DZNE
Deutsches Zentrum für
Neurodegenerative Erkrankungen
in der Helmholtz-Gemeinschaft

UNIVERSITÄT BONN

Advanced Image Reconstruction Methods for Ultra-High Field MRI

DISSERTATION

zur
Erlangung des Doktorgrades (Dr. rer. nat.)
der
Mathematisch-Naturwissenschaftlichen Fakultät
der
Rheinischen Friedrich-Wilhelms-Universität Bonn

vorgelegt von

Jolanda M. Schwarz

aus Kenzingen

Bonn, April 2020

Angefertigt mit Genehmigung der Mathematisch-Naturwissenschaftlichen Fakultät der
Rheinischen Friedrich-Wilhelms-Universität Bonn

1. Gutachter: Prof. Dr. Tony Stöcker
2. Gutachter: Prof. Dr. Carsten Urbach

Tag der mündlichen Prüfung: 24. Juni 2020
Erscheinungsjahr: 2020

Abstract

Magnetic resonance imaging (MRI) has become a very powerful and flexible medical imaging technique, that allows an unrivaled insight into human anatomy and physiology. For a wide range of possible applications, acquisition of high-quality images in short scan times is essential. A recent step in this direction is the introduction of the first clinical 7 Tesla MRI scanners. For instance, the high signal-to-noise ratio (SNR) achieved by the strong magnetic field allows for increased parallel imaging accelerations. However, the images are more susceptible to magnetic field deviations, such as those caused by subject motion or instrumental imperfections. This thesis addresses these challenges and contributes to the acquisition and reconstruction of ultra-fast high-quality 3D images at 7 Tesla MRI scanners.

The first part focuses on the development and validation of a novel non-iterative parallel imaging reconstruction for wave-CAIPI acquisitions. The recently proposed wave-CAIPI sampling strategy along corkscrew sampling trajectories in the spatial frequency space allows to utilize the coil sensitivity variations of multiple receiver coils in all three dimensions, instead of two with conventional parallel imaging. Although Cartesian parallel imaging reconstructions are no longer applicable, the reconstruction can be formulated as a Cartesian problem which allows to use a GRAPPA-based reconstruction of the missing data in the frequency space. The developed GRAPPA-based wave-CAIPI reconstruction is fast and robust and, compared to the previously proposed iterative SENSE-type reconstruction, it does not depend on the accuracy of specific coil sensitivity estimations and mask regions. A system of nuclear magnetic resonance (NMR) field probes is used to determine the actual corkscrew trajectories required for a successful and artifact-free wave-CAIPI reconstruction. The utility of GRAPPA-based wave-CAIPI is investigated at a 7 Tesla scanner on the example of two widely-used fast 3D structural MRI methods: T_1 weighted gradient echo (MP-RAGE) and T_2

weighted spin echo (TSE). The additional spatial information gained with wave-CAIPI sampling allows to significantly increase image quality and SNR of rapidly acquired images. 16-fold accelerated whole brain wave-CAIPI MP-RAGE and wave-CAIPI TSE data with $1\,\mathrm{mm}$ isotropic resolution and good image quality are acquired in only 40 seconds and 1:32 minutes, respectively.

The second contribution of this thesis addresses the monitoring and correction of magnetic field fluctuations induced by the patient's physiology. Field perturbations caused by deep breathing or limb motion effect the signal encoding and lead to artifacts in the reconstructed brain images. Nevertheless, many of the image artifacts caused by magnetic field distortions can be corrected if the magnetic field changes are known. Therefore, a field correction approach that accounts for field changes of up to first order spatial expansion is incorporated into the GRAPPA-based parallel imaging reconstruction. Considering technical limitations of the NMR field probes, such as the minimal time between successive field probe excitations, two field monitoring approaches with different temporal resolution are investigated and compared for high-resolution T_2^* weighted 3D-EPI acquisitions at 7 Tesla. Especially for acquisitions that are subject to strong field changes, the temporal SNR strongly benefits from field correction and high-quality images can be regained.

Zusammenfassung

Die Magnetresonanztomographie (MRT) hat sich zu einer sehr leistungsfähigen und flexiblen medizinischen Bildgebungstechnik entwickelt, die einen unvergleichlichen Einblick in die menschliche Anatomie und Physiologie ermöglicht. Für ein breites Spektrum möglicher Anwendungen ist die Aufnahme qualitativ hochwertiger Bilder in kurzen Messzeiten unerlässlich. Ein aktueller Schritt in diese Richtung ist die Einführung der ersten klinischen 7-Tesla-MRT-Scanner. So ermöglicht beispielsweise das hohe Signal-Rausch-Verhältnis (SNR), das durch das starke Magnetfeld erreicht wird, eine erhöhte parallele Bildbeschleunigung. Die Bilder sind jedoch anfälliger für Magnetfeldabweichungen, wie sie beispielsweise durch die Bewegung der Patienten oder durch instrumentelle Imperfektionen verursacht werden. Die vorliegende Arbeit befasst sich mit diesen Herausforderungen und trägt zur Erfassung und Rekonstruktion ultraschneller 3D-Bilder hoher Qualität bei 7 Tesla bei.

Der erste Teil konzentriert sich auf die Entwicklung und Validierung einer neuartigen, nicht-iterativen parallelen Bildrekonstruktion für wave-CAIPI Messungen. Die kürzlich veröffentlichte wave-CAIPI Samplingstrategie ermöglicht es, die Sensitivitätsvariationen der Empfangsspulen nicht wie in der herkömmlichen parallelen Bildgebung in nur zwei, sondern in allen drei Dimensionen zu nutzen. Obwohl die wave-CAIPI Technik keine kartesische Messmethode ist, kann die parallele Bildrekonstruktion als ein kartesisches Problem formuliert werden, sodass eine GRAPPA-basierte Rekonstruktion der fehlenden Daten im Frequenzraum verwendet werden kann. Im Vergleich zu der zuvor implementierten interativen SENSE-Rekonstruktion, ist die hier entwickelte GRAPPA-basierte wave-CAIPI Rekonstruktion nicht nur robust, sondern auch unabhängig von den expliziten Spulensensitivitäten sowie der Maskierung dieser Regionen. Mithilfe eines externen Magnetfeldsondensystems werden die für eine erfolgreiche und artefaktfreie wave-CAIPI Rekonstruktion

erforderlichen tatsächlichen Korkenzieher-Trajektorien bestimmt. Die Wirksamkeit der GRAPPA-basierten wave-CAIPI Rekonstruktion wird an einem 7-Tesla-Scanner anhand von zwei weit verbreiteten schnellen strukturellen 3D-MRT-Methoden validiert: T_1 gewichtetes Gradienten-Echo (MP-RAGE) und T_2 gewichtetes Spin-Echo (TSE). Die zusätzliche räumliche Information, die mit dem wave-CAIPI Sampling gewonnen wird, erlaubt es, die Bildqualität und das SNR von schnell aufgenommenen Bildern signifikant zu erhöhen. 16-fach beschleunigte wave-CAIPI MP-RAGE und wave-CAIPI TSE Daten mit einer isotropen Auflösung von $1\,\mathrm{mm}$ und guter Bildqualität werden in nur 40 Sekunden bzw. 1:32 Minuten aufgenommen.

Der zweite Beitrag dieser Arbeit befasst sich mit der Überwachung und Korrektur von Magnetfeldfluktuationen, die durch die Physiologie des Patienten induziert werden. Feldstörungen, die durch tiefe Atmung oder Bewegung von Gliedmaßen verursacht werden, beeinflussen die Signalkodierung und führen zu Artefakten in den rekonstruierten Hirnaufnahmen. Wenn die Magnetfeldänderungen bekannt sind, können jedoch viele der durch Magnetfeldverzerrungen verursachten Bildartefakte korrigiert werden. In die GRAPPA-basierte parallele Bildrekonstruktion wird hierzu eine Korrektur für Felder bis zu einer räumlichen Ausdehnung erster Ordnung integriert. Unter Berücksichtigung der technischen Möglichkeiten der Magnetfeldsonden, wie beispielsweise des zeitichen Mindestabstands zwischen aufeinanderfolgenden Sondenanregungen, werden zwei Feldüberwachungsansätze mit unterschiedlicher zeitlicher Auflösung für hochaufgelöste T_2^*-gewichtete 3D-EPI-Aufnahmen bei 7 Tesla untersucht und verglichen. Insbesondere Aufnahmen, die starken Feldänderungen unterliegen, profitieren von der Feldkorrektur, sodass ein verbessertes zeitlichen SNR und eine hochwertige Bildqualität gewonnen werden können.

Contents

1

Introduction

1.1 Motivation

Magnetic resonance imaging (MRI) is a flexible and powerful medical imaging technique. Unlike invasive imaging modalities such as radiography, computed tomography (CT) or positron emission tomography (PET), it does not employ ionizing radiation or radioactive substances. Furthermore, MRI enables excellent soft tissue imaging and benefits from a variety of different contrasts. The origins of MRI date back to the first successful nuclear magnetic resonance (NMR) experiments by Felix Bloch and Edward Purcell (Bloch, 1946; Purcell and Torrey, 1946) in 1945. However, it was not until the 1970s, that Paul Lauterbur (Lauterbur, 1973) obtained the first images by using gradient fields for spatial mapping of NMR resonances. With the development of a fast reliable mathematical reconstruction by Peter Mansfield (Mansfield and Maudsley, 1976) and the improvement in scanner hardware and computers, MRI was introduced in the clinical routine in the early 1980s, where it has become an essential imaging modality suitable for a wide range of applications and allowing unrivaled insight into human anatomy and physiology.

Compared to other imaging modalities, the main drawback of MRI lies in relatively long acquisition times, which hamper their use for some applications in research and especially in clinical routine. Together with high purchasing and maintenance costs of MR scanners the long scan times lead to high costs per patient. In addition, the narrow scanner bore and the loud noise caused by the vibration of the rapidly switching gradients can make patients feel uncomfortable or claustrophobic during long measurements. These patients get restless and often start moving, which can lead to artifacts in the images and making them difficult to interpret.

Because of the described negative consequences of long measurements, the reduction of the acquisition time is still one of the most important goals in MRI related research. Since the early clinical advent of MRI, where low resolution volumetric MRI acquisition still took about one hour, improvements through rapid imaging techniques (Haase et al., 1986; Hennig et al., 1986; Mansfield, 1977) and advanced scanner hardware have significantly reduced the acquisition time. A major breakthrough in further increasing imaging speed was the development of multi-coil arrays. The use of multiple receiver coils, placed around the object to be imaged, allow the MR signal to be acquired simultaneously at different locations. Moreover, the additional information gained by the distinct spatial coil sensitivities is used in parallel imaging to reduce the amount of gradient encoding steps and thereby to speed up the data acquisition without changing the image contrast. Reasonable acceleration factors are limited by the decrease of the signal-to-noise ratio (SNR), which make strong parallel imaging acceleration very interesting at 7 Tesla scanners which typically provide higher SNR than the clinical 1.5 or 3 Tesla scanners. Depending on the application and the coil array set-up, parallel imaging commonly allows reductions in acquisition times by up to a factor of eight.

MRI data are acquired in spatial frequency space which is successively sampled with each gradient encoding step. The sampling extend defines the image resolution; the spacing of sampling points defines the image field of view. Each sampling point thus contributes to the entire image which is gained by the inverse Fourier transform. Since parallel imaging acceleration reduces the amount of encoding steps, i.e. the sampling density, acquisitions with this technique result in aliasing (fold-over) artifacts in the images. To combine the subsampled data from each of the receiver coils into one artifact-free image, specific parallel imaging reconstruction algorithms are required, among which SENSE (Pruessmann et al., 1999) and GRAPPA (Griswold et al., 2002) are the most commonly employed ones. Although these techniques apply different algorithmic approaches to recover the missing information, they both require an accurate calibration of the coil sensitivities to solve an ill-posed problem.

In addition to the reconstruction algorithms, the sampling strategy strongly determines the quality of the reconstructed image. In this context 2D CAIPIRINHA (Breuer et al., 2006) is a well-established sampling strategy which modifies the appearance of the 2D aliasing artifacts and thus tries to maximize utilization of the spatial coil sensitivity variations. The idea behind 2D CAIPIRINHA can be taken a step further by spreading the aliasing not only in two but also a third dimension in which case the method is known as wave-CAIPI (Bilgic et al., 2015). The special feature of wave-CAIPI is the use of corkscrew sampling trajectories in the frequency space instead of rectilinear aligned sample points (Cartesian sampling) employed by most parallel imaging acquisitions. However, this also implies that Cartesian implementations of SENSE or GRAPPA reconstructions are no longer applicable. The accurate and efficient image reconstruction of non-Cartesian acquisitions is a challenging problem which requires exact knowledge of the sampling trajectories. The first part of this thesis aims to implement a robust and non-iterative GRAPPA-based wave-CAIPI reconstruction as an alternative to the previously proposed iterative SENSE-type reconstruction (Bilgic et al., 2015).

Due to hardware limitations, the actual trajectory usually deviates from the nominal trajectory which can lead to severe artifacts in the images. In this work, a system of NMR field probes (De Zanche et al., 2008) was used to determine the actual corkscrew trajectories required for a successful reconstruction of non-Cartesian data. The utility of GRAPPA-based wave-CAIPI was investigated on the example of the two most relevant 3D structural MRI methods.

Patient movement can lead to deviations from the nominal trajectory as well. Although parallel imaging techniques and fast imaging sequences allow scanning times to be significantly reduced, motion thus still leads to image artifacts. In addition to direct misregistration artifacts, moving tissues lead to spatio-temporal field fluctuations induced by changes in magnetic susceptibility in the magnetic bore. These field fluctuations even extend to locations further apart from the moving limb. For example, the movement of the chest during respiration and the varying lung volume disturb the spatial field distribution in the head region and thus influences the spatial encoding in the brain. Since physiological field changes scale with the signal amplitude, their effects are more prominent at higher field strengths, such as 7 Tesla. Nevertheless, many of the image artifacts caused by magnetic field distortions can be corrected if the magnetic field and the field gradients are known. NMR field probes allow to detect these fields during the scan. However, the monitoring is limited by various factors such as the decay of the field probe signal, the time between successive probe excitations and the probe positioning. The objective of the second part of this thesis is to measure and investigate physiological field fluctuations in fast 3D MRI acquisitions despite these limitations, and to implement a field correction which accounts for global magnetic field changes and small shifts away from the nominal sampling trajectory caused by field perturbations.

1.2 Thesis Outline

The content of this thesis is organized in four main parts consisting of an overview of the theoretical background (Chapter 2) followed by this thesis' contributions to ultra-fast 3D imaging using a GRAPPA-based reconstruction (Chapter 3) and to the correction of physiological fluctuations in 3D acquisitions (Chapter 4). A conclusion with outlook is given in Chapter 5.

The main principles of MR imaging and the technique of spatial encoding of the MR signal using magnetic field gradients are briefly introduced in Chapter 2. Furthermore, the concept of k-space and different sampling trajectories are discussed. A second part of the chapter covers the basics of parallel imaging acceleration and explains the most commonly used parallel imaging reconstruction algorithms SENSE and GRAPPA, as well as GROG, an extension of GRAPPA that allows a shifting of parallel imaging data in the k-space. In a third part, the origins of magnetic field distortions and their effect on signal encoding are described. Finally, the design and functionality of the NMR field probes used in this work for magnetic field monitoring are explained.

Chapter 3 gives an overview of the wave-CAIPI concept and introduces the GRAPPA-based reconstruction method developed within the scope of this thesis. The reconstruction method is validated for highly accelerated whole-brain wave-CAIPI acquisition performed at 7 Tesla. For this purpose, wave-CAIPI sampling was incorporated in two MR sequences, MP-RAGE and TSE, which provide distinct soft tissue contrast and enable different gradient waveforms. Trajectory measurements are performed using an NMR field probe system. Furthermore, the advantages and limitations of wave-CAIPI acquisitions and the GRAPPA-based wave-CAIPI reconstruction are discussed.

In Chapter 4, the field probes are used for in-vivo monitoring of subject-induced field changes in high-resolution 3D acquisitions at 7 Tesla. The effect of field fluctuations induced by the movement of the thorax during breathing or repeated hand movements is investigated. Two different field probe-based monitoring approaches, namely snapshot and concurrent field monitoring, are compared and their benefits and limitations are discussed. The correction of physiological field fluctuations up to the first-order are included in the image reconstruction for both approaches. Furthermore, methods to consider the eddy current compensation performed by the scanner during signal reception are proposed.

Finally, Chapter 5 concludes the findings presented in this thesis and gives a brief outlook on possible research topics that can be pursued based on this work.

1.3 Publications

The following works have been published within the scope of this thesis:

Journal papers

- **Schwarz JM**, Pracht ED, Brenner D, Reuter M and Stöcker T, 2018. GRAPPA reconstructed wave-CAIPI MP-RAGE at 7 Tesla. Magnetic Resonance in Medicine 80, 2427-2438.

Conference Contributions

- **Schwarz JM**, Brenner D, Layton KJ, Zaitsev M and Stöcker T, 2016. 16-fold accelerated 3D imaging at 7 Tesla using the hardware-independent sequence format PulSeq and a python toolbox for image reconstruction. Proceedings of the 33 Scientific Meeting of the European Society for Magnetic Resonance in Medicine and Biology, p. 112.
- **Schwarz JM**, Brenner D, Pracht ED and Stöcker T, 2017. GRAPPA reconstructed wave-CAIPI MPRAGE at 7 Tesla. Proceedings of the 25th Scientific Meeting of the International Society for Magnetic Resonance in Medicine, p. 5174.

- **Schwarz JM**, Pracht ED and Stöcker T, 2018. GRAPPA reconstructed 3D wave-CAIPI TSE at 7 Tesla. Proceedings of the 26th Scientific Meeting of the International Society for Magnetic Resonance in Medicine, p. 0938. (ISMRM Summa Cum Laude Merit Award)
- **Schwarz JM**, Stirnberg R, Ehses P and Stöcker T, 2019. Correction of physiological field fluctuations in high- and low-resolution 3D-EPI acquisitions at 7 Tesla. Proceedings of the 27th Scientific Meeting of the International Society for Magnetic Resonance in Medicine, p. 0446. (ISMRM Magna Cum Laude Merit Award)
- Brunheim S, Mirkes C, Dietrich B, **Schwarz JM**, Stirnberg R, Ismar S, Alexander C, Barmet C and Stöcker T, 2020. Replaceable field probe holder for the Nova coil on a 7 Tesla Siemens scanner. Proceedings of the 28th Scientific Meeting of the International Society for Magnetic Resonance in Medicine.

Application notes

- **Schwarz JM**. User application: Clip-On Camera, GRAPPA reconstructed wave-CAIPI MP-RAGE - Delay correction versus full trajectory measurement. *https://www.skope.swiss/user-application-wave-caipi*

2

Background

2.1 Basics of Magnetic Resonance Imaging

2.1.1 Nuclear Magnetic Resonance

Nuclear magnetic resonance (NMR) is the fundamental physical phenomenon behind MRI. It was first experimentally described by Felix Bloch and Edward Purcell in 1946 (Bloch, 1946; Purcell and Torrey, 1946). For their discovery, they both shared the Nobel Prize for Physics in 1952.

Nuclei with unpaired protons or neutrons possess a non-zero spin angular momentum S that causes a rotation of the nucleus around its own axis. Such nuclei behave as small magnetic dipoles with random orientation and magnetic moment

$$\mu = \gamma \mathbf{S}. \tag{2.1}$$

The physical constant γ, known as gyromagnetic ratio, is specific for different nuclei. The most import nucleus for MRI applications is the nucleus of hydrogen ^{1}H which consists of a single proton with spin 1/2 and gyromagnetic ratio $\gamma = 2.675 \cdot 10^8\,\mathrm{rad/s/T}$ or $\frac{\gamma}{2\pi} = 42.58\,\mathrm{MHz/T}$.

Nuclear spins interact with an external magnetic field B_0, which is by convention and without loss of generality assumed oriented along the z-direction. Spin-1/2 systems such as ^{1}H, ^{13}C, ^{19}F, ^{31}P tend to align their spins parallel (spin-up) or anti-parallel (spin-down) to B_0. They thereby create two distinct energy levels, where the spin-down state is the higher energy state. The energy difference between the two energy states is given by

$$\Delta E = \gamma \hbar B_0, \tag{2.2}$$

where $\hbar$ is the Planck's constant divided by 2π. This phenomenon of energy splitting in an external magnetic field is called Zeeman Effect. In the thermal equilibrium, the distribution of the spins in the two energy levels is determined by the Boltzmann distribution

$$\frac{n_\downarrow}{n_\uparrow} = \exp\left(-\frac{\Delta E}{k_B T}\right) \tag{2.3}$$

with the population of the two spin states $n_\downarrow$ and $n_\uparrow$, the absolute temperature T of the system and the Boltzmann constant $k_B = 1.381 \cdot 10^{-23}\,\mathrm{J/K}$. At room temperature and in a high magnetic field of $B_0 = 7\,\mathrm{T}$, there are approximately 0.005% more spins in the lower than in the upper energy state. Although the population difference is small, an observable macroscopic magnetization

$$\mathbf{M} = \sum_{n=1}^{N_s} \mu_{\mathbf{n}} \tag{2.4}$$

of the spin system is generated. Here, N_s is the total number of spins and $\mu_{\mathbf{n}}$ is the magnetic moment of the n-th spin.

According to the Planck–Einstein relation, a transition of spins between the two energy states can be induced by applying a radiofrequency (RF) pulse of the angular frequency

$$\omega_0 = \frac{\Delta E}{\hbar} = \gamma B_0. \tag{2.5}$$

The characteristic resonance frequency is known as Larmor frequency . For ^{1}H atoms in a $7\,\mathrm{T}$ magnetic field the frequency is $f_0 = \frac{\omega_0}{2\pi} \approx 298\,\mathrm{MHz}$.

2.1.2 Bloch Equations and Relaxation

Although only quantum mechanics allow a complete description of the NMR phenomenon, some of its features can be explained in a classical way.

In the equilibrium, the net magnetization $\mathbf{M}$ is parallel with the main magnetic field $\mathbf{B_0}$. By applying an additional alternating magnetic field $\mathbf{B_1}$ (RF pulse at Larmor frequency ω_0) perpendicular to $\mathbf{B_0}$, the system gets excited and the macroscopic magnetization is tipped from the longitudinal into the transversal direction by an excitation angle α. After the excitation, the spin system relaxes back to the equilibrium state. This relaxation is characterized by a precession of $\mathbf{M}$ around $\mathbf{B_0}$.

The behavior of $\mathbf{M}$ under influence of a total magnetic field $\mathbf{B}$ is described by a set of differential equations known as Bloch equations (Bloch, 1946):

$$\frac{\mathrm{d}\mathbf{M}}{\mathrm{d}t} = \gamma\left(\mathbf{M} \times \mathbf{B}\right) + \frac{M_x \mathbf{e_x} + M_y \mathbf{e_y}}{T_2} - \frac{(M_z - M_0)\mathbf{e_z}}{T_1}. \tag{2.6}$$

Here, M_0 denotes the equilibrium magnetization, $\mathbf{e_x}$, $\mathbf{e_y}$ and $\mathbf{e_z}$ are unit vectors in x, y and z-direction and the time constants T_1 and T_2 characterize two independent relaxation processes, the longitudinal and the transversal relaxation, of the spin system after excitation.

The relaxation of the longitudinal magnetization M_z, also known as the spin-lattice relaxation, is induced by energy exchange of the spins with their surrounding (lattice). The exponential behavior is described by

$$M_z(t) = M_0 + (M_z(0) - M_0)e^{-t/T_1}. \tag{2.7}$$

The longitudinal relaxation time T_1 is defined as the time required for the longitudinal magnetization to reach approximately 67% $(1 - 1/e)$ of its original equilibrium value.

The relaxation of the transversal component $M_{x,y}$ of the magnetization, the so-called spin-spin relaxation, originates from local fluctuations of the dipole fields of interacting spins which lead to a loss of phase coherence of the spins. The decay of the magnetization is given by

$$M_{x,y}(t) = M_{x,y}(t = 0)e^{-t/T_2}e^{-i\omega_0 t}, \tag{2.8}$$

where the transversal relaxation time T_2 describes the time when the transverse magnetization irreversibly decayed to approximately 37% $(1/e)$ of its initial value directly after the excitation. The relaxation times T_1 and T_2 vary between different tissues and are frequently used sources of MR image contrast (cf. Section 2.1.5).

Additional to spin-spin interactions, a dephasing of the spins can be induced by inhomogeneous magnetic fields. As this inhomogeneity is static and time-independent, its influence can be reversed by proper design of MR sequences. The effective transverse relaxation in the presence of magnetic field inhomogeneities $DeltaB_0$ is characterized by the time constant T_2^*. The decay can be approximated by

$$\frac{1}{T_2^*} = \frac{1}{T_2} + \gamma\Delta B_0. \tag{2.9}$$

2.1.3 Spatial Encoding

Up to now, the NMR signal arises from the whole measured volume and informations cannot be spatially localized. In order to produce a 3D volumetric image, a spatial dependency needs to be encoded in the FID signal. According to Equation 2.5, the Larmor frequency is proportional to the magnetic field strength. By applying spatially varying magnetic field gradients $G(\mathbf{r})$, the precession frequency of the spins is directly related to their positions along that direction. For linear gradients, the resonance frequency at the position $\mathbf{r}$ is given by

$$\omega(\mathbf{r}) = \gamma(B_0 + \mathbf{G}(\mathbf{r})\mathbf{r}) = \omega_0 + \gamma\mathbf{G}(\mathbf{r})\mathbf{r}. \tag{2.10}$$

Such field alterations along the scanners' orthogonal directions x, y and z are usually generated using a set of three gradient coils. Linear combinations of the three gradients allow the encoding and imaging of arbitrary planes. In the following, the most relevant spacial encoding methods are briefly explained.

2.1.3.1 Slice Selection

A common method to excite a thin slice of the imaged object is the slice-selective excitation. By employing simultaneously a linear magnetic gradient along the axis perpendicular to the desired slice (e.g. the xy-plane) and a frequency selective RF pulse, only nuclei with resonant frequencies inside the narrow frequency bandwidth Δf of the excitation pulse are affected by the pulse. Consequently, the excitation only takes place in a slice of thickness

$$\Delta z = \frac{2\pi\Delta f}{\gamma G_z} \tag{2.11}$$

which depends on the bandwith of the RF pulse and on the amplitude of the slice selection gradient (here along the z-direction).

2.1.3.2 Frequency Encoding

Frequency encoding of the spatial position again uses the fact, that the resonance frequency depends on the magnetic field strength. Applying a gradient during data acquisition spatially modifies the precession frequency of the spins. The position of a spin is now encoded in the frequency of the measured signal. Since the gradient is turned on during the signal readout, this direction is also called readout direction and the gradient is often referred as readout gradient.

2.1.3.3 Phase Encoding

The aforementioned frequency encoding allows to separate signal contributions of a thin slice along one spatial dimension. To obtain an image of the selected slice, further spatial informations are required. This is achieved by applying a gradient field for a short time interval after the excitation and before the signal acquisition. Due to the gradient field, the spins precess with slightly different frequencies, which leads to a dephasing depending on their position along the gradient direction. When the phase encoding gradient is switched off, the spins again precess all with the same frequency, but possess a different phase which is linearly dependent on the spatial coordinate. Since the phase of individual spins cannot be disentangled from the net MR signal, the process needs to be repeated with linearly varying gradient strength in order to encode a spatial frequency. An alternative to slice-selective two-dimensional MR experiments is three-dimensional spatial encoding. Here, not only a thin slice, but a complete volume is excited and additional phase encoding is employed along the third dimension.

2.1.3.4 Signal Equation and k-Space Formalism

Following an RF excitation, the transversal magnetization of a spin system precesses around the axis of the magnetic field described by Equation 2.8. According to Faraday's Law, the time varying electromagnetic field can be measured by a receiver coil non-parallel to the transverse plane. The measured signal is called free induction decay (FID).

The MR signal of the entire sample volume is determined by the integral over the transversal magnetization in the volume. The signal equation is given by

$$S(t) \propto \int\limits_{volume} M_{x,y}(x,y,z,t)\mathrm{d}V = \left[\int\limits_x \int\limits_y \int\limits_z M_{x,y}(x,y,z,t=0)e^{-t/T_2(x,y,z)}\mathrm{d}x\mathrm{d}y\mathrm{d}z\right] e^{-i\omega_0 t}. \tag{2.12}$$

The term $e^{-i\omega_0 t}$ corresponds to the carrier signal induced by the static magnetic field. In the following, the signal equation is simplified by moving to the rotating frame which corresponds to a demodulation of the acquired signal by the Larmor frequency.

Ignoring relaxation effects, the signal of a 2D slice-selective MR experiment using frequency and phase encoding gradients G_x and G_y for spatial encoding can be written as

$$S(t) = \int\limits_x \int\limits_y M_{x,y}(x,y,t=0)e^{-i\gamma\left[\int_0^t G_x(\tau)\mathrm{d}\tau\right]x} e^{-i\gamma\left[\int_0^t G_y(\tau)\mathrm{d}\tau\right]y}\mathrm{d}x\mathrm{d}y. \tag{2.13}$$

By introducing the spatial frequency variables

$$k_x = \frac{\gamma}{2\pi}\int\limits_0^t G_x(\tau)\mathrm{d}\tau, \qquad k_y = \frac{\gamma}{2\pi}\int\limits_0^t G_y(\tau)\mathrm{d}\tau, \tag{2.14}$$

Equation 2.13 can be rewritten as

$$S(k_x,k_y) = \int\limits_x \int\limits_y M_{x,y}(x,y,t=0)e^{-i2\pi k_x x}e^{-i2\pi k_y y}\mathrm{d}x\mathrm{d}y. \tag{2.15}$$

In the more general vector form, the signal equation in the rotating frame leads to

$$S(\mathbf{k}) = \int\limits_{volume} M_{x,y}(\mathbf{r}, t=0) e^{-i2\pi\mathbf{kr}} \mathrm{d}^3 r \propto \mathcal{FT}\left[M_{x,y}(\mathbf{r}, t=0)\right], \tag{2.16}$$

where $\mathbf{k}$ is the k-space vector and $\mathbf{r}$ is the position vector in image space. The equation directly shows, that the signal $S(\mathbf{k})$ corresponds to the Fourier transform of the transverse magnetization. An MR image (spatial distribution of spin density) can thus be gained by the inverse Fourier transform of the received signal.

The k-space formalism is a useful interpretation of the signal acquisition. Applying gradients is equivalent to traveling through k-space along trajectories and the k-space is typically subsequently filled during an MR imaging protocol. Since it is not possible to continuously acquire the MR signal, only discrete points are sampled in k-space. The distance Δk between acquired k-space points determines the field of view (FOV) that can be imaged without leading to fold-in/aliasing artifacts. According to the Nyquist criterion, the size of the imaged object is given by

$$FOV_i = \frac{1}{\Delta k_i}; i \in \{x, y, z\} \tag{2.17}$$

Different FOV sizes in the different directions can be obtained by choosing different values for Δk.

The maximum achievable spatial resolution

$$\Delta i = \frac{FOV_i}{N_i} = \frac{1}{2k_i^{max}}; i \in \{x, y, z\} \tag{2.18}$$

is determined by the maximum acquired k-space value k^{max}. This corresponds to the highest sampled spatial frequency. Here, N denotes the number of pixels or k-space samples.

2.1.4 MRI Pulse Sequences

Pulse sequences combine RF pulses and spatial encoding techniques (using gradients) to acquire all k-space data required to obtain an MR image.

2.1.4.1 Fundamental MRI Pulse Sequences

MRI pulse sequences can generally be divided into spin echo and gradient echo sequences. Since both sequences are used in this work, the basics for the two sequences are briefly described.

Gradient Echo Imaging Sequences

Figure 2.1 shows the timing diagram of a simple 2D gradient echo pulse sequence with slice-selective excitation. For spatial encoding, three gradients, frequency encoding or readout gradient G_r, slice selection gradient G_s and phase encoding gradient G_p are required. During the slice selection, the magnetization of the selected slice is tipped into the transverse plane. The slice selection is followed by a refocusing gradient to reverse the dephasing of the spins and to null the accumulated gradient moment. To measure one k-space line, the FID signal is spatially encoded in the phase encoding direction. At the same time, a readout prephasing gradient prepares the signal for the readout. The subsequent readout gradient (with twice the duration of the readout prephasing gradient) refocuses the magnetization and generates a gradient echo in the middle of the data acquisition window. The time of the echo after the excitation is referred as echo time TE. To reduce image artifacts due to remaining phase encoding signal, the phase encoding gradient is rewound after the readout and before the next excitation. This basic block of the pulse sequence is repeated for all different phase encoding steps to completely fill the k-space. The time between successive excitations is denoted as repetition time TR. Usually, spoiler gradients (not shown in Figure 2.1) are applied after signal acquisition in order to dephase the remaining magnetization and to reduce echoes from preceding repetitions.

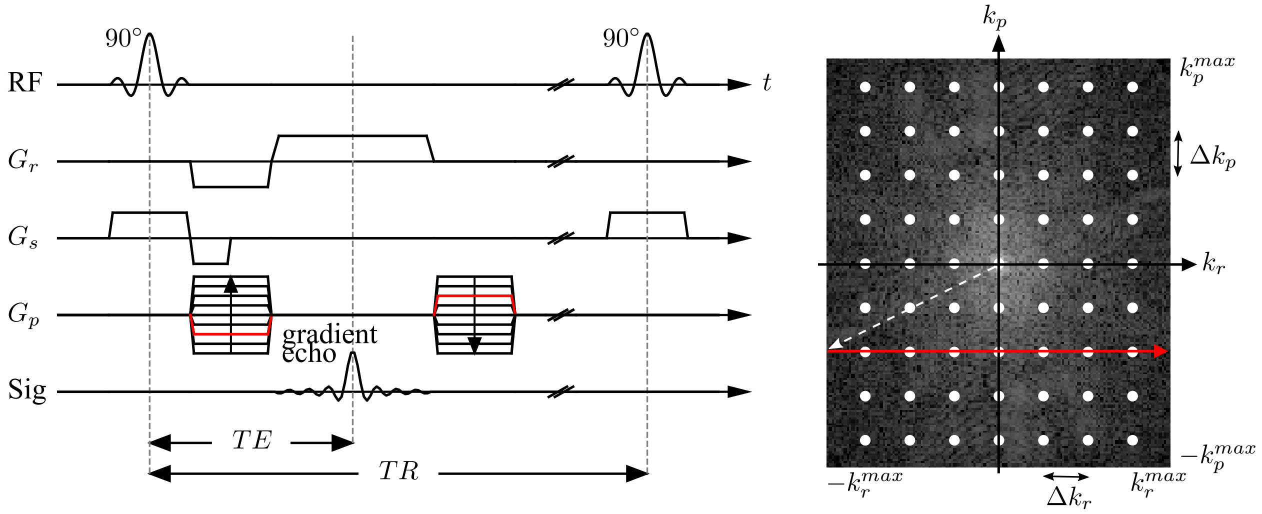

Figure 2.1: Schematic timing diagram of a 2D gradient echo sequence. The different lines show the RF pulses, the readout, slice and phase encoding gradient axes and the generated gradient echo signal. The phase encoding step marked in red in the sequence diagram results in the red k-space path in the schematic k-space shown on the right.

Spin Echo Imaging Sequences

Figure 2.2 depicts the sequence diagram of a typical 2D spin echo sequence. The main difference to the gradient echo sequence is the refocusing of the magnetization with an RF refocusing pulse instead of only gradients. A $180°$ pulse at time $TE/2$ inverts the dephasing magnetization which rephases and generates an echo at the time TE after the excitation. Due to the echo generation using refocusing pulses, the minimal acquisition time for a whole slice or volume is longer than for gradient echo sequences.

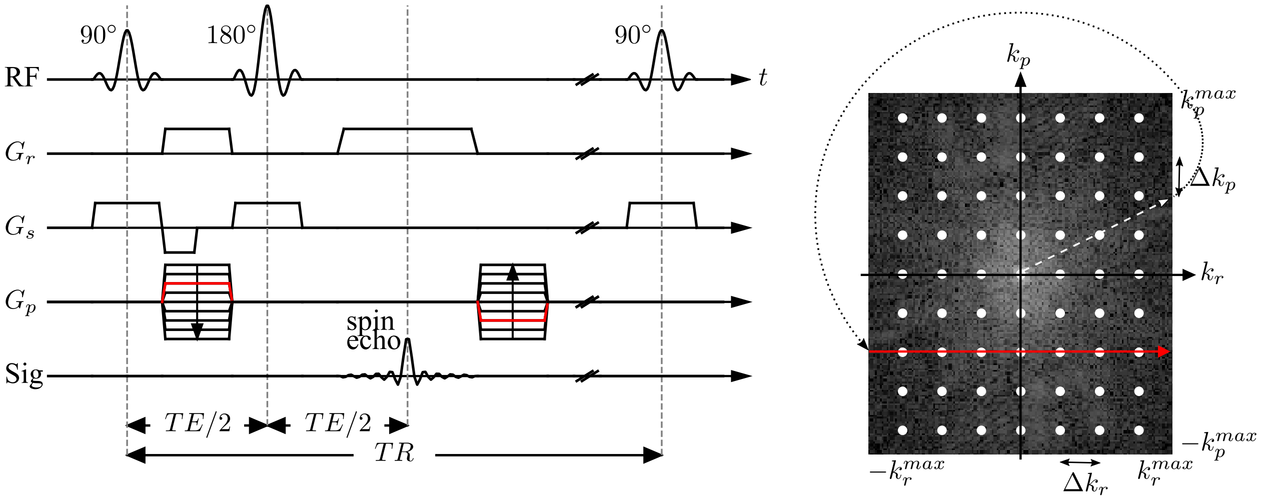

Figure 2.2: Schematic timing diagram of a 2D spin echo sequence using a $180°$ pulse to refocus the magnetization (left). The phase encoding step marked in red in the sequence diagram results in the red k-space path (right). The refocusing pulse rotates the start of each k-space line by $180°$ as indicated by the black dashed line.

Developing complex MRI sequences with multiple gradients and RF pulses requires the calculation of the signal course during the acquisition. This can be done using the Bloch equations. However, solving the Bloch equations for thousands of microscopic groups of spins is computational expensive. A powerful tool to depict and understand the magnetization response and echo generation of MRI sequences is the extended phase graph (EPG) concept. An overview of the principles of the EPG concept can be found in (Weigel, 2015).

2.1.4.2 Volumetric Imaging

The gradient echo and spin echo sequence shown above are 2D sequences with slice-selective RF pulses, where N_p phase encoding steps are acquired to fill the 2D k-space. The total acquisition time for the slice is given by $N_p \cdot TR$ and in case of Cartesian k-space sampling, the final image is obtained by applying the two-dimensional inverse Fourier transform. To obtain volumetric image data, multiple slices are acquired and stacked into a 3D volume after the reconstruction of each slice. In contrast, 3D volumetric encoding excites the whole volume using non-selective RF pulses. The slice selection is replaced by additional phase encoding and the sequence thus consists of one frequency encoding direction and two phase encoding direction with N_{p1} and N_{p2} phase encoding steps. The time required to fill the 3D k-space is equal to $N_{p1} \cdot N_{p2} \cdot TR$. For Cartesian acquisitions, the spatial distribution of the transverse magnetization is yielded directly by the three-dimensional inverse Fourier transform.

2.1.4.3 k-Space Sampling Strategies

There are various different ways to cover k-space. Four different k-space trajectories with the respective gradient waveforms are schematically depicted in Figure 2.3.

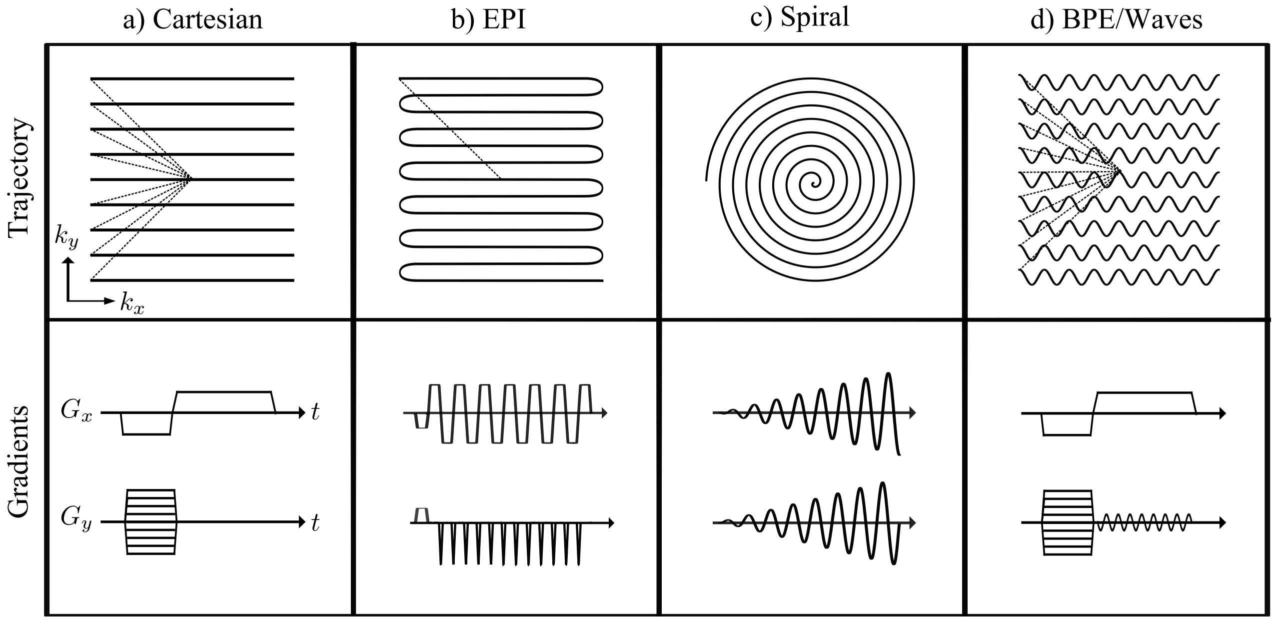

Figure 2.3: Different k-space trajectories including the respective gradient waveforms: a) Cartesian line-by-line sampling, b) echo planar imaging (EPI) as a specific example for fast Cartesian imaging, c) spiral sampling and d) bunched phase encoding (BPE) or wave-encoding for 3D imaging with sinusoidal gradients in both phase encoding directions.

Most MRI applications employ Cartesian trajectories (cf. Figure 2.3a)), where the k-space is acquired on a regular grid. The k-space is often sampled line-by-line such as in the example sequences in Section 2.1.4.1. This sampling scheme is robust, but rather slow due to the long recovery time of the magnetization after each excitation.

An example for fast and efficient Cartesian k-space traversal is echo planar imaging (EPI) (Mansfield, 1977). After spin excitation, multiple k-space lines are acquired using short blipped phase encoding gradients after each readout(cf. Figure 2.3b)). Due to the alternating readout gradients, successive readout lines of an EPI echo train have different k-space sampling directions (‘even’ and ‘odd’ lines). For a successful image reconstruction, every second k-space line must be reflected before the reconstruction.

However, k-space can also be sampled along non-Cartesian trajectories. By using varying gradient waveforms instead of linear gradients, data are acquired off the Cartesian grid. Depending on the trajectories and on the applications, non-Cartesian imaging can have some benefits compared to Cartesian imaging. These are among others a fast k-space coverage due to an efficient use of gradient hardware or reduced sensitivity to subject motion. An example of a commonly used non-Cartesian k-space traversal is the spiral trajectory (Ahn et al., 1986) as schematically shown in Figure 2.3c).

Another non-Cartesian trajectory used for some fast imaging applications is bunched phase encoding (BPE) (Moriguchi and Duerk, 2006). It applies a sinusoidal phase encoding gradient during the readout of each k-space line and thereby creates oscillating k-space trajectories (cf. Figure 2.3d)). Wave-encoding (Bilgic et al., 2015) further expends this concept for 3D sequences by applying sinusoidal gradients in both phase encoding directions. In this case, the k-space is sampled along corkscrew trajectories.

2.1.5 MRI Contrasts

Biological tissues consist of various components with different relaxation times T_1 and T_2. The ability to differentiate between image structures is described by the image contrast

$$C(A,B) = \frac{|I(A) - I(B)|}{I_{\text{ref}}}, \tag{2.19}$$

where $I(A)$ and $I(B)$ are the image intensities of two structures A and B and I_{ref} is a reference intensity (for example $I_{\text{ref}} = I(A) + I(B)$). The contrast depends on the sequence type and sequence parameters. The most basic image contrasts exploit differences in proton density (PD), T_1 and T_2. A PD weighted contrast is generated in sequences using long TR and short TE. In this case, the signal intensity is basically independent on relaxation parameters and is only determined by the magnetization M_0. T_1 weighted contrast (intensity variations especially between tissues with different T_1) is achieved if TR is in the order of the typical T_1 values. Intensity differences between tissues with different T_2 values are most prominent in T_2 or T_2^* weighted images acquired with TE in the order of the expected T_2 or T_2^* values and long TR to reduce T_1 weighting of the signal.

Generally, spin echo sequences allow to generate pure T_2 weighted contrast since static inhomogeneities are rephased due to the inversion of the magnetization at $TE/2$. The signal intensity in gradient echo sequences is modulated by T_2^* and is therefore more sensitive to susceptibility changes.

2.1.6 Signal-to-Noise Ratio and Imaging Speed

MR image quality is generally limited by the Signal-to-Noise Ratio (SNR) which is defined as

$$SNR = \frac{S}{\sigma_N}, \tag{2.20}$$

where S denotes the signal level and σ_N the standard deviation of the background noise. The SNR depends on a number of factors. The most important ones are:

- field strength: $SNR \propto B_0$
- voxel size: $SNR \propto \Delta V = \Delta x \Delta y \Delta z$
- acquisition bandwidth or acquisition time: $SNR \propto \sqrt{BW} = 1/\sqrt{t_{acq}}$
- repetition time: longer TR allow a recovery of the longitudinal magnetization and produces high signal intensity
- echo time: longer TE result in signal loss due to relaxation

The SNR is the fundamental limitation in MR imaging since it is generally not possible to speed up the acquisition without any loss of SNR in the final image. However, if the SNR is high enough, there are several ways to accelerate the imaging process.

Different methods to reduce the dead time between data acquisition and the next excitation pulse have been developed. Sequences such as fast low angle shot (FLASH) (Haase et al., 1986) allow to reduce the TR significantly by employing low flip angles for the excitation pulses. Besides, many sequences acquire multiple k-space lines after one excitation and thereby reduce the dead time, as for example echo planar imaging (EPI) (Mansfield, 1977) (cf. Figure 2.3b)), turbo spin echo imaging (TSE) (Hennig et al., 1986) or the magnetization-prepared rapid gradient-echo (MP-RAGE) sequence (Mugler and Brookeman, 1990).

Other methods accelerate image acquisition by reducing the number of phase encoding steps. Sampling schemes such as elliptical scanning (Bernstein et al., 2001) or partial Fourier scanning (Noll et al., 1991) capture only parts the k-space. In addition, imaging speed can be increased by a method called parallel imaging, which is covered in detail in the next section.

2.2 Parallel Imaging

2.2.1 Basics of Parallel Imaging

Despite significant improvements through optimized data acquisition and advanced scanner hardware, reducing MR scan time remains one of the main research areas for MRI. Parallel imaging allows to speed up the imaging process by reducing the amount of k-space data required for image reconstruction. As such, it has become an established technique for accelerated imaging that maintains image contrast and resolution without further demands on the gradient hardware.

Originally, MR receive coil arrays were developed to increase the SNR by use of several small receiver coils instead of a large one. For this purpose, the set of coils, known as phased array (Roemer et al., 1990), is placed around the object in such a way, that their sensitivity volumes slightly overlap and cover the entire region of interest. Each channel is provided with its own receiver chain so that the MR signal is received in parallel. The receiver coils each acquire a spatially-weighted image m_j of the object m

$$m_j(\mathbf{r}) = C_j(\mathbf{r})m(\mathbf{r}), \tag{2.21}$$

where C_j denotes the complex-valued spatial sensitivity profile of the j-th coil of the coil and $\mathbf{r}$ is the position vector. Figure 2.4 shows example images of a phased array with 8 elements with different coil sensitivity profiles.

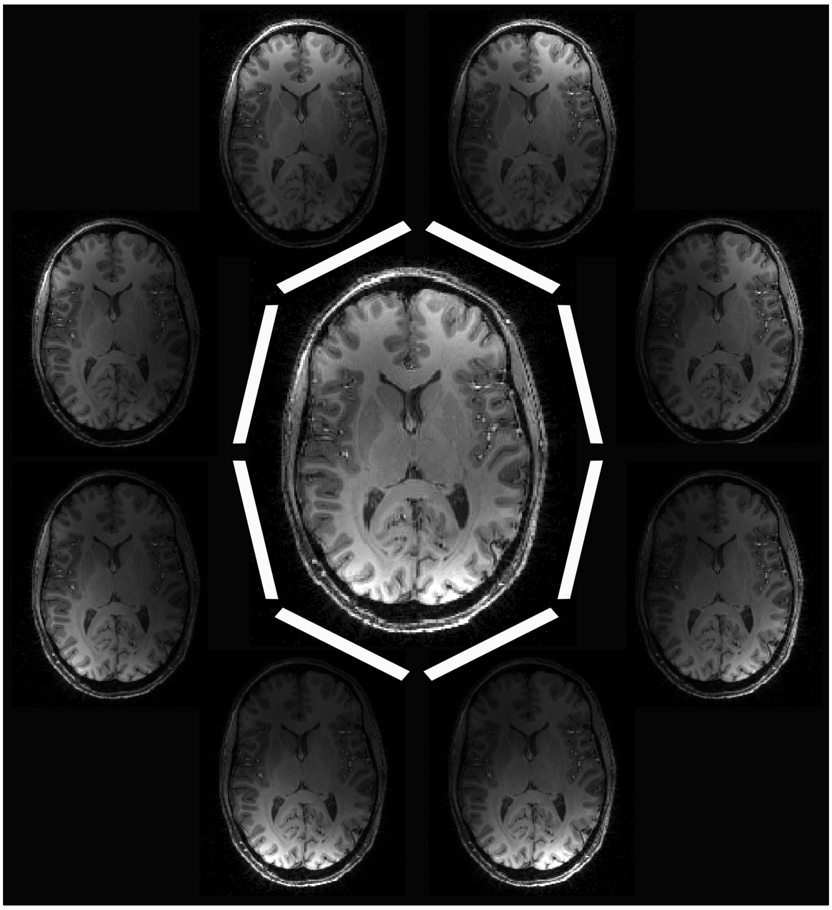

Figure 2.4: Example of a 8-channel receiver array, where every coil acquires a spatially-weighted image of the head. The combination of the coil images covers the object completely and yields an image with improved SNR compared to the image of a single larger coil.

Soon after the development of phased array coils, it was recognized that this additional spatial information from the receiver coil sensitivity profiles could be used to reduce the necessary amount of k-space data. To reduce the scan time, k-space is undersampled by sampling only every R-th line in the phase encoding direction. R is referred to as the reduction or acceleration factor. For 3D imaging, undersampling can be applied to both phase encoding directions. Since the extend of the k-space remains the same, the image resolution is maintained (cf. Equation 2.18). However, according to Equation 2.17, the increased sampling interval of $R\Delta k_y$ leads to a reduction of the FOV by a factor R along this direction. If the object is larger than the reduced FOV, the Nyquist criterion is violated and frequencies from different locations within the object are indistinguishable from each other. This leads to aliasing artifacts in the reconstructed images as depicted in Figure 2.5. To combine the undersampled data from each of the receiver coils into one unaliased image, specific parallel imaging reconstruction algorithms are required.

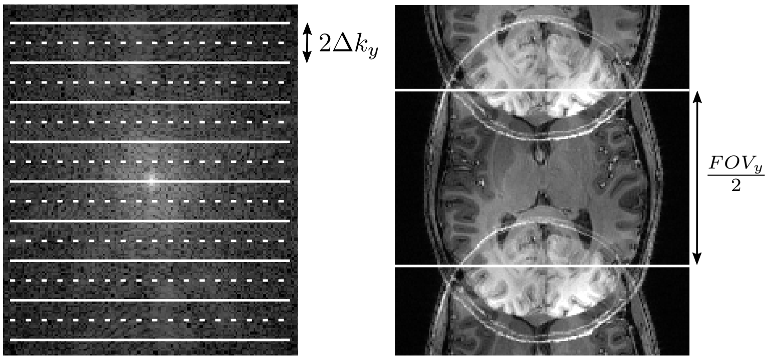

Figure 2.5: Undersampled k-space with acceleration factor $R = 2$ in y-direction, resulting in a reduced FOV with aliasing artifacts. The dashed lines indicate the k-space lines that were not acquired.

2.2.2 Reconstruction Algorithms

Over the years, various techniques such as SMASH (Sodickson and Manning, 1997), AUTO-SMASH (Jakob et al., 1998), SENSE (Pruessmann et al., 1999), SPACE RIP (Kyriakos et al., 2000), PILS (Griswold et al., 2000), VD-AUTO-SMASH (Heidemann et al., 2001), GRAPPA (Griswold et al., 2002), SPIRIT (Lustig and Pauly, 2010) and ESPIRIT (Uecker et al., 2014) have been proposed. The reconstruction algorithms are generally divided into two classes. The first class of algorithms, such as SENSE or PILS, are based on the explicit knowledge of coil sensitivities to reconstruct a single combined image. Other algorithms, such as SMASH or GRAPPA, use the correlation in k-space between multiple channels and neighboring points to reconstruct the missing k-space data of each coil. SENSE-type and GRAPPA-type algorithms are most commonly used in clinical routine and are both introduced in the following. Although the two methods are based on different approaches, they both provide good results with similar reconstruction quality and are well-suited for the reconstruction of accelerated parallel imaging acquisitions.

2.2.2.1 SENSitivity Encoding (SENSE)

SENSE (SENSitivity Encoding) (Pruessmann et al., 1999) explicitly uses coil sensitivity maps to separate aliased pixels. In its simplest form of regularly undersampled Cartesian data, it can be characterized as pixel-by-pixel unfolding in the image domain. Undersampling with a factor of R in the y-direction results in a FOV reduction in this direction and thus to aliasing artifacts. An aliased point at location (x,y) contains information from R equidistantly spaced points (x, y_1), ..., (x, y_R) of the desired full FOV image m. The points are weighted with the spatial sensitivities C_j of the coils. The signal intensity I in each point of the N_c undersampled coil images can be formulated in a linear system of equations:

$$\begin{pmatrix} I_1(x,y) \\ \vdots \\ I_N(x,y) \end{pmatrix} = \begin{bmatrix} C_1(x,y_1) & \dots & C_1(x,y_R) \\ \vdots & \ddots & \vdots \\ C_{N_c}(x,y_1) & \dots & C_{N_c}(x,y_R) \end{bmatrix} \begin{pmatrix} m(x,y_1) \\ \vdots \\ m(x,y_R) \end{pmatrix}. \tag{2.22}$$

A pictorial representation of this equation is shown in Figure 2.6 for an acceleration factor $R = 2$ and two receiver coils.

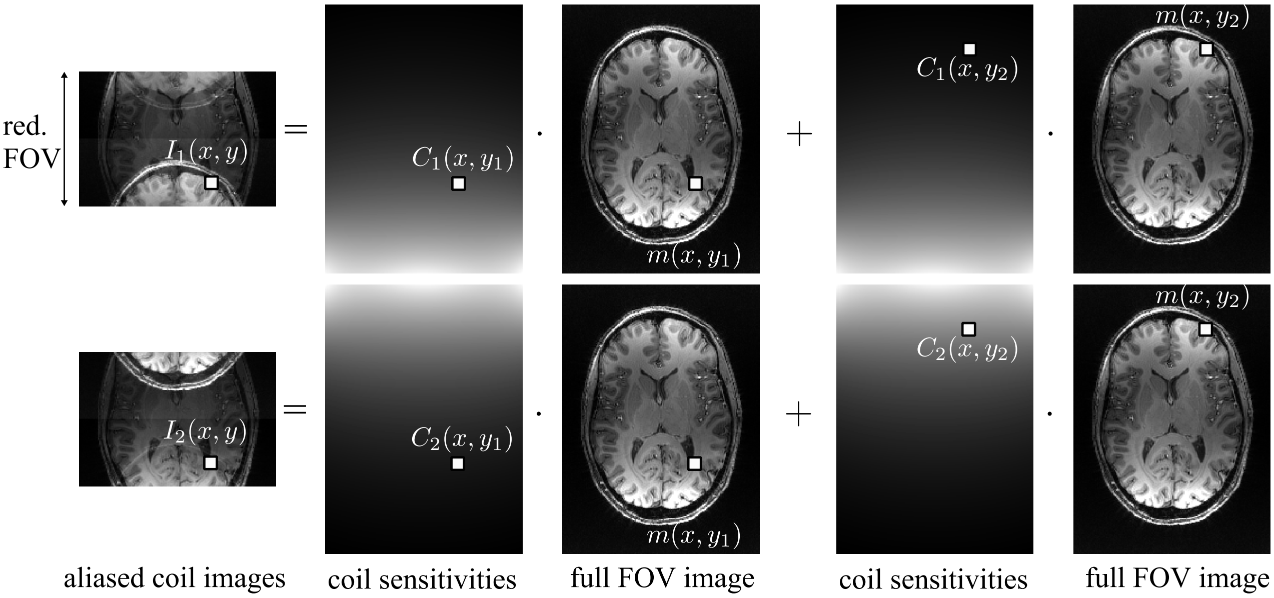

Figure 2.6: Illustration of Equation 2.22 for a parallel imaging acquisition with acceleration factor $R = 2$ and $N = 2$ receiver coils. An aliased point in the coil images contains information from two points of the desired full FOV image that are FOV/2 apart. The points are weighted with the spatial coil sensitivity at their location. If these coil sensitivities are known, the desired full FOV image can be calculated.

In a more general form using the matrix-vector notation, the sensitivity encoding equation can be written as

$$\mathbf{I} = \mathbf{Cm}, \tag{2.23}$$

where $\mathbf{m} \in \mathbb{C}^{N_f}$ represents the signal of N_f folded voxels in the full FOV image, $\mathbf{I} \in \mathbb{C}^{N_c}$ the signal of the aliased voxels of each coil and $\mathbf{C} \in \mathbb{C}^{N_c \times N_f}$ the coil sensitivity matrix. Note that N_f is equal to R for regular undersampling of Cartesian data.

If the complex coils sensitivities are known, the linear system can be solved by calculating the inverse of the coil sensitivity matrix. Usually, the number of coils is larger than the acceleration factor and the non-square matrix is inverted using the Moore-Penrose pseudoinverse

$$\mathrm{pinv}(\mathbf{C}) = (\mathbf{C}^H\mathbf{C})^{-1}\mathbf{C}^H, \tag{2.24}$$

where $\mathbf{C}^H$ denotes the complex conjugate transposed of the matrix $\mathbf{C}$. The final image is then given by

$$\mathbf{m} = (\mathbf{C}^H\mathbf{C})^{-1}\mathbf{C}^H\mathbf{I}. \tag{2.25}$$

For simplicity, the noise characteristics of the different receiver channels are not considered in Equation 2.25. A detailed description accounting for noise correlation can be found in (Pruessmann et al., 1999).

The inversion problem given by Equation 2.25 provides a framework for reconstruction of arbitrary k-space data. However, only in the case of regularly undersampled Cartesian data, R points from well-known location are folded into one point. This allows to break down the problem into a series of independent small equations for each group of aliased pixels (cf. Equation 2.22) and requires little computation power. For the general SENSE reconstruction with arbitrary k-space sampling patterns, the aliasing is more complex since every point can potentially alias with all the other points. In this case, solving the SENSE equation is numerically complex and the reconstruction is performed iteratively (Pruessmann, 2001).

A successful SENSE reconstruction relies on an explicit knowledge of coil sensitivity maps. However, an accurate and robust coil sensitivity estimation is often very difficult and even small errors can result in artifacts in the reconstructed image. Coil sensitivities can be estimated from a separate low resolution dataset that covers the whole FOV or from a fully sampled central part of a variable-density k-space acquisition (McKenzie et al., 2002). A simple method to approximate the coil sensitivities is to divide the coil images by the sum of squares combination of all coils. To increase robustness, it is helpful to smooth the maps using polynomial fitting (Pruessmann et al., 1999).

2.2.2.2 GeneRalized Partially Parallel Acquisitions (GRAPPA)

The basic idea of GeneRalized Partially Parallel Acquisitions (GRAPPA) (Griswold et al., 2002) is to calculate missing k-space lines by appropriate combination of the acquired neighboring lines in the multi-coil k-space. The GRAPPA method is based on SMASH (Sodickson and Manning, 1997) and further improvements of SMASH called AUTO-SMASH (Jakob et al., 1998) and VD-AUTO-SMASH (Heidemann et al., 2001). The principles of k-space parallel imaging reconstruction can be understood by examining the MR signal $S_j(k_y)$ received by coil j:

$$S_j(k_x, k_y) = \int_x \int_y \rho(x, y) C_j(x, y) e^{-i2\pi k_x x} e^{-i2\pi k_y y} \mathrm{d}x\mathrm{d}y. \tag{2.26}$$

The spin density $\rho(x, y)$ of the object is weighted with the corresponding sensitivity profile $C_j(x, y)$ at this location. Similarly, the signal at k-space location $k_y + m\Delta k_y$ is given by

$$S_j(k_x, k_y + m\Delta k_y) = \int_x \int_y \rho(x, y) C_j(x, y) e^{-i2\pi k_x x} e^{-i2\pi (k_y + m\Delta k_y) y} \mathrm{d}x\mathrm{d}y. \tag{2.27}$$

The only difference between shifted k-space lines are spatial harmonics of order m. GRAPPA approximates the missing harmonic functions for each individual coil j by a linear combination of the coil sensitivity functions of all coils N_c

$$C_j(x, y) e^{-i2\pi m\Delta k_y y} \approx \sum_{k=1}^{N_c} w(m, j, k) C_k(x, y), \tag{2.28}$$

with the weighting factor $w(m, j, k)$ for the mth spatial harmonic. The signal of acquired k-space lines from all coils can thus be used to approximate the signal from missing lines

$$\begin{aligned} S_j(k_x, k_y + m\Delta k_y) &\approx \int_x \int_y \rho(x, y) \sum_{k=1}^{N_c} w(m, j, k) C_k(x, y) e^{-i2\pi k_x x} e^{-i2\pi k_y y} \mathrm{d}x\mathrm{d}y \\ &= \sum_{k=1}^{N_c} w(m, j, k) S_k(k_x, k_y). \end{aligned} \tag{2.29}$$

The original GRAPPA implementation proposed by Griswold et al. uses a block of multiple k-space lines to calibrate the weighting factors. This was later improved and the kernel size was extended to points in the readout direction (Wang et al., 2005). For a kernel size of $N_x^{src} \times N_y^{src}$, the reconstruction can be written as

$$S_j(k_x, k_y + m\Delta k_y) = \sum_{k=1}^{N_c} \sum_{a=0}^{N_x^{src}-1} \sum_{b=0}^{N_y^{src}-1} w(m, j, k, a, b) S_k(k_x + a\Delta k_x, k_y + bR\Delta k_y), \tag{2.30}$$

where R represents the acceleration factor and a and b iterate over all acquired points within the kernel. For the $N_c(R-1)$ missing k-space points, Equation 2.30 can be written in matrix form

$$\mathbf{T} = \mathbf{w}\mathbf{S}, \tag{2.31}$$

where the vector $\mathbf{T} \in \mathbb{C}^{N_c(R-1)}$ represents the missing target points, $\mathbf{S} \in \mathbb{C}^{N_c N_x^{src} N_y^{src}}$ contains the acquired source point and the $\mathbf{w} \in \mathbb{C}^{N_c(R-1) \times N_c N_x^{src} N_y^{src}}$ is the weighting matrix referred to as GRAPPA weights.

While SENSE reconstructs one single combined image, GRAPPA calculates the missing k-space lines for every coil and obtains separate full FOV coil images. These images can be combined with a method of choice, often the sum of squares combination. The GRAPPA reconstruction can be visualized as sliding the kernel from point to point through k-space and multiplying the weights by the kernel source points to determine the missing target points. A schematic description of the GRAPPA reconstruction is given in Figure 2.7 for a GRAPPA kernel size of 3×2.

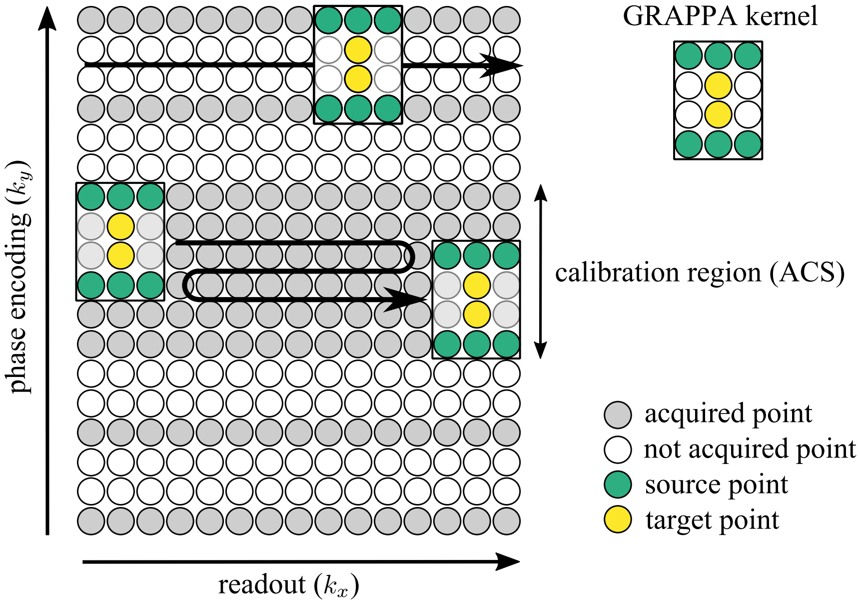

Figure 2.7: Schematic description of the GRAPPA reconstruction of Cartesian data undersampled by a factor $R = 3$ using a reconstruction kernel of size 3×2. For simplicity, only the k-space of one coil is shown. The kernel, however, uses source points from all coils to determine the target points in one coil. In a first step, the reconstruction kernel is moved to all possible positions within the fully encoded calibration region and collects for each position the $R - 1 = 2$ target points and the $N_x^{src} \cdot N_y^{src} = 3 \cdot 2$ source points in each of the coils. The appropriate weights are found by fitting the source points to the target points. These weights are then applied in a second step to the undersampled data to determine the missing target points of all coils at the corresponding kernel positions.

GRAPPA reconstructions, like SENSE, require a calibration dataset which contains the sensitivity informations of the different coils. However, GRAPPA uses the calibration data in k-space and does not require explicit knowledge of the coil sensitivity profiles. The GRAPPA kernel is moved to every possible position of the full sampled calibration k-space, called autocalibration signal or ACS, and collects source points $\mathbf{S}_{\text{ACS}}$ and target points $\mathbf{T}_{\text{ACS}}$. The weights required for the GRAPPA reconstruction can be found by inverting Equation 2.31:

$$\mathbf{w} = \mathbf{T}_{\text{ACS}} \cdot \text{pinv}(\mathbf{S}_{\text{ACS}}). \tag{2.32}$$

At least $N_x^{src}N_y^{src}$ kernel repetitions are required within the ACS to determine $\mathbf{w}$. However, for robust calibration, more ACS data is required in practice. The size of the GRAPPA kernel can be chosen for every reconstruction. Larger kernel sizes improve the reconstruction quality, but require a larger calibration dataset and increase the computation time for the reconstruction (Bauer et al., 2011). The ACS data can be obtained from a fully sampled k-space center or from a separate calibration scan. If the ACS are collected in the k-space center of the accelerated acquisition, the calibration data can be included in the final reconstruction to improve image quality. The effective acceleration factor of the parallel imaging acquisition is given by

$$R_{\text{eff}} = \frac{R}{1 + \frac{N_{\text{ACS}}}{Ny}(R-1)}, \tag{2.33}$$

where N_y is the size of the fully encoded k-space in k_y-direction and N_{ACS} the number of ACS lines.

GRAPPA is a Cartesian approach that requires a regularly sampled Cartesian k-space. However, generalizations of GRAPPA have been applied to specific non-Cartesian trajectories, where similar undersampling patterns exist (Breuer et al., 2008; Griswold et al., 2003; Heidemann et al., 2006). A GRAPPA-based reconstruction for non-Cartesian wave trajectories (cf. Figure 2.3d)) with parallel imaging acceleration, namely wave-CAIPI, was proposed in (Jolanda M. Schwarz, Eberhard D. Pracht, Brenner, et al., 2018) and is subject of Chapter 3.

2.2.2.3 GRAPPA Operator Gridding (GROG)

GRAPPA Operator Gridding (GROG) (Seiberlich et al., 2007) is an extension of GRAPPA that allows to convert non-Cartesian data into Cartesian data by shifting the data points to their nearest Cartesian location. Afterwards, in the regridding process, data can be reconstructed using the Cartesian GRAPPA reconstruction described above.

GROG is based on the GRAPPA Operator formalism described by Griswold et al. (Griswold et al., 2005) which has several properties useful for gridding. It is the special case of GRAPPA, where the number of target and source points are the same. For a shift of Δk and a single source and target point, Equation 2.30 can be written as

$$\mathbf{S}(k_x, k_y + \Delta k_y) = \mathbf{G}_y \mathbf{S}(k_x, k_y), \tag{2.34}$$

where the GRAPPA operator $\mathbf{G}_y \in \mathbb{C}^{N_c \times N_c}$ contains the GRAPPA weights for a shift of Δk_y in y-direction. For a shift of two k-space points, the GRAPPA operator can be applied twice. The resulting signal can be expressed as

$$\mathbf{S}(k_x, k_y + 2\Delta k_y) = \mathbf{G}_y \mathbf{S}(k_x, k_y + \Delta k_y) = \mathbf{G}_y^2 \mathbf{S}(k_x, k_y). \tag{2.35}$$

This significant characteristic of the GRAPPA operator can be used for an arbitrary small shift $\delta_y \Delta k_y$:

$$\mathbf{S}(k_x, k_y + \delta_y \Delta k_y) = \mathbf{G}_y^{\delta_y} \mathbf{S}(k_x, k_y). \tag{2.36}$$

Furthermore, multidimensional shifts can be described by combining one-dimensional GRAPPA operators

$$\mathbf{S}(k_x + \delta_x \Delta k_x, k_y + \delta_y \Delta k_y, k_z + \delta_z \Delta k_z) = \mathbf{G}_x^{\delta_x} \mathbf{G}_y^{\delta_y} \mathbf{G}_z^{\delta_z} \mathbf{S}(k_x, k_y, k_z). \tag{2.37}$$

The GRAPPA operator along each direction only needs to be determined once for a defined step size, typically Δk. It can be obtained like the GRAPPA weights (cf. Equation 2.32) by collecting source and target points from ACS data and inverting Equation 2.34 by the use of the pseudo-inverse. The matrix operations $\mathbf{G}^{\delta}$ can be performed by diagonalizing the GRAPPA operator:

$$\mathbf{G} = \mathbf{E} \cdot \mathbf{V} \cdot \mathbf{E} \quad \rightarrow \quad \mathbf{G}^{\delta} = \mathbf{E} \cdot \mathbf{V}^{\delta} \cdot \mathbf{E}. \tag{2.38}$$

Hereby, the matrix $\mathbf{E}$ contains the eigenvectors and the diagonal matrix $\mathbf{V}$ contains the eigenvalues of $\mathbf{G}$.

In contrast to the GRAPPA weights, the GRAPPA operator only employs one source point per target point. Because of the small amount of fitting data, high spatial harmonics (corresponding to larger shifts in k-space) cannot be fitted accurately and the GRAPPA operator is generally more susceptible to noise than GRAPPA weights. The GRAPPA operator is therefore only suitable for small k-space shifts. Besides, since the formalism uses parallel imaging concepts, it strongly depends on the sensitivity variations within the coil array.

The GROG technique represents an alternative method to conventional convolution gridding (Jackson et al., 1991). Using the properties of the GRAPPA operator, GROG enables the regridding of non-Cartesian data points to a Cartesian grid as schematically illustrated in Figure 2.8. Since only one source point is involved in the GRAPPA operator formalism, any source point can be shifted to any nearby location. Deviations from the Cartesian grid are not restricted to non-Cartesian acquisitions. They can also result from distortions of the magnetic field as described in Chapter 2.3. Since GROG is well suited to perform small k-space shifts, this technique is used in Chapter 4 to correct for physiological field fluctuations.

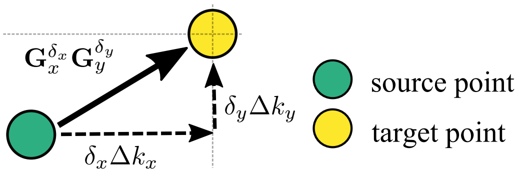

Figure 2.8: Illustration of GROG. Using the GRAPPA operators $\mathbf{G}_x$ and $\mathbf{G}_y$, a non-Cartesian data point (green point) is shifted by $\delta_x \Delta k_x$ along the x-direction and by $\delta_y \Delta k_y$ along the y-direction to a Cartesian grid (yellow point).

2.2.3 Parallel Imaging Reconstruction Quality

SNR and g-Factor

The main limitation of parallel imaging is the loss in SNR due to the subsampling of k-space. Therefore, acquisitions with a general high SNR, such as for example ultra-high field applications, are best suited for parallel imaging accelerations. The SNR in the reconstructed images is decreased by the square root of the acceleration factor ($\sqrt{R}$). Furthermore, noise is amplified by a spatially varying term which depends on the encoding efficiency of the receiver coils. It is described by the so-called coil geometry factor or g-factor that arises from the geometry and the properties of the receiver coils and the sampling scheme. If the coil sensitivities are completely independent from another, the signal contribution from each location can be well distinguished and the g-factor is equal to one. Otherwise, the g-factor can be larger than one and the SNR decreases. The relationship between the SNR of the fully sampled image compared to the image of the reduced dataset is given by

$$SNR_{acc} = \frac{SNR_{full}}{\sqrt{R} \cdot g}. \tag{2.39}$$

The g-factor was introduced by Pruessmann et al. (Pruessmann et al., 1999) for SENSE reconstructions and has become the standard method for assessing parallel imaging algorithms. The g-factor at pixel p can be directly calculated from the coil sensitivity matrix of the SENSE equation according to

$$g_p = \sqrt{[(C^H C^{-1})^{-1}]_{p,p}[C^H C]_{p,p}}, \tag{2.40}$$

where $[\dots]_{p,p}$ represents the diagonal matrix elements. Furthermore, g-factor maps can be calculated analytically for GRAPPA reconstructions from the GRAPPA kernel as described in (Breuer et al., 2009).

A general SNR quantification approach that can also be used to evaluate different parallel imaging methods is the pseudo multiple replica (PMR) method (Robson et al., 2010). It is a Monte Carlo approach that follows the noise propagation through the image reconstruction. It is based on the assumption, that repeatedly acquired k-space data only differ in their noise level, while the signal remains the same. Noise added in k-space results in characteristic spatial noise variance in the reconstructed image. Random Gaussian noise is generated, then scaled and correlated using the covariance matrix obtained from a noise prescan, and finally added to the subsampled k-space data. This data is reconstructed using the reconstruction matrix obtained from reconstruction of the original dataset. These steps are usually repeated many times so that at least 100 replicas are generated. The unaccelerated image noise is found from a stack of replicas of noise-only fully sample k-spaces which are reconstructed using a simple fast Fourier transform and optimal complex coil combination (Roemer et al., 1990). The noise standard deviation at each pixel location corresponds to the standard deviation of the real or imaginary part of the pixel value through the stack of replicas. The g-factor can be calculated from the noise standard deviations of the subsampled (σ_{acc}) and the fully sampled replicas (σ_{full}):

$$g_{PMR} = \frac{\sigma_{acc}}{\sqrt{R} \cdot \sigma_{full}}.$$

Additionally, SNR maps can be calculated according to Equation 2.20, using the original reconstructed image and σ_{acc}. The noise distribution appears different in SENSE and GRAPPA reconstructed images. While it is more uniformly distributed in GRAPPA, SENSE images generally show more spatial variation of noise (Thunberg and Zetterberg, 2007).

Root-Mean-Square Error

Besides the noise enhancement, high acceleration factors can lead to residual aliasing artifacts in the reconstructed images. Small errors in the sensitivity maps are often amplified and result in a visible decrease in image quality. A common method to evaluate the quality of the reconstructed image is the root-mean-square error (RMSE). For parallel imaging, it serves as a measure of deviations between the reconstructed images of the subsampled and the fully sampled reference data. The RMSE error is defined as

$$RMSE = \sqrt{\frac{\sum_p (m_p - m_{p,ref})^2}{\sum_p m_{p,ref}^2}},$$

where m_p and $m_{p,ref}$ denote the values of pixel p in the accelerated image and in the non-accelerated reference image, respectively.

Regularization

One common strategy to increase the SNR in parallel imaging reconstructions is the application of regularization. However, over-regularization can lead to severe image artifacts and therefore regularization often is a compromise between SNR and image artifacts. In the regularization process, additional assumptions are added to an ill-posed problem in order to improve the conditioning of the problem and enable a direct numerical solution. A commonly used strategy is the Tikhonov regularization. Regularization of the pseudoinverse (Equation 2.41) helps to obtain a stable inversion in spite of insufficient coil sensitivity variations or insufficient calibration data

$$\mathrm{pinv}(\mathbf{C}) = (\mathbf{C}^H \mathbf{C} + (\Gamma^H \Gamma))^{-1} \mathbf{C}^H, \tag{2.41}$$

with the Tikhonov matrix Γ. Often, the so-called L_2 regularization is chosen, where Γ is a multiple of the identity matrix $\Gamma = \lambda \mathbb{1}$ with the regularization parameter λ. Regularization can be applied to both, SENSE and GRAPPA, and leads to a noise reduction in the reconstructed images.

2.2.4 3D Parallel Imaging

In 3D MRI, spatial encoding is performed using phase encoding gradients along two spatial dimensions (cf. Section 2.1.4.2). These acquisitions allow an acceleration in both phase encoding directions and can thus benefit from coil sensitivity variations in two dimensions. The second phase encoding direction is commonly refereed to as partition encoding direction.

For an acceleration factor R_y in y-direction and R_z in z-direction, the total acceleration factor is given by $R = R_y \cdot R_z$ and consequently R pixels are folded on top of each other in case of regularly sampled Cartesian imaging. As an example, the aliased images for a 4-fold accelerated dataset with different subsampling schemes are shown in Figure 2.9. Dividing the acceleration in the phase and partition encoding directions spreads the aliasing more efficiently over the whole image, resulting in a better reconstruction quality and lower g-factor values (cf. Figure 2.9c)) .

The coil sensitivity variations can be exploited even more efficiently using the CAIPIRINHA (Controlled Aliasing In Parallel Imaging Results IN Higher Acceleration) concept (Breuer et al., 2005, 2006). The appearance of the aliasing is modified by a shift of k-space points along the partition encoding direction as shown in Figure 2.9d) for a shift of $\Delta = 1$. The shifted k-space sampling of 2D CAIPIRINHA can be implemented in the 3D MRI sequence by adjusting the phase and partition encoding gradients. The benefit of a CAIPIRINHA shift strongly depends on the sampling pattern, the FOV and the coil sensitivity variations.

The reconstruction of 3D parallel imaging is very similar to 2D imaging data. A common approach for GRAPPA is the 2D GRAPPA method (Blaimer et al., 2006) that employs a 3D reconstruction kernel with source points taken from the 3D neighborhood. The missing k-space points are generated by a linear combination of these source points from all coils. Examples of possible GRAPPA kernels for different sampling schemes are shown in Figure 2.9.

Most 3D parallel imaging methods exploit the coil sensitivity variations along phase and partition encoding direction, but not along the readout direction. Bilgic et al. (Bilgic et al., 2015) proposed an extension of 2D CAIPIRINHA, the wave-CAIPIRINHA (wave-CAIPI) method, which allows to additionally spread the aliasing in the readout direction. The basics of wave-CAIPI are discussed in Chapter 3 and a GRAPPA based reconstruction method is proposed. The reconstruction is employed for highly accelerated T_1 and T_2 weighted imaging and compared to conventional 2D CAIPIRINHA sampling.

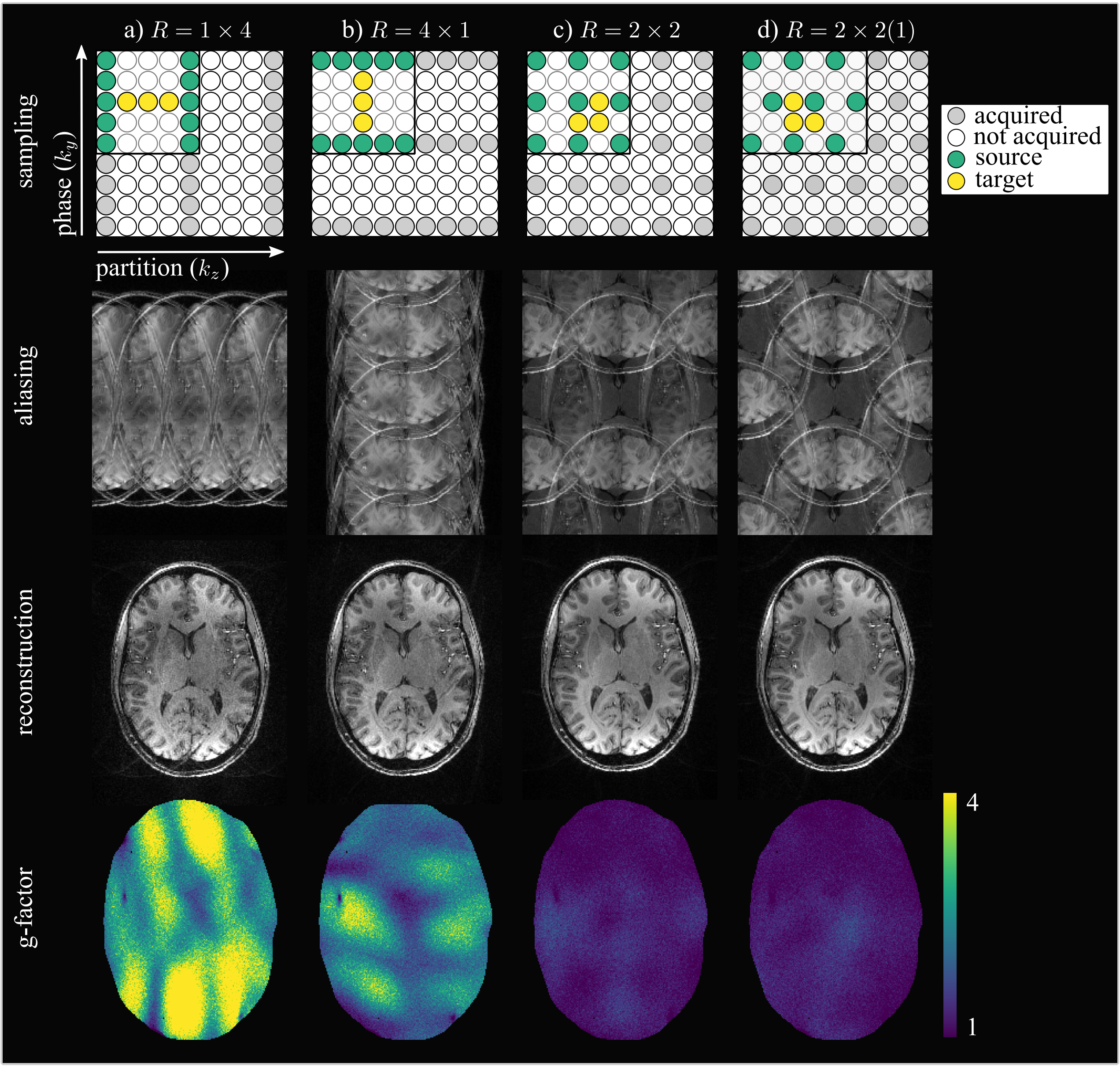

Figure 2.9: Different k-space sampling schemes for 4-fold accelerated 3D MRI. For simplicity, the fully sampled readout direction is omitted. For a subsampling along partition or phase encoding direction ($R = 1 \times 4$ or $R = 4 \times 1$), the aliasing only appears along this direction. If the dataset is reduced in both directions ($R = 2 \times 2$), the aliasing is spread more efficiently over the image. The parallel imaging reconstruction (here GRAPPA) strongly benefits from the coil sensitivity variations along both directions. Image artifacts and the g-factor are clearly reduced. 2D CAIPIRINHA sampling with shift $\Delta = 1$ ($R = 2 \times 2(1)$) further modifies the appearance of aliasing. This results in a further small g-factor decrease. The example reconstruction kernels chosen for the GRAPPA reconstruction are depicted in the sampling scheme (top row) with source and target points marked in green and yellow, respectively.

2.3 Magnetic Field Monitoring

There is a large number of mechanisms causing deviations from the nominal magnetic field evolution during MRI acquisitions that can result in artifacts in the reconstructed images. Field distortions in general include changes of the global magnetic field δB_0, linear first-order field fluctuations which lead to deviations $\delta\mathbf{k}(t)$ from the nominal k-space trajectory, or even higher-order field changes. In presence of up to first-order field distortions, the signal equation (Equation 2.16) changes into

$$S(\mathbf{k},t) = \int\limits_{volume} M_{x,y}(\mathbf{r},t=0)e^{-i\gamma\delta B_0 t}e^{-i2\pi(\mathbf{k}+\delta\mathbf{k}(t))\mathbf{r}}\mathrm{d}^3r. \tag{2.42}$$

For a successful image reconstruction based on the acquired MR signal, it is necessary that the signal can be accurately assigned to points in k-space. Therefore, the exact knowledge of the main magnetic field and the time course of the applied gradient fields is required.

2.3.1 Origin of Field Distortions

Field distortions generally have their origin in MR hardware imperfections or in the physiology of the subject in the scanner.

Commercial MR systems typically meet high field homogeneity requirements within a defined volume in the scanner bore. However, a wide range of hardware-related mechanisms lead to deviations from the nominal field dynamics. These mechanisms include gradient delays, mechanical vibrations due to fast gradient switching (Yuhua et al., 2000), bandwidth limitation of the gradient amplifier, thermal effects (Foester et al., 2014), and eddy currents induced by temporally and spatially changing magnetic fields in gradient coils and other conducting structures of the MR system (Boesch et al., 1991; Liu et al., 1994; Spees et al., 2011). To reduce the effect of eddy currents, commercial MR scanner employ gradient and RF eddy current pre-emphasis during transmission and signal eddy current compensation (ECC) during reception.

Additionally, the magnetic field is distorted when an object is placed in the homogeneous background field due to differences in magnetic susceptibility. The magnetic susceptibility of the human body is close to that of water and differs from the susceptibility of the surrounding air by $\Delta\chi \approx 10\,\mathrm{ppm}$. During in-vivo imaging, the most significant field distortions occur at these interfaces. This is especially problematic in brain imaging, where the ear canals and air-filled sinuses are very close to regions of interest in the brain. Susceptibility-induced field perturbations are proportional to the background magnetic field B_0 and can lead to maximum field changes (Schenck, 1996)

$$\Delta B_{max} = \Delta\chi \cdot B_0 \tag{2.43}$$

and are therefore particularly prominent at higher field strength. These field deviations inside the object are spatially varying, but temporally static, and the field homogeneity is typically adjusted using so-called shim coils. An overview of the principles of shimming can be found in (Jezzard, 2006). However, physiological motion such as respiration, limb motion or cardiac pulsation changes the magnetic susceptibility distribution in the magnetic bore and gives rise to spatio-temporal field fluctuations. These field changes even extend to locations at some distance from the moving tissue (Van de Moortele et al., 2002; Versluis et al., 2010). For example chest movement due to respiration disturbs the spatial field distribution and thereby influences the spatial encoding in the brain.

2.3.2 Effects of Field Distortions

The aforementioned sources of field distortions influence the signal encoding (cf. Equation 2.42) and lead to a wide range of artifacts in the reconstructed images. This can render MR images difficult to interpret. The appearance and severity of these artifacts depend on the characteristics of the field distortions during image acquisition and on the way the k-space is sampled.

Inhomogeneities or perturbations of the main magnetic field cause frequency shifts which in turn lead to geometrical distortions (displacement of pixel locations), intensity changes or blurring of the MR image. While for example changes in susceptibility lead in particular to geometrical distortions in Cartesian acquisitions, they mainly appear as image blurring in non-Cartesian acquisitions.

Deviations from the nominal k-space trajectory, for example due to eddy current or gradient delays, lead to an incorrect assignment of the signal to positions in k-space. For non-Cartesian acquisitions (e.g. spirals or wave-sampling), the k-space is sampled on a non-uniform grid. Small deviations from the expected trajectory can lead to severe artifacts in the reconstructed image. Due to the regular sampling scheme of Cartesian acquisitions, the effect on Cartesian images is much smaller. Thus, a trajectory shift in readout direction due to gradient delays only produces a linear phase over the image. However, gradient delays have a severe effect on EPI acquisitions. Due to the k-space coverage with alternating direction of successively sampled lines, they cause a relative k-space shift between even and odd lines. This results in replicas of the object at shifted positions in the final image, so called ghosting artifacts.

Slow k-space sampling schemes are generally more robust regarding eddy-currents-induced field changes, since they operate less at the gradient system limits. However, due to their usually long acquisition times, they are more affected by field fluctuations due to motion which can lead to ghosts, image blurring or intensity variations.

2.3.3 Field Measurements

Many of the image artifacts caused by magnetic field distortions can be corrected if the magnetic field and the time course of the applied gradient fields are known.

2.3.3.1 MRI-based Methods

Various MRI-based methods have been proposed to measure reproducible, hardware-related B_0 field variations (Crozier et al., 1992; Ordidge and Cresshull, 1986), effective k-space trajectories (Duyn et al., 1998; Mason et al., 1997; Tan and Meyer, 2009; Zhang et al., 1998) or gradient delays (Peters et al., 2003; Robison et al., 2010). In EPI acquisitions, the problem of non-ideal k-space is typically addressed by using navigator echoes (Buonocore and Gao, 1997). Many methods for the determination of physiological B_0 fluctuations are also based on navigator MRI techniques, where phase variations are extracted from navigator scans (Hu and Kim, 1994; Pfeuffer et al., 2002; Versluis et al., 2010).

However, all those field measurement methods require changes in the MR sequence and additional scan time or a separate calibration scan. Furthermore, they do not allow to measure field dynamics concurrently with the imaging process.

2.3.3.2 NMR Field Probes for Field Monitoring

The field monitoring approach used in this thesis is based on a miniaturized NMR experiment inside a confined volume, the so-called field NMR probe (Barmet et al., 2009; De Zanche et al., 2008). In contrast to the MRI-based methods, they allow field monitoring simultaneously to the imaging process.

An NMR field probe consists of a small droplet of an NMR active liquid which is encased in a glass capillary, as schematically shown in Figure 2.10. The glass capillary is surrounded by a solenoid coil for sample excitation and signal reception. To minimize phase dispersion within the probe droplet due to inhomogeneities caused by different susceptibilities, all components are susceptibility-matched. The FID signal of the probe is measured after applying a short excitation pulse at the approximate Larmor frequency of the probe nucleus. If the NMR active droplet is small enough, the phase evolution of the magnetization in the magnetic field B can be summarizes by one value

$$\varphi(t) = \gamma \int\limits_0^t B(\mathbf{r}_p, \tau) \mathrm{d}\tau + \varphi_0, \tag{2.44}$$

where γ is the gyromagnetic ratio of the nucleus used in the field probe, φ_0 is the initial phase after excitations and $\mathbf{r}_p$ denotes the location of the probe.

Due to their high gyromagnetic ratio and therefore high NMR sensitivity, hydrogen ($\frac{\gamma_\mathrm{H}}{2\pi} = 42.58\,\mathrm{MHz/T}$) or fluorine ($\gamma_\mathrm{F}/(2\pi) = 40.05\,\mathrm{MHz/T}$) are generally used as the NMR active material in the field probe. The advantage of ^{19}F NMR field probes is that they allow to measure the field concurrently with the imaging experiment, which is usually operating at the proton frequency. The difference in resonance frequencies of ^{1}H and ^{19}F is large enough to allow for spectral separation of the signals. To gain information on the total field dynamics during multiple acquisitions, the field probe system must allow for a fast repeated probe excitation. To this end, T_1 of the field probes is reduced using relaxing gradients/contrast agents, while keeping T_2 as long as possible.

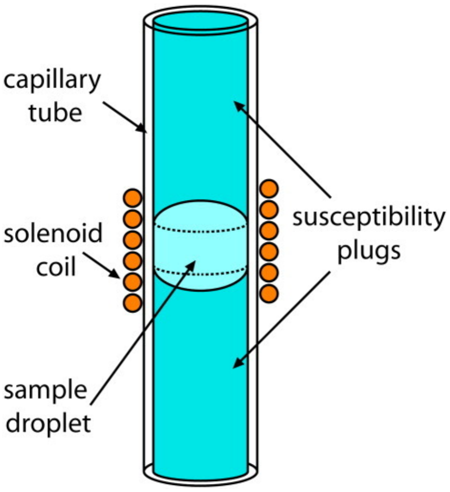

Figure 2.10: Schematic representation of an NMR field probe. (Figure adapted from (De Zanche et al., 2008).)

A single field probe enables the measurement of the time evolution of the magnetic field at one spatial position. By combining several probes, it is possible to extract information on the spatiotemporal distribution of the magnetic field. Assuming a smooth field with origin outside the volume of interest, the magnetic field allows spatial expansion on a low number L of spatially smooth basis functions (Barmet et al., 2008) and the signal phase of a probe at position $\mathbf{r}_p$ can be expressed as

$$\varphi_p(t) = \sum_{i=1}^{L} b_i(\mathbf{r}_p)k_i(t) + \varphi_{0,p}. \tag{2.45}$$

Here, $b_i(\mathbf{r}_p)$ denote the spatial basis functions and $k_i(t)$ the corresponding phase coefficients. The signal phase for N probes distributed within the volume can be written in the vector-matrix notation

$$\boldsymbol{\varphi}(\boldsymbol{t}) = \mathbf{P}\mathbf{k}(t) + \boldsymbol{\varphi}_0, \tag{2.46}$$

with the calibration matrix

$$\mathbf{P} = \begin{bmatrix} b_1(\mathbf{r}_1) & \dots & b_L(\mathbf{r}_1) \\ \vdots & \ddots & \vdots \\ b_1(\mathbf{r}_N) & \dots & b_L(\mathbf{r}_N) \end{bmatrix}. \tag{2.47}$$

The phase coefficients $k_i(t)$ are obtained from the pseudo-inverse $\mathbf{P}^+$ of $\mathbf{P}$:

$$\mathbf{k}(t) = \mathbf{P}^+ \left(\boldsymbol{\varphi}(t) - \boldsymbol{\varphi}_0\right). \tag{2.48}$$

To solve Equation 2.48, the initial phase of every probe $\varphi_{0,p}$ and their position $\mathbf{r}_p$ must be known.

They can be determined from the FID signal of the probe array during a short calibration scan. Therein, the probe signal is first measured without any magnetic field gradient and then three separate short measurements under constant gradients along the x, y and z-direction are performed.

One well-suited choice of basis functions are spherical harmonics. Real-valued spherical harmonics of up to second-order and the corresponding phase coefficients are listed in Table 2.1. To determine phase coefficients of up to first-order, at least 4 field probes are required. They contain a spatially uniform zero-order phase coefficient k_0 and linear first-order coefficients k_x, k_y and k_z, which correspond to the spatial frequency variables (cf. Equation 2.14) and describe the actual k-space trajectory. Higher-order field monitoring (Vannesjo et al., 2012; Wilm et al., 2011) accordingly requires a larger number of field probes.

order	spherical harmonic	phase coefficient
0	1	k_0
1	x	k_x
	y	k_y
	z	k_z
2	xy	k_4
	yz	k_5
	$2z^2 - x^2 - y^2$	k_6
	xz	k_7
	$x^2 - y^2$	k_8

Table 2.1: Real-valued spherical harmonics up to second-order as basis functions and corresponding phase coefficients.

The positioning of a field probe array is exemplary shown in Figure 2.11 for brain imaging using a 32-channel head receive coil.

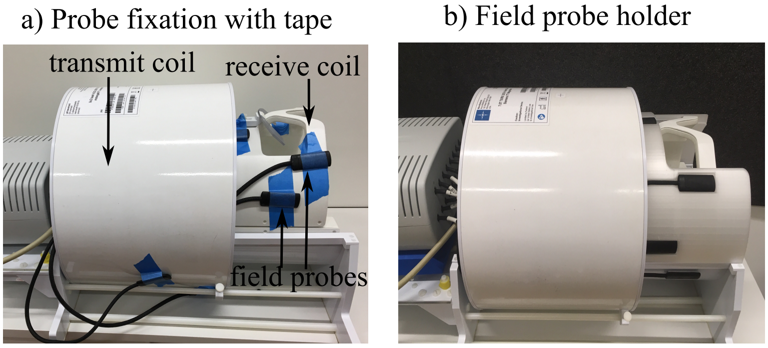

Figure 2.11: Exemplary positioning of 16 field probes around a 32-channel head receive coil using a) tape or b) a replaceable field probe holder (Brunheim et al. 2020) for probe fixation.

The excitation of the field probes is controlled by an external trigger from the MR scanner. To use the field measurements for image reconstruction, the delay between the MR system and the field camera must be known. Therefore, a short synchronization measurements is performed at the beginning of the actual imaging experiment. During this measurement, the field probe system plays out amplitude-modulated RF pulses at the MR system frequency (proton frequency). This signal is received by both, the scanner and probe system, and the delay is determined by correlation of the two acquired datasets.

3

GRAPPA-based Wave-CAIPI Reconstruction

This chapter was partly adapted from:

Schwarz JM, Pracht ED, Brenner D, Reuter M and Stöcker T, 2018. GRAPPA reconstructed wave-CAIPI MP-RAGE at 7 Tesla. Magnetic Resonance in Medicine 80, 2427-2438.

Schwarz JM, Pracht ED and Stöcker T, 2018. GRAPPA reconstructed 3D wave-CAIPI TSE at 7 Tesla. Proceedings of the 26th Scientific Meeting of the International Society for Magnetic Resonance in Medicine, p. 0938.

3.1 Introduction

As discussed in Section 2.2, parallel imaging techniques have been shown to be a powerful and robust method to reduce the acquisition time of MRI experiments. By taking advantage of the spatially varying coil sensitivity profiles, the number of encoding steps is reduced in the phase and partition encoding direction. The resulting aliasing artifacts are corrected by image reconstruction algorithms, such as GRAPPA (Generalized Autocalibrating Partially Parallel Acquisitions) (Griswold et al., 2002) and SENSE (SENSitivity Encoding) (Pruessmann et al., 1999). The 2D CAIPIRINHA (Controlled Aliasing in Volumetric Parallel Imaging) acquisition scheme (Breuer et al., 2006) modifies the 2D aliasing and thereby exploits the coil sensitivity variations more efficiently in the phase and partition encoding direction. By applying an additional oscillating phase encoding gradient G_{p1} during the readout of each phase encoding line (Moriguchi and Duerk, 2006), zigzag k-space trajectories are created. As shown by Breuer et al. (Breuer et al., 2008), the combination of zigzag sampling with parallel imaging significantly improves the reconstruction as the coil sensitivity variations in the readout direction is additionally utilized. For image reconstruction, they proposed a GRAPPA-type reconstruction.

Recently, the wave-CAIPI (Bilgic et al., 2015) method has been proposed for highly accelerated 3D imaging. Additional to 2D CAIPIRINHA sampling, sinusoidal G_{p1} and G_{p2} gradients are applied during the readout of each k-space line. The resulting corkscrew trajectories are well-suited for parallel imaging. The aliasing is spread to all three spatial dimensions and efficiently exploits the 3D coil sensitivity variations. Bilgic et al. showed that this method enables highly accelerated imaging and reduces artifacts and noise amplification compared to other methods. The authors unfold aliasing voxels using an iterative SENSE-type (Pruessmann et al., 1999) image reconstruction. To assess the feasibility of higher acceleration, acquisitions were also performed at 7T (Bilgic et al., 2015; Polak et al., 2018). Both, the increase in signal-to-noise ratio (SNR) from higher field strength and the improved coil sensitivity variation mitigate the inherent SNR penalty and the g-factor noise amplification. Over the last years, wave-CAIPI has been employed in different sequences such as conventional gradient-echo (GRE) (Bilgic et al., 2015), magnetization-prepared rapid gradient-echo (MP-RAGE) (Polak et al., 2018; Jolanda M. Schwarz, Eberhard D. Pracht, Brenner, et al., 2018), echo planar imaging (3D-EPI) (Poser et al., 2017), simultaneous multi-slice TSE (Gagoski et al., 2015) and 3D-TSE (Polak et al., 2019; Jolanda M. Schwarz, Eberhard D. Pracht, and Stöcker, 2018; Zhou et al., 2020).

GRAPPA (Griswold et al., 2002) is a well-established parallel imaging method for Cartesian acquisitions. While SENSE reconstructions are sensitive to small errors in the coil sensitivities, GRAPPA has been found to perform more robustly (Blaimer et al., 2004; Preibisch et al., 2008) and provides a more uniform noise distribution (Thunberg and Zetterberg, 2007). Uecker et al. (Uecker et al., 2014) explained the theoretical relationship between SENSE and GRAPPA and developed an improved iterative algorithm. As GRAPPA is a non-iterative, single step reconstruction, the aim of this project was to implement a GRAPPA-based reconstruction algorithm for wave-CAIPI acquisitions.

This chapter describes the GRAPPA-based wave-CAIPI reconstruction and validates the reconstruction method for highly accelerated T_1 weighted magnetization-prepared rapid gradient-echo (MP-RAGE) (Mugler and Brookeman, 1990) and T_2 weighted turbo spin echo (TSE) (Hennig et al., 1986; Mugler, 2014) acquisitions at 7T. The GRAPPA-based wave-CAIPI reconstruction method and the validation for the MP-RAGE sequence has been published as a Full Paper in the journal *Magnetic Resonance in Medicine* (Jolanda M. Schwarz, Eberhard D. Pracht, Brenner, et al., 2018).

3.2 Image Reconstruction

A GRAPPA-based wave-CAIPI algorithm was developed for the parallel imaging reconstruction. Compared to Cartesian GRAPPA described in Section 2.2.2.2, multiple GRAPPA reconstruction kernels along the readout direction (Breuer et al., 2008) are needed for the reconstruction of the wave-CAIPI dataset as schematically shown in Figure 3.1b). The required number of different GRAPPA reconstruction kernels depends on the number of k-space points acquired during one wave cycle. For example, for a matrix size of 512 in readout direction and 32 oscillations, $512/32 = 16$ reconstruction kernels are needed. The fully sampled k-space center or a low-resolution wave reference scan serves as autocalibration signal (ACS) for the determination of the GRAPPA weights. The different GRAPPA reconstruction kernels are slid through the ACS data and for each kernel, the kernel repetitions are collected in the source and the target matrix. The GRAPPA weights are derived from these matrices and are applied to the undersampled wave-CAIPI dataset.

After the GRAPPA reconstruction, the image still shows spreading in readout direction due to the non-Cartesian wave trajectory (cf. Figure 3.1a), right). The remaining wave spreading is removed by deconvolution with a point spread function (Bilgic et al., 2015)

$$\mathrm{PSF}(k_r, p_1, p_2) = \exp(i2\pi(\mathrm{T}_{p_1}(k_r)p_1 + \mathrm{T}_{p_2}(k_r)p_2)) \tag{3.1}$$

which depends on the spatial location in the phase and partition encoding directions p_1 and p_2, respectively. The sinusoidal k-space trajectories are described by T_{p_1} and T_{p_2}. The reconstructed wave-CAIPI image is then given by

$$\mathrm{Img}(r, p_1, p_2) = \mathcal{F}_r^{-1}[\mathrm{PSF}(k_r, p_1, p_2)\mathcal{F}_r[\mathrm{GR}(r, p_1, p_2)]], \tag{3.2}$$

where $\mathcal{F}_r$ is the discrete Fourier transform along the readout direction and GR is the GRAPPA reconstruction that still contains the wave spreading in readout direction.

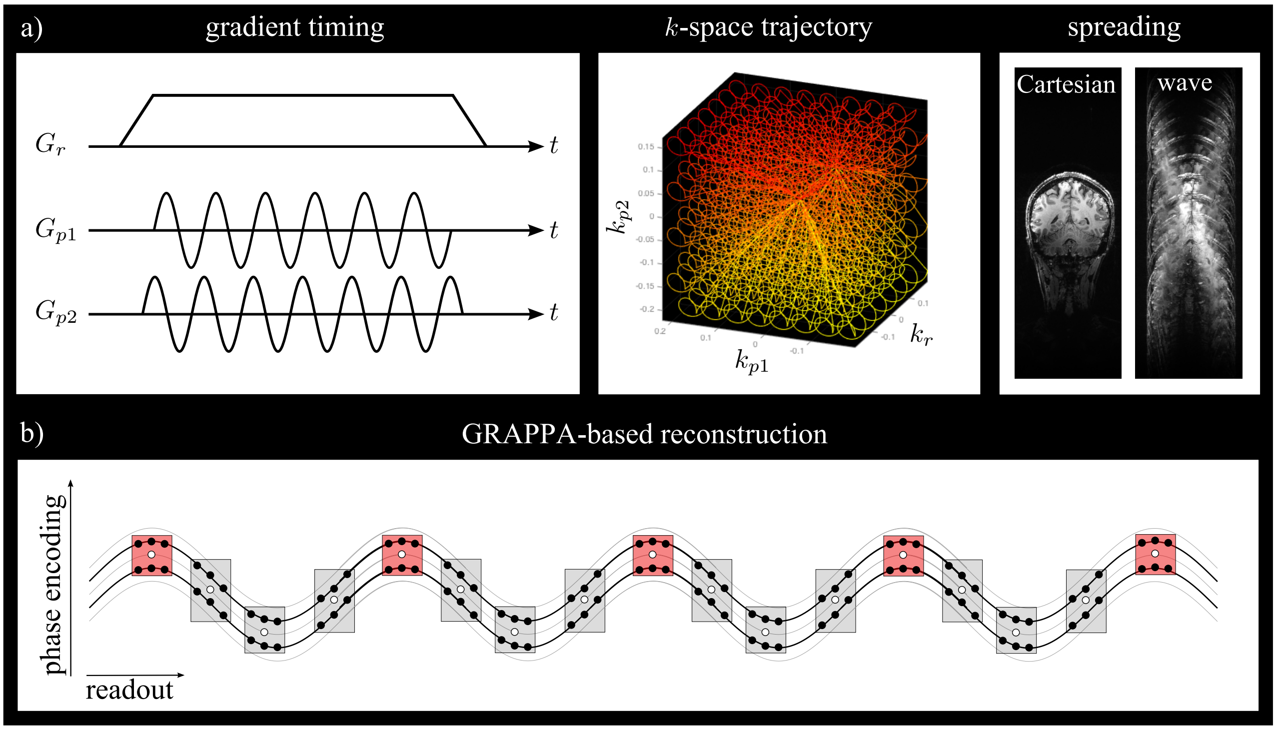

Figure 3.1: a) Schematic description of an acquisition with wave sampling. Sinusoidal phase encoding gradients during the readout process (left) result in corkscrew k-space trajectories (middle) and wave spreading in the readout direction of the image (right). b) For the GRAPPA-based wave-CAIPI reconstruction, multiple GRAPPA reconstruction kernels along the readout direction are required. The number of different kernels depends on the number of k-space points acquired during one wave cycle. For simplification, only a 2D k-space trajectory is schematically shown for an acceleration of $R = 2$ and for a 2D reconstruction kernel of size 2×3. The acquired source points (black points) from all coils are used to reconstruct a missing target point (white points) in a single coil. The repetition of one kernel along the readout is depicted in light red.

All image reconstructions were performed offline on a workstation with 256 GB of RAM and 2 CPUs with 12 cores each. The raw data was imported utilizing the ISMRM Raw Data Format (Inati et al., 2017) and reconstructed using our image reconstruction algorithm implemented in Python.

The different steps for our GRAPPA-based wave-CAIPI reconstruction are as follows:

1) raw data import using the ISMRM Raw Data Format.
2) incorporation of k-space trajectory measurements and determination of the PSF.
3) determination of GRAPPA weights from the ACS for each reconstruction kernel.
4) GRAPPA reconstruction of the missing k-space points.
5) replacement of the k-space center with ACS dataset (if ACS included).
6) deconvolution of the coil images with the PSF.
7) sum of squares combination of the deconvolved coil images.
8) removal of the oversampling in the readout direction.

The wave parameters, number of oscillations per readout and amplitude of the k-space trajectory, need to be chosen carefully for the GRAPPA reconstruction. Given a fixed number of samples along the corkscrew trajectory, the number of distinct GRAPPA kernels should be as small as possible. This results in a good fit of the GRAPPA weights since data from more kernel repetitions in readout direction are available. If the GRAPPA weights are computed based on too few kernel repetitions, the reconstruction shows significant GRAPPA artifacts. Therefore, increasing the number of wave cycles is desirable for GRAPPA-based wave-CAIPI reconstruction as it reduces the number of distinct points along the trajectory and, thus, the number of required kernels. The optimal number of wave cycles further depends on the wave amplitude, as both parameters determine the spread in readout direction. Finally, both parameters are limited by the performance of the gradient system. Based on these considerations, suitable wave parameterizations for each investigated sampling scheme are introduced in the next sections.

3.3 k-Space Trajectory Measurements

Due to gradient hardware imperfections, eddy currents, and field inhomogeneities, the applied gradient shape during a wave-CAIPI readout deviates from the nominal shape and induces phase errors, resulting in blurring and image artifacts. In order to measure the actual corkscrew k-space trajectory, a commercially available system for measuring the k-space trajectory (Clip-On Camera, Skope Magnetic Resonance Technologies, Zurich, Switzerland) was used. The camera consists of 16 ^{19}F NMR field probes ((De Zanche et al., 2008), cf. Section 2.10) which were placed around the head receive coil and were fixed on the coil using tape as exemplary shown in Figure 2.11a). The phase/partition encoding trajectories k_{p1} and k_{p2} were monitored during 10 readouts and averaged for noise reduction. Thus, no separate sequence implementation and calibration scans were required to measure the actual corkscrew trajectory. Based on this corkscrew trajectory, the point spread deconvolution function required for the wave-CAIPI image reconstruction was determined.

3.4 Wave-CAIPI MP-RAGE

3.4.1 Introduction

The magnetization-prepared rapid gradient-echo (MP-RAGE, (Mugler and Brookeman, 1990)) is the gold standard for T_1 weighted structural imaging. It is widely used for high-resolution anatomical imaging due to its good gray/white matter contrast. MP-RAGE images are utilized in various neuro applications, such as brain segmentation, co-registration, and voxel-based morphometry. However, the sequence suffers from long scan times due to a long inversion and recovery period before and after the gradient echo readout, respectively.

Wave-CAIPI sampling was incorporated in a fast 3D MP-RAGE sequence tailored for ultra-high field applications. To validate the proposed GRAPPA-based reconstruction method, fully acquired datasets (Cartesian and wave sampling) were retrospectively accelerated and compared to each other. Besides the investigation of the g-factor, subcortical segmentation was performed. The segmented structures were analyzed using the Dice coefficient. Compared to Cartesian GRAPPA, reconstruction artifacts and g-factor were significantly reduced, resulting in an improved image quality. Additionally, the reconstructed images were compared to those using the previously established SENSE-based wave-CAIPI reconstruction (Bilgic et al., 2015).

We performed whole brain imaging, 16-fold accelerated, at a resolution of $0.8\,\mathrm{mm}^3$ in an acquisition time of $52\,\mathrm{s}$.

3.4.2 Methods

3.4.2.1 Sequence Implementation

By combining corkscrew k-space trajectories with CAIPIRINHA sampling (Breuer et al., 2006), wave-CAIPI fully exploits the 3D coil sensitivity variations (see Figure 3.1a) and thereby reduces artifacts and limits reconstruction induced localized noise enhancement. For demonstration, we implemented a 3D MP-RAGE sequence with wave-CAIPI sampling on a 7T scanner (Siemens Healthineers, Erlangen, Germany) utilizing a 32-channel head coil (Nova Medical, Wilmington, USA) for data reception. The MR scanner is equipped with a gradient system allowing nominal maximum gradient amplitude of $40\,\mathrm{mT/m}$ and a maximum slew rate of $200\,\mathrm{T/m/s}$. The sequence is a fast 3D gradient echo sequence. Each repetition time interval TR starts with an inversion pulse followed by an inversion time TI to generate a T_1 weighted contrasts. The prepared magnetization is sampled using a train of gradient echoes. This block is repeated until the undersampled 3D k-space is filled. In order to speed up the acquisition of CAIPIRINHA-accelerated measurements, a flexible linear reordering scheme (Brenner et al., 2014; Busse et al., 2008) was employed. A similar reordering approach was recently introduced for wave-CAIPI MP-RAGE acquisitions by Polak et al. (Polak et al., 2018). Furthermore, all datasets in this work were acquired utilizing elliptical scanning (Bernstein et al., 2001; Brenner et al., 2014).

3.4.2.2 Validation - Retrospectively Accelerated Acquisitions

Fully sampled data with $1\,\mathrm{mm}$ isotropic resolution were acquired in 5 healthy subjects (two male, three female). The study protocol was approved by the local ethics committee, and subjects gave informed consent prior to undergoing MR examination.

For the MP-RAGE acquisitions, the following sequence parameters were used: FOV $= 256 \times 256 \times$

$176\,\mathrm{mm}^3$ (whole brain coverage with readout in head-foot direction), $TE = 4.6\,\mathrm{ms}$, $TR = 2.5\,\mathrm{s}$, $TI = 1.132\,\mathrm{s}$ and BW $= 130\,\mathrm{Hz/pixel}$. The acquisitions were repeated using different k-space trajectories:

1) Cartesian sampling
2) wave sampling with 32 oscillations/readout and wave amplitudes of $A = 1.5 \cdot \Delta k$ (in both phase encoding directions)
3) wave sampling with 32 oscillations/readout and $A = 2.5 \cdot \Delta k$

For the gradient system and the given sequence parameters, we chose 32 wave cycles per readout for the wave sampling. The maximum possible wave amplitude within the slew rate limit of the scanner was $A = 2.5 \cdot \Delta k$. The wave spreading pattern in readout direction [corkscrew k-space trajectories 2) and 3)] are shown in Figure 3.2.

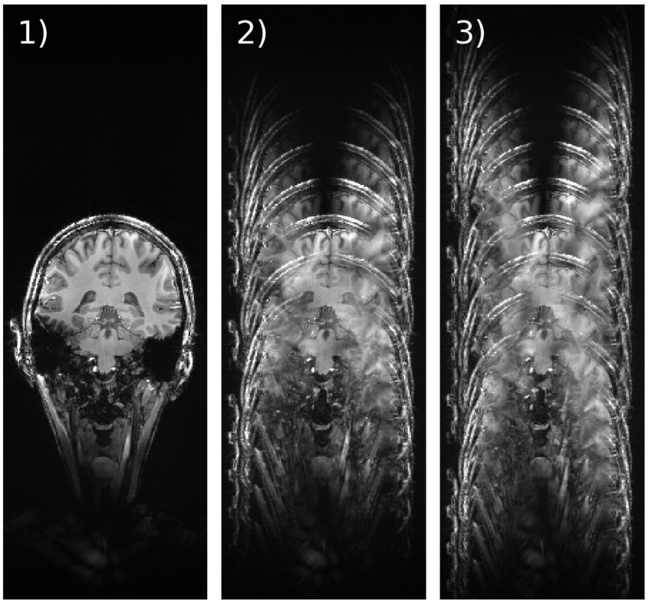

Figure 3.2: Coronal view (with oversampling in readout direction) of the fully encoded images for 1) Cartesian sampling, 2) wave sampling with 32 oscillations/readout and wave amplitudes of $A = 1.5 \cdot \Delta k$ and 3) wave sampling with 32 oscillations/readout and $A = 2.5 \cdot \Delta k$. The wave spreading in 3) better covers the FOV in the readout direction.

CAIPIRINHA-type (Breuer et al., 2006) accelerated data ($R = 3 \times 4$ with shift 2 and $R = 4 \times 4$ with shift 2) were simulated by retrospectively removing phase encoding steps from the fully sampled acquisitions. The k-space center of size $512 \times 32 \times 32$ served as ACS. We chose not to use a high bandwidth external calibration scan for all MP-RAGE acquisitions, as it would only allow acquisitions of significantly reduced number of wave cycles. As consequence, only a few kernel repetitions in readout direction would be used for the GRAPPA weight estimation. In addition, an integrated calibration scan can be included in the GRAPPA reconstruction and further improve image quality. The undersampled data were reconstructed using an in-house developed Python toolbox for image reconstruction. A 3D reconstruction kernel of size $3 \times 3 \times 3$ was taken and Tikhonov regularization was used for the calculation of the GRAPPA weights. For all measurements, the regularization was chosen as the identity matrix and scaled by the regularization factor $\lambda = 10^{-3} \cdot S_{\mathrm{max}}$, where S_{max} represents the maximum singular value of the GRAPPA source matrix of the ACS dataset. The regularization parameter was selected to achieve a good compromise between SNR and image artifacts. The ACS lines were included in the GRAPPA reconstruction resulting in an effective acceleration of $R_{\mathrm{eff}} = 9.6$ ($R = 3 \times 4$) and $R_{\mathrm{eff}} = 11.9$ ($R = 4 \times 4$).

After image reconstruction, the brain was extracted using BET (FSL (Smith, 2002)) for each of the subjects. The brain region as indicated in Figure 3.4 (top left) for one of the subjects served as region of interest (ROI) for the evaluation of the reconstruction results. The root mean square error (RMSE) with regard to the fully sampled data was calculated in the ROI. Additionally, g-factor maps were determined from 200 ‘pseudo multiple replicas’ (Robson et al., 2010) and the maximum and mean g-factor (g_{max} and g_{mean}) were evaluated in the ROI. The mean value and standard error of the RMSE, g_{max} and g_{mean} were determined across the five subjects.

In order to obtain a quantitative comparison of the different sampling schemes, the reconstructed images were automatically processed with the longitudinal Freesurfer stream (Reuter et al., 2012). For each of the volunteers, a subject template was created using the information of the three fully sampled images (Cartesian, $A = 1.5 \cdot \Delta k$, $A = 2.5 \cdot \Delta k$). This template served as initial guess for the processing of all 9 datasets (three different k-space trajectories, each of them acquired with acceleration factors $R = 1$, $R = 3 \times 4(2)$ and $R = 4 \times 4(2)$). The automatic subcortical segmentation (Fischl et al., 2002) of the fully sampled images served as ground truth. The relative segmentation volume overlap (Dice coefficient, cf. (Han and Fischl, 2007)) of the retrospectively accelerated images was evaluated with respect to the ground truth for different brain volumes. For each sampling scheme, the Dice coefficient was averaged across the five subjects and the standard error was calculated.

Additionally, the iterative SENSE-based reconstruction approach previously established by Bilgic et al. (Bilgic et al., 2015) was employed to the 16-fold retrospectively accelerated wave-CAIPI dataset with wave amplitude of $A = 2.5 \cdot \Delta k$ and 32 wave cycles. The coil sensitivities were computed using the ESPIRiT algorithm (Uecker et al., 2014) from the Berkeley Advanced Reconstruction Toolbox (BART) (Uecker et al.). For the SENSE-type wave-CAIPI reconstruction, the implementation offered as supplementary material by Bilgic et al. (Bilgic et al., 2015) was utilized.

Moreover, the impact of the actual measured k-space trajectory was investigated by comparing the GRAPPA reconstruction utilizing the nominal trajectory, a delay-corrected nominal trajectory, and the actual trajectory, respectively.

3.4.2.3 Accelerated Acquisitions

Additionally, $1\,\mathrm{mm}$ isotropic CAIPIRINHA-type accelerated measurements ($R = 3 \times 4(2)$ and $R = 4 \times 4(2)$) were performed. The total scan time reduction is based on the effective parallel imaging acceleration ($\mathrm{R_{eff}}$) and an additional $20\,\%$ scan time reduction is achieved through elliptical sampling (Brenner et al., 2014). The data were acquired for Cartesian k-space sampling and wave sampling (32 oscillations/readout and $A = 2.5 \cdot \Delta k$). The total scan time for the whole brain acquisitions were 48 seconds ($R = 12$) and 40 seconds ($R = 16$).

Furthermore, we acquired CAIPIRINHA and wave-CAIPI whole brain MP-RAGE images with $0.8\,\mathrm{mm}$ and $0.6\,\mathrm{mm}$ isotropic resolution employing $2 \times 2(1)$, $3 \times 4(2)$ and $4 \times 4(2)$ acceleration, respectively. Total acquisition times were 2:49, 1:07 and 0:52 minutes for the $0.8\,\mathrm{mm}^3$ resolution data and 4:48, 1:47 and 1:24 minutes for the scans with $0.6\,\mathrm{mm}$ isotropic resolution. Wave amplitudes were maximized within the slew rate limit of the scanner for the chosen number of oscillations.

An overview of the acquisition parameters of the accelerated MP-RAGE measurements is given in Table 3.1. 3D GRAPPA reconstruction kernels of size $3 \times 3 \times 3$ were utilized and the ACS lines were included in all reconstructions.

Table 3.1: Acquisition parameters of accelerated (wave-)CAIPI measurements

a) Sequence parameters

	Resolution $[\mathrm{mm}^3]$	FOV $[\mathrm{mm}^3]$	$TR/TE/TI$ [ms]	BW [Hz/px]
Protocol 1	$1.0 \times 1.0 \times 1.0$	$256 \times 256 \times 176$	2500/4.6/1132	130
Protocol 2	$0.8 \times 0.8 \times 0.8$	$256 \times 240 \times 166.4$	2500/5.0/1135	120
Protocol 3	$0.6 \times 0.6 \times 0.6$	$260 \times 234.7 \times 153.6$	2500/5.2/1106	120

b) Sampling schemes and acquisition times

	ACS	Amplitude $[\Delta k]$	Oscillations	Acceleration	Acq. Time [min]
Sampling 1	$512 \times 32 \times 32$	0.0/2.5	0/32	$3 \times 4(2)$	0 : 48
				$4 \times 4(2)$	0 : 40
Sampling 2	$640 \times 32 \times 32$	0.0/2.0	0/32	$2 \times 2(1)$	2 : 49
				$3 \times 4(2)$	1 : 07
				$4 \times 4(2)$	0 : 52
Sampling 3	$864 \times 32 \times 32$	0.0/2.5	0/27	$2 \times 2(1)$	4 : 48
				$3 \times 4(2)$	1 : 47
				$4 \times 4(2)$	1 : 24

3.4.3 Results

3.4.3.1 k-Space Trajectory Measurements

The necessity of a k-space trajectory measurement is illustrated in Figure 3.3. A section of the trajectory for a wave acquisition with $A = 2.5 \cdot \Delta k$ and 32 wave cycles during a $7680\,\mu\mathrm{s}$ readout is plotted for one of the phase encoding directions. The PSF was determined for the nominal and measured k-space trajectories and applied to the fully sampled wave measurement. Even if the deviation of the delay-corrected nominal trajectory to the measured trajectory is small, the nominal trajectory still produces significant artifacts in the image. Image reconstruction based on the measured trajectory provides strongly improved image quality, where the remaining small artifacts close to the ears stem from a tiny synchronization inaccuracy between the measured trajectory and the actual trajectory. This issue was solved in the newer software version of the field camera that was used for the wave-CAIPI TSE acquisitions in Section 3.5.

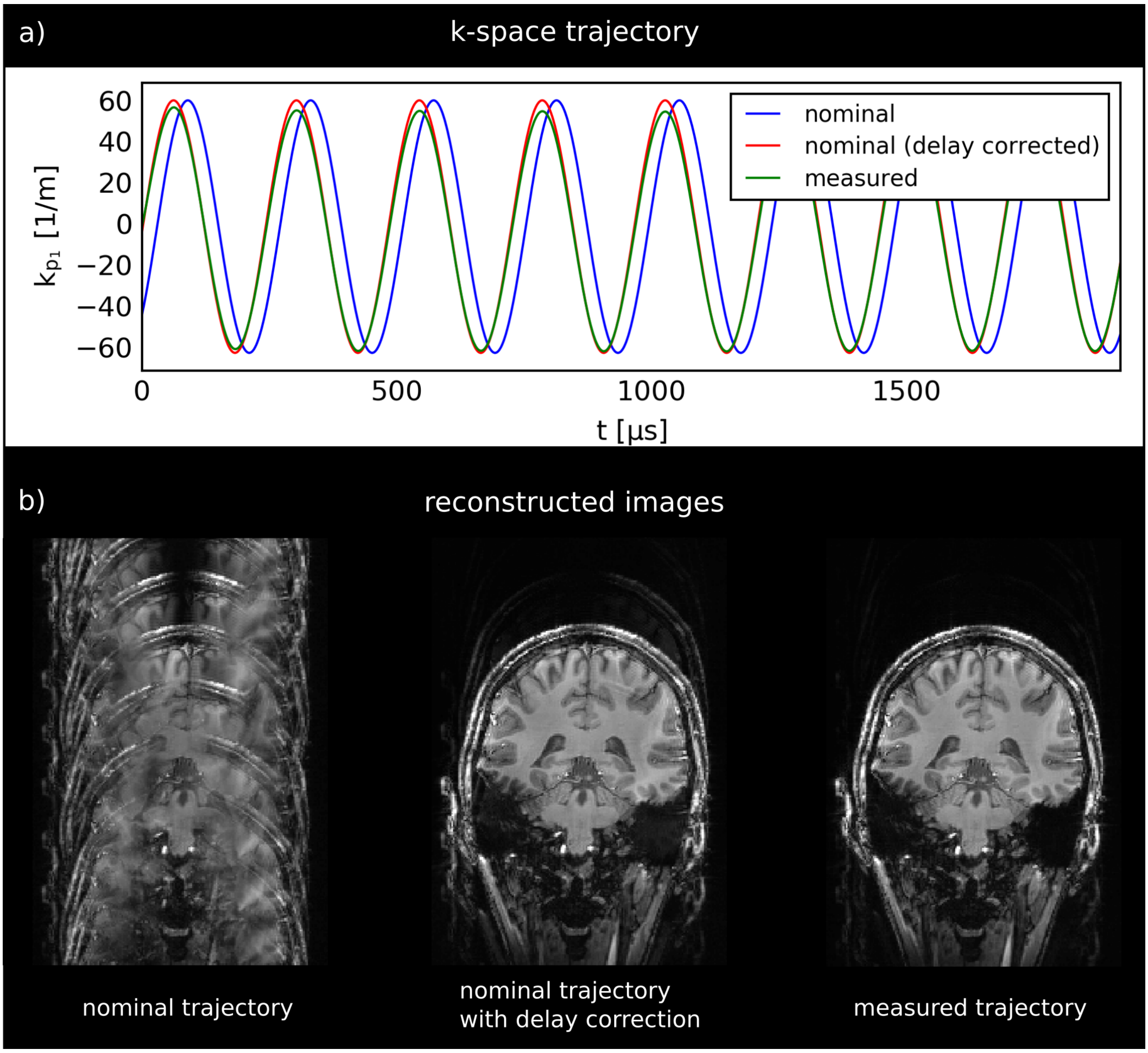

Figure 3.3: a) Section of the trajectory for a wave acquisition with $A = 2.5 \cdot \Delta k$ and 32 wave cycles during a $7680\,\mu$s readout for one of the phase encoding directions. The nominal, the delay-corrected nominal and the measured wave trajectory are plotted. b) Corresponding reconstruction of a fully sampled wave dataset. Without delay correction, the reconstruction using the nominal trajectory shows severe image artifacts. Also the delay-corrected nominal trajectory still produces significant artifacts.

3.4.3.2 Validation - Retrospectively Accelerated Acquisitions

In Figure 3.4, the reconstructed images for the simulated 16-fold accelerated CAIPIRINHA and wave-CAIPI acquisitions are shown for one subject. The noise amplification and reconstruction artifact level are quantified with g-factor maps and the difference to the fully sampled image. While aliasing artifacts are visible in the CAIPIRINHA images, the wave-CAIPI images are free of those. Further, the g-factor is reduced. All subsequently shown magnitude images were corrected for the receiver profile using the N4 bias correction (Tustison et al., 2010).

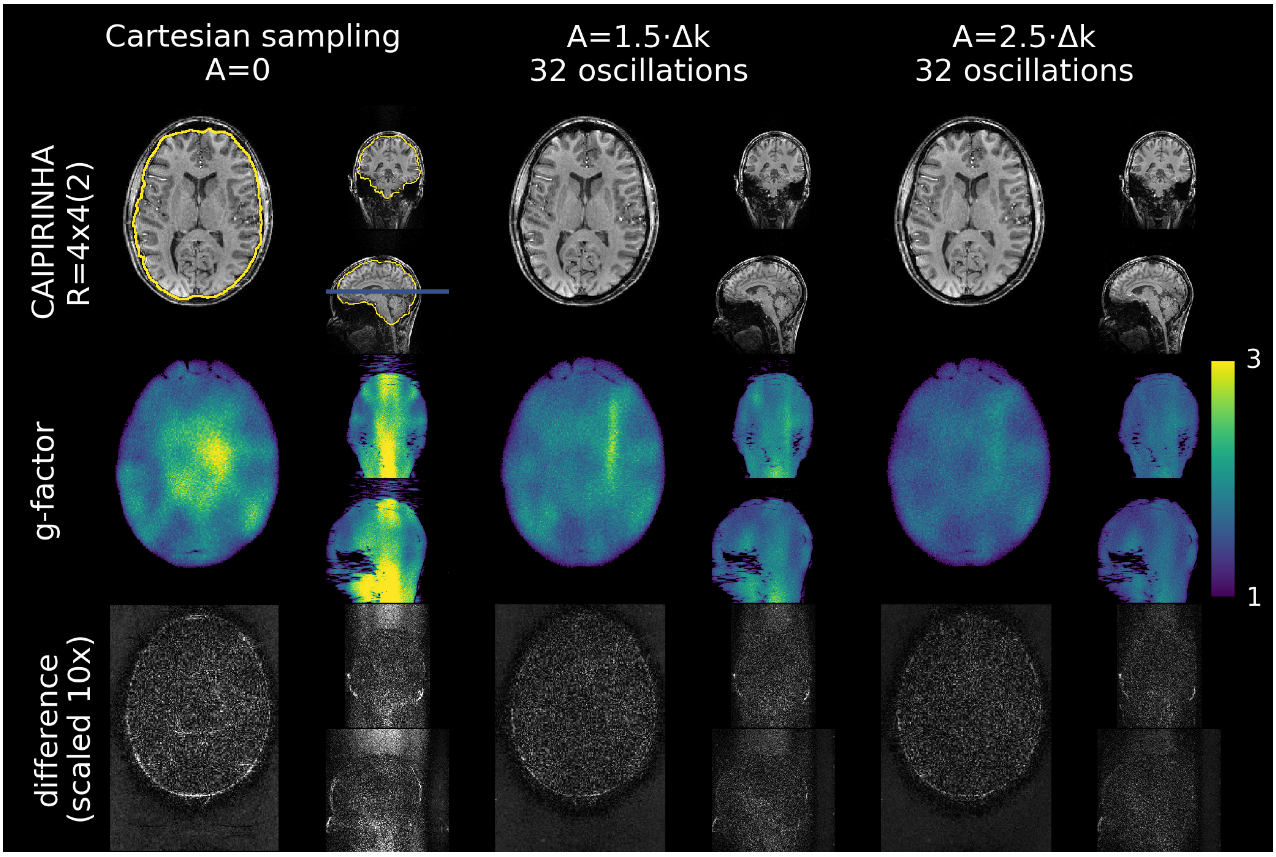

Figure 3.4: Retrospectively accelerated acquisitions. Top: 16-fold accelerated CAIPIRINHA and wave-CAIPI MP-RAGE images of one of the subjects. The position of the coronal slice is displayed by the vertical bar in the sagittal view. The yellow lines indicate the ROI used for the evaluation. Middle: g-Factor maps. Bottom: Difference to fully sampled image.

The reconstruction results are evaluated for 12- and 16-fold accelerated Cartesian CAIPIRINHA and wave-CAIPI across the five subjects. The mean values and standard error of the RMSE, g_{mean} and g_{max} are illustrated in Figure 3.5. For the higher wave amplitudes of $A = 2.5 \cdot \Delta k$, better results could be achieved than for amplitudes of $A = 1.5 \cdot \Delta k$ with the same number of oscillations. Wave-CAIPI with 32 oscillations and $A = 2.5 \cdot \Delta k$ clearly improves the RMSE and g-factor for both acceleration factors. Compared to 12-fold accelerated Cartesian CAIPIRINHA, 16-fold accelerated wave-CAIPI shows an improvement of $5.4\,\%$, $3.9\,\%$ and $3.7\,\%$ in RMSE, g_{max} and g_{mean}, despite the higher acceleration factor. In the wave-CAIPI acquisitions with amplitudes of $A = 1.5 \cdot \Delta k$, image pixels are badly folded which leads to a local hot spot of high g-factor. However, the mean g-factor is clearly reduced compared to the Cartesian reconstruction.

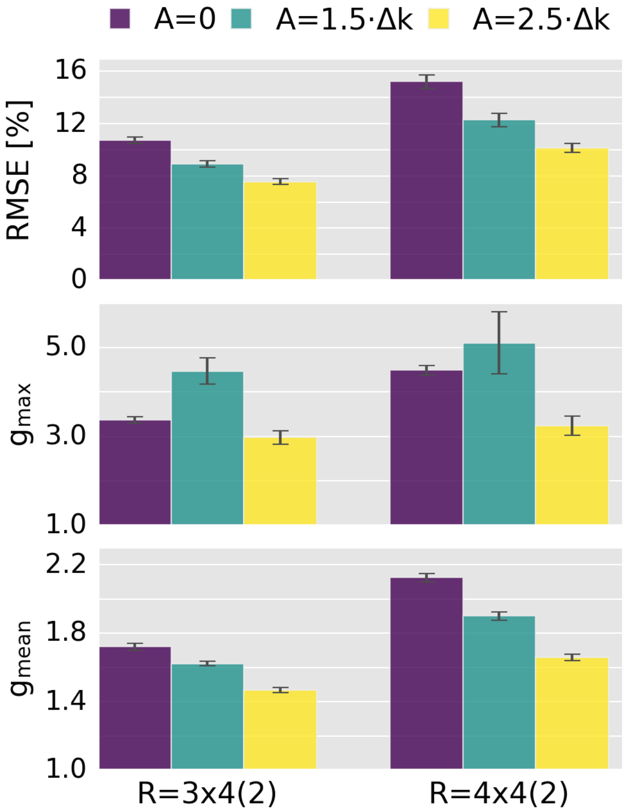

Figure 3.5: 12- and 16-fold accelerated Cartesian CAIPIRINHA (A = 0) and wave-CAIPI (wave amplitudes of $A = 1.5 \cdot \Delta k$ and $A = 2.5 \cdot \Delta k$) reconstructions evaluated in the brain ROI. The mean values of the five subjects and the standard error are illustrated via bar plots with error bars. The root mean square error (RMSE) and mean g-factor ($\mathrm{g}_{\mathrm{mean}}$) are clearly reduced for wave-CAIPI. For the higher wave amplitudes of $A = 2.5 \cdot \Delta k$, better results could be achieved than for amplitudes of $A = 1.5 \cdot \Delta k$ with the same number of oscillations.

For completeness, 16-fold accelerated wave-CAIPI reconstruction with included ACS and 12-fold accelerated Cartesian CAIPIRINHA with separate reference ACS are analyzed in Figure 3.6. The wave-CAIPI reconstruction performs clearly better than a time-matched Cartesian protocol with smaller ACS size and separate acquisition of ACS.

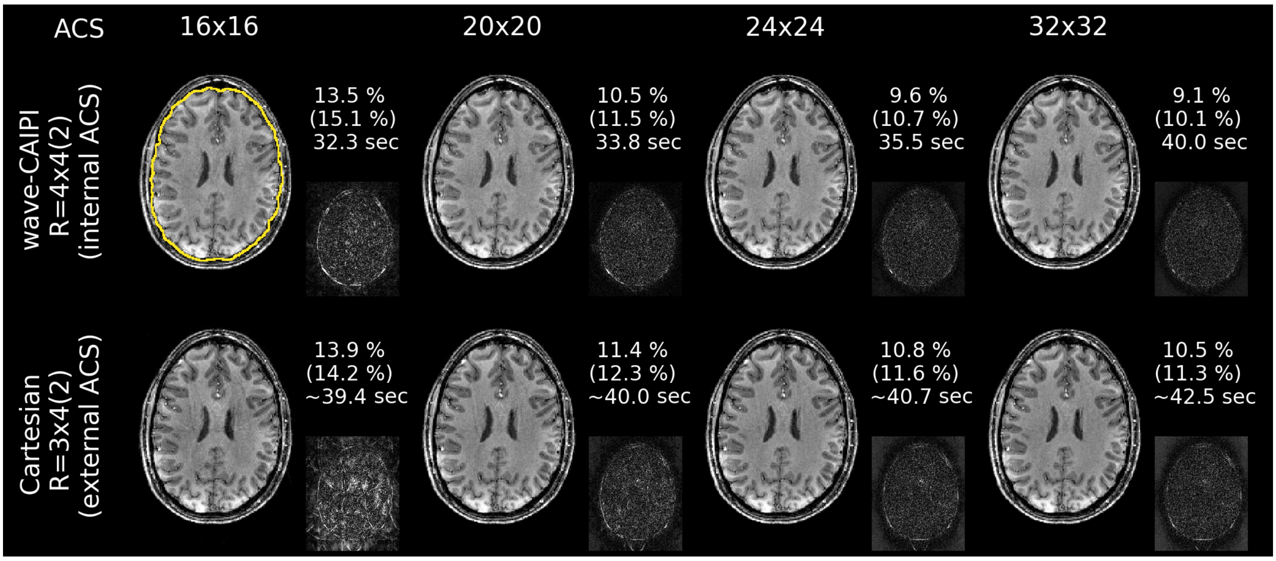

Figure 3.6: Comparison of 16-fold accelerated wave-CAIPI (ACS included) and 12-fold accelerated Cartesian CAIPIRINHA (ACS excluded). Accelerated data were simulated from the fully sampled datasets and the reconstruction was performed using 16×16, 20×20, 24×24 and 32×32 ACS lines for the computation of the GRAPPA weights. An axial view of the reconstruction and the difference to the fully sampled image (scaled $10\times$) are shown. The RMSE in the brain region and the acquisition time of a respectively accelerated scan are given. The RMSE averaged over all 5 subjects is depicted in brackets. The yellow line indicates the ROI used for the RMSE. The results show, that highly accelerated Cartesian CAIPIRINHA reconstructions are more prone to image artifacts, especially for smaller ACS sizes. 16-fold accelerated wave-CAIPI performs better than an approximately time-matched 12-fold accelerated Cartesian CAIPIRINHA protocol with 20×20 ACS lines and external reference scan. Additionally, wave-CAIPI allows a further scan time reduction by acquiring only 20×20 or 24×24 ACS lines while maintaining good image quality.

Figure 6.1 in the Appendix depicts examples of the subcortical segmentation results. Visual inspection shows that the segmentation worked well in all cases and no clear difference is visible between the different sampling schemes and accelerations. However, the quantitative comparison based on the Dice coefficient indicates a clear improvement of the segmentation of the different brain regions using wave-CAIPI instead of Cartesian CAIPIRINHA. For example, the dice coefficient of the hippocampus segmentation improved by $2.1\,\%$ ($91.2\,\%$ for CARTESIAN and $93.1\,\%$ for wave-CAIPI) for 12-fold acceleration and by $3.3\,\%$ ($91.2\,\%$ for CARTESIAN and 93.1% for wave-CAIPI) for 16-fold acceleration. The mean Dice coefficients across the five subjects with standard errors are shown in Figure 3.7. Here, left and right cerebral hemisphere values were combined since no significant lateralization effect was observed with respect to the Dice metric.

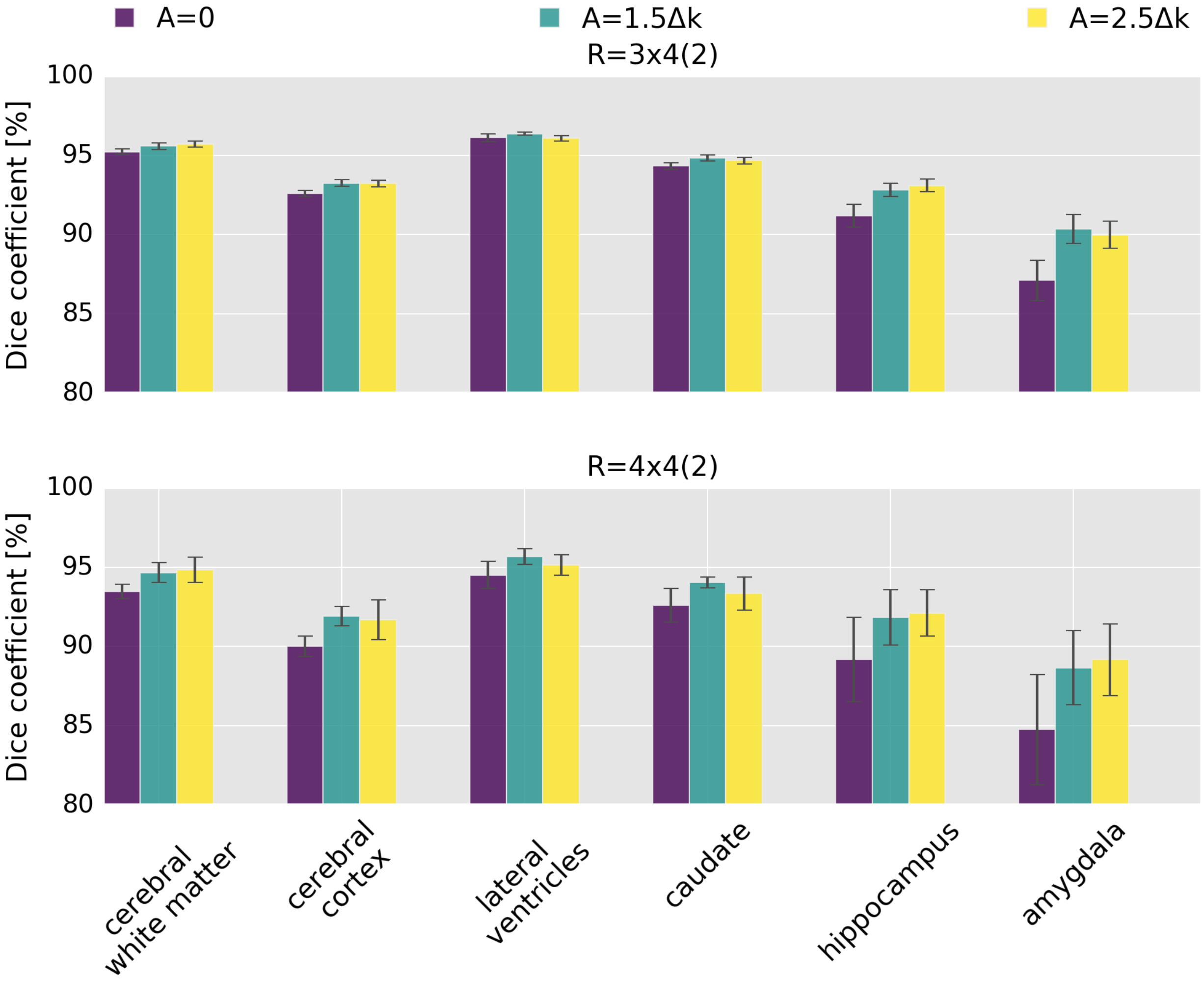

Figure 3.7: Dice coefficient (relative volume overlap) averaged across five subjects for different subcortical structures. The left and right cerebral hemispheres were combined as no discrepancy was found.

A comparison of the presented GRAPPA-based and the recently established iterative SENSE-type wave-CAIPI image reconstruction is illustrated in Figure 3.8. Both methods provide an effective wave-CAIPI reconstruction for 16-fold accelerated data with comparable image results. SENSE reconstruction requires high-quality sensitivity maps and mask region, estimated from the calibration data. Simple coil sensitivity estimates by means of conventional channel wise sum of squares division with subsequent masking resulted in strong artifacts of the SENSE reconstruction (not shown). However, utilizing the BART toolbox for coil sensitivity maps and mask region estimation, we were able to produce high-quality images with SENSE reconstruction. As the default mask computed by the toolbox was too small, we choose a smaller threshold for the mask estimation that optimized the RMSE of the reconstruction. Using this mask, the RMSE in the brain region was $9.58\,\%$ with regard to the fully sampled data. The SENSE reconstructions and the corresponding RMSE for smaller and larger mask sizes are shown for completeness in Figure 6.2 in the Appendix.

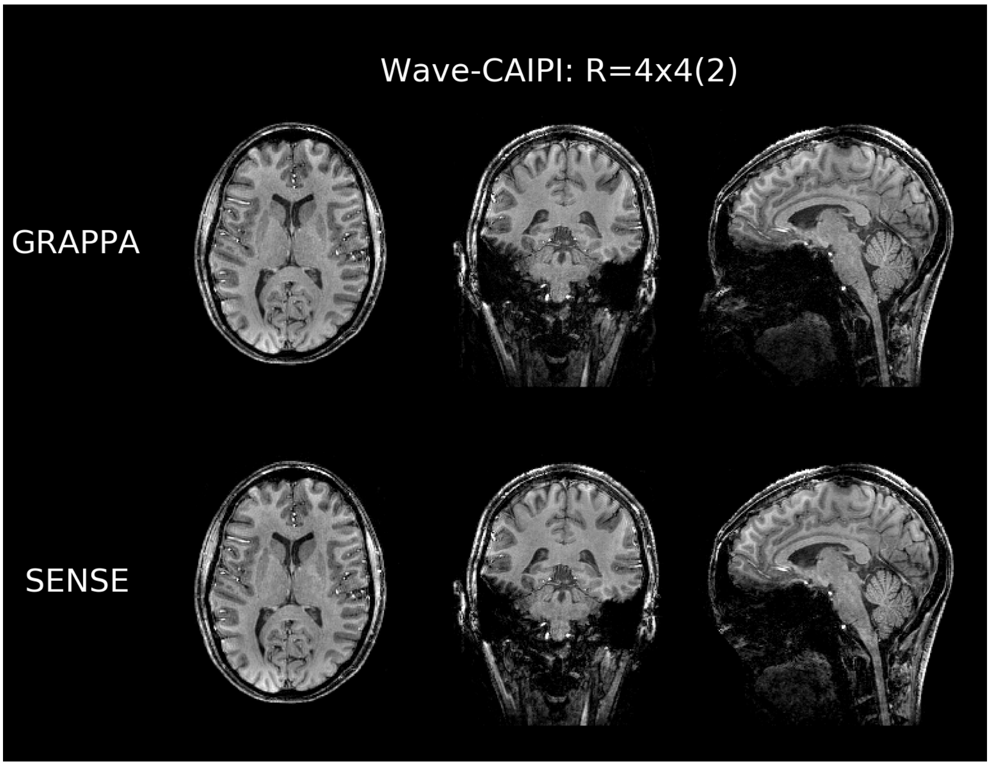

Figure 3.8: Retrospectively 16-fold accelerated wave-CAIPI acquisition reconstructed with a GRAPPA-based reconstruction (top) and a SENSE-type reconstruction (bottom).

3.4.3.3 Accelerated Acquisitions

Figure 3.9 depicts 12- and 16-fold accelerated full brain MP-RAGE images with $1\,\mathrm{mm}$ isotropic voxel size. As expected from the results of the retrospectively accelerated acquisitions, visual inspection shows similar image quality for conventional CAIPIRINHA and wave-CAIPI sampling, however, careful inspection shows a decreased noise level for the wave-CAIPI acquisitions. Furthermore, the axial slice of the 16-fold Cartesian CAIPIRINHA acquisition shows a reconstruction artifact which is not present for wave-CAIPI sampling. Inspecting the high-resolution acquisitions, the improved image quality of wave-CAIPI sampling becomes even more prominent. The corresponding images with $0.8\,\mathrm{mm}$ and $0.6\,\mathrm{mm}$ isotropic resolution and different acceleration factors are shown in Figure 3.10. For higher accelerations, a clear improvement in signal-to-noise ratio can be observed in the wave-CAIPI images.

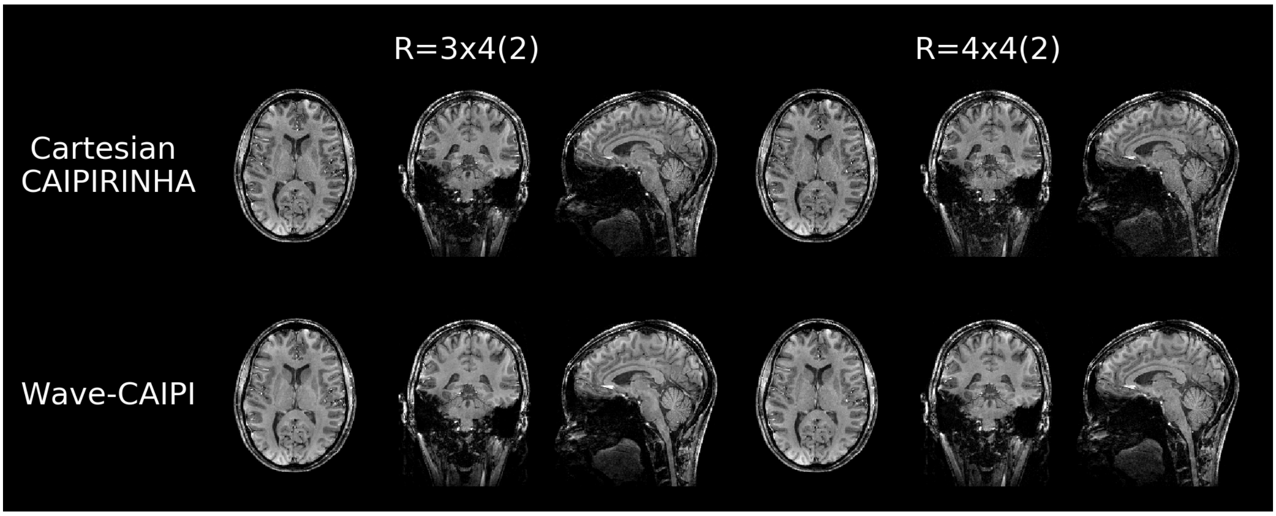

Figure 3.9: Retrospectively 16-fold accelerated wave-CAIPI acquisition reconstructed with a GRAPPA-based reconstruction (top) and a SENSE-type reconstruction (bottom).

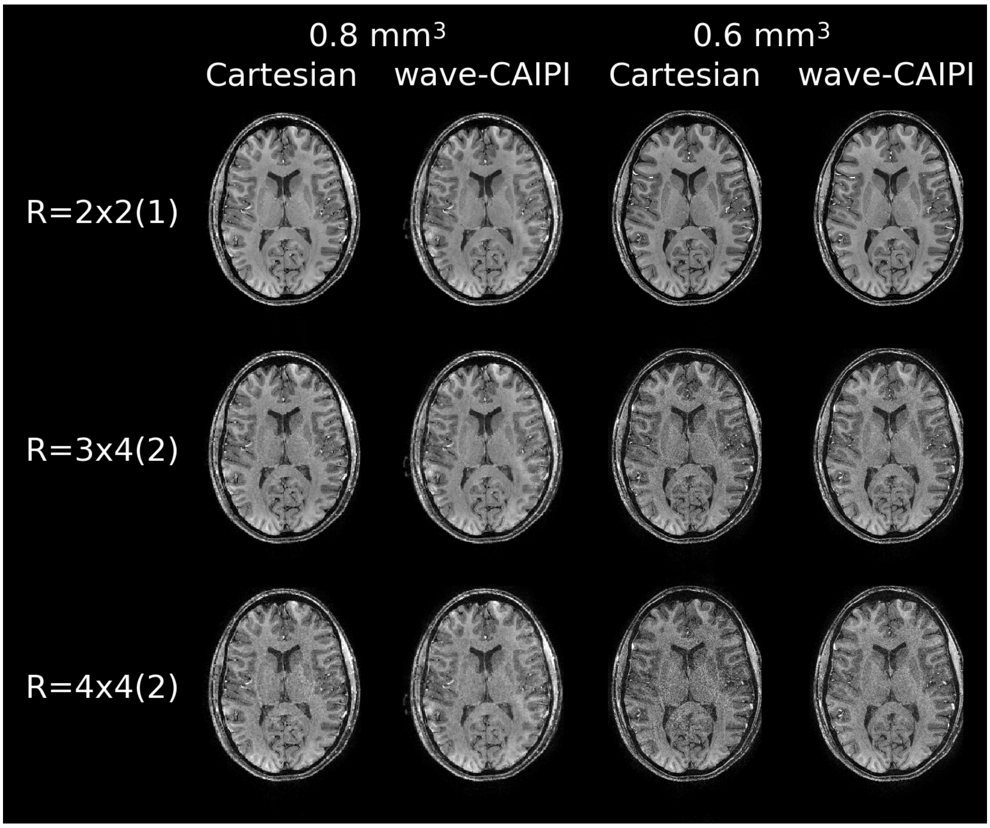

Figure 3.10: Axial view of Cartesian CAIPIRINHA and wave-CAIPI images with $0.6\,\mathrm{mm}$ and $0.8\,\mathrm{mm}$ isotropic voxel size. The data were acquired employing $2 \times 2(1)$, $3 \times 4(2)$ and $4 \times 4(2)$ acceleration, respectively. For higher accelerations, a clear improvement in signal-to-noise ratio can be observed in the wave-CAIPI images.

3.4.4 Discussion

We have shown that high-quality wave-CAIPI MP-RAGE images can be reconstructed by means of a GRAPPA-based algorithm utilizing multiple reconstruction kernels. Even for high acceleration factors, the non-iterative reconstruction is robust and does not depend on the accuracy of coil sensitivity estimations.

The GRAPPA-based wave-CAIPI reconstruction has been validated across five subjects at the 7 Tesla scanner. Full k-space MP-RAGE data with and without wave sampling were acquired and subsequent under-sampling was performed to simulate acceleration factors $R = 3 \times 4(2)$ and $R = 4 \times 4(2)$. Compared to Cartesian CAIPIRINHA sampling, the image reconstruction of wave-CAIPI MP-RAGE data strongly improved image quality with diminished artifacts and reduced g-factor penalties. It has been shown, that for the chosen parameters, the image quality of 16-fold accelerated wave-CAIPI is comparable to that of 12-fold accelerated Cartesian CAIPIRINHA (Figure 3.4). Utilizing the full k-space sampling as ground truth, an improvement in subcortical segmentation could be achieved for both accelerations using the wave-CAIPI sampling as compared to conventional Cartesian CAIPIRINHA sampling (Figure 3.7).

For the $1\,\mathrm{mm}^3$ resolution acquisitions, the k-space trajectory with 32 wave cycles per readout was found to be optimal. It allows sufficiently high wave amplitudes within the slew rate limit of the scanner and the GRAPPA weights are calculated based on 16 kernel positions in the readout direction. The spreading due to the higher wave amplitudes of $A = 2.5 \cdot \Delta k$ allows a full FOV coverage in readout direction with oversampling (cf. Figure 3.2) and better reconstruction results could be achieved than with the smaller wave amplitude of $A = 1.5 \cdot \Delta k$. The g-factor maps for 12- and 16-fold accelerated wave-CAIPI with $A = 1.5 \cdot \Delta k$ show high local values. In this case, the 3D aliasing does not seem to be optimal.

In order to improve the wave-CAIPI image quality, gradient waveforms (number of oscillations and wave amplitudes) must be optimized. As mentioned by Breuer et al. (Breuer et al., 2008) for zigzag sampling, a strategy to find the optimal gradient waveform is required. This strategy must take into account the sequence parameters, the gradient system, the acceleration factor/sampling pattern and the receiver coil. In contrast to the SENSE-based reconstruction, the quality of the GRAPPA-based wave-CAIPI reconstruction strongly depends on the number of wave cycles. To achieve a good fit of the GRAPPA weights, enough kernel repetitions in the readout direction must be available. We found that 32 wave cycles with maximum wave amplitude achieve a wave spreading which results in a good GRAPPA reconstruction.

We have shown that deviations between the nominal and actual corkscrew trajectory limit the performance of the reconstruction. Therefore, k-space trajectory measurements were performed once for each set of sequence parameters utilizing magnetic field probes, although other ways are possible to determine the actual wave-CAIPI trajectory (Bilgic et al., 2015; Cauley et al., 2016).

Accelerated wave-CAIPI MP-RAGE scans with $R = 4 \times 4(2)$ and whole-brain coverage were acquired in only 40 seconds. The GRAPPA-based wave-CAIPI reconstruction provided good image quality for highly accelerated, high-resolution measurements ($0.6\,\mathrm{mm}^3$ and $0.8\,\mathrm{mm}^3$ voxel size) and clearly outperforms conventional CAIPIRINHA sampling (Figure 3.10).

Nevertheless, we have shown that even for Cartesian CAIPIRINHA, the combination of our MP-RAGE implementation with flexible reordering and elliptical scanning and our GRAPPA reconstruction with 3D GRAPPA kernel, Tikhonov regularization and included ACS can achieve highly accelerated full brain acquisitions with good image quality.

Using our in-house developed Python implementation for image reconstruction on a high-end workstation, the total reconstruction time for the $1\,\mathrm{mm}^3$ wave-CAIPI MP-RAGE measurement with matrix size of $512 \times 256 \times 176$, ACS size of $512 \times 32 \times 32$, 32 wave cycles/readout and CAIPIRINHA-type acceleration of $R = 4 \times 4(2)$ was approximately 10 minutes. In contrast to conventional GRAPPA reconstructions, the oversampling in readout direction is only removed after the reconstruction. This extends the required memory and reconstruction time. However, there is still much potential to speed up the reconstruction. For example, the size of the dataset can efficiently be reduced prior to the reconstruction by applying coil array compression (Buehrer et al., 2007; Huang et al., 2008; Zhang et al., 2013). This technique reduces the processing time and computer memory requirements without a considerable degradation in image quality. If the main focus lies on the quality of the image, the virtual coil concept proposed by Blaimer et al. (Blaimer et al., 2009) improves the reconstruction conditions for the GRAPPA reconstruction and reduces the noise enhancement. Nevertheless, this concept doubles the number of channels and thereby increases the computation time. A combination of coil compression and the virtual coil concept might improve image quality without an increase or even with a reduction in reconstruction time.

3.5 Wave-CAIPI TSE

3.5.1 Introduction

In additional to the T_1 weighted MP-RAGE sequence of the previous section, wave-CAIPI sampling was incorporated in a turbo spin echo (TSE) sequence (Hennig et al., 1986; Mugler, 2014). TSE is also known as rapid acquisition with refocusing echoes (RARE) or fast spin echo (FSE), and provides an image contrast that is dominated by the transverse relaxation time T_2. It is widely used in clinical applications and neuroscience for T_2 weighted brain imaging, structural imaging and lesion detection. Compared to conventional spin echo sequences, multiple phase encoding lines are acquired during each repetition time (TR) interval of the TSE sequence. Nevertheless, the sequence suffers from long scan times due to the long TR and can thus benefit from the higher acceleration factors achievable with wave-CAIPI sampling.

To fulfill the CPMG condition despite eddy currents induced by the wave gradients, additional rephasing gradients were empirically determined using the field probe system. 16- and 20-fold accelerated wave-CAIPI TSE imaging at an isotropic resolution of $1\,\mathrm{mm}^3$ were performed and reconstructed using the GRAPPA-based parallel imaging reconstruction. Compared to Cartesian GRAPPA, reconstruction artifacts and g-factor were significantly reduced.

3.5.2 Methods

3.5.2.1 Sequence Implementation

Wave-encoding was incorporated in a 3D non-selective variable flip angle TSE sequence (Mugler, 2014; Pracht et al., 2018) as schematically shown in Figure 3.11.

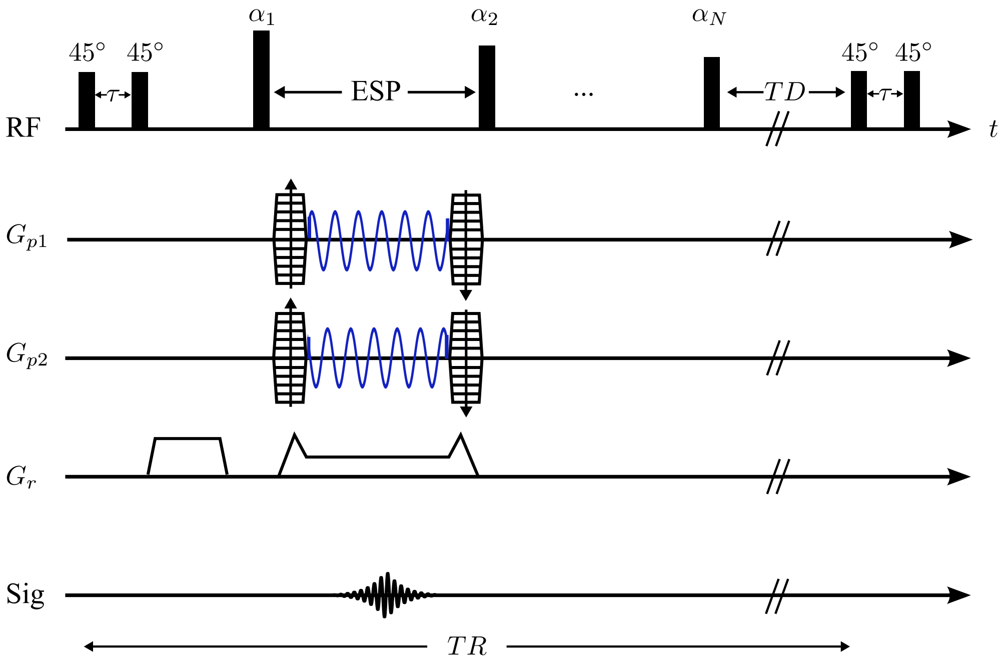

Figure 3.11: Schematic sequence diagram of the 3D wave-CAIPI TSE sequence with variable flip angles. The fat component is suppressed using a binomial water excitation pulse (Hore, 1983). The shortest possible echo spacing (ESP) is used for the echo train to avoid signal loss due to the T_2 decay. The refocusing angles α are calculated for a predefined signal shape. After a relaxation delay of TD, the next TR interval starts with the excitation pulses. The corkscrew k-space sampling is achieved by playing out sinusoidal gradients during each readout.

Compared to the conventional spin echo sequence introduced in Section 2.1.4.1, the TSE sequence uses a series of refocusing pulses to generates a train of echoes after each excitation pulse. Thereby, multiple phase encoding lines are acquired during each TR interval. The flip angles of the refocusing pulses are optimized using an extended phase graph (EPG) algorithm to achieve highest possible SNR at 7T for a predefined signal shape (Hennig, 1988; Hennig et al., 2004). To avoid signal loss and blurring due to the T_2 decay, the shortest possible echo spacing (ESP, time between consecutive echoes) is chosen. The fat signal is suppressed using a binomial water excitation pulse (Hore, 1983). The CAIPIRINHA-accelerated sequence is sped up using an improved linear reordering scheme (Feiweier, 2010) and elliptical scanning (Bernstein et al., 2001), where the corners of k-space are omitted. The corkscrew k-space sampling is achieved by playing out sinusoidal gradients in the phase encoding directions ($G_{p1/2}$) with a relative phase shift of $\pi/2$ during each readout (G_r). To reduce the ramp time, the sine and cosine gradients start with an initial phase of $\pi/4$.

3.5.2.2 CPMG Condition and Gradient Momentum Correction

Multiecho spin echo sequences, such as TSE sequences, rely on the CPMG (Carr-Purcell-Meiboom-Gill) condition (Meiboom and Gill, 1958) for generating long trains of spin echoes. They include a phase shift of $90°$ between excitation and refocusing pulses to reduce cumulated phase errors. The CPMG technique is robust and allows to destroy unwanted magnetization components rapidly after some echoes. Hence, echoes are generated at the same time after each refocusing pulse.

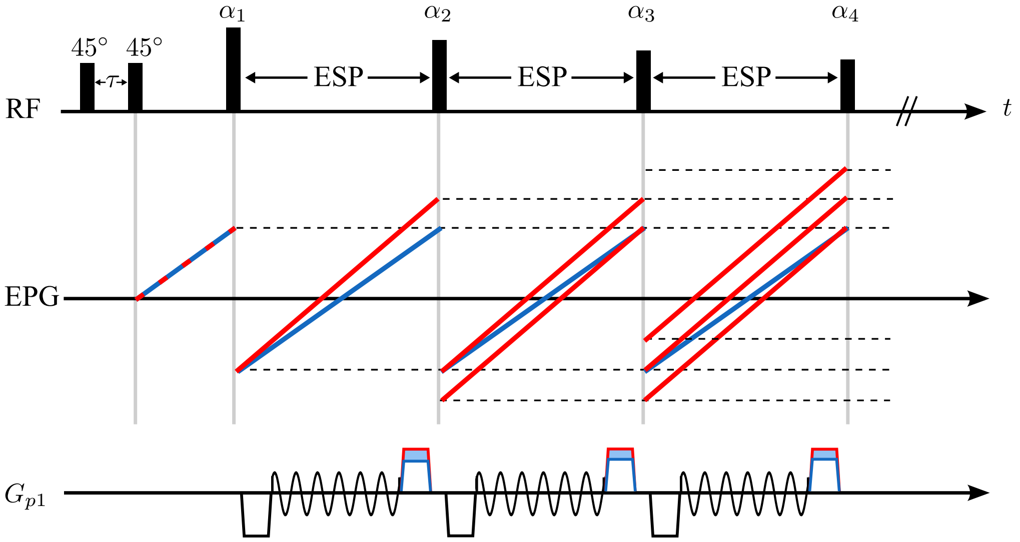

Figure 3.12: Schematic illustration of the extended phase graph (EPG) for the 3D wave-CAIPI TSE sequence with variable flip angles. Echoes are generated at the same time after each refocusing pulse (blue lines). The echoes correspond to the crossing of the blue lines with the time axis. An additional gradient momentum accumulated between refocusing pulses leads to the generation of spin echoes of increasing number with every refocusing pulse as indicated by the red lines. The phase encoding gradients G_{p1} between the refocusing pulses are exemplary depicted in the bottom line with the uncorrected rephasing gradient in red and the corrected gradient in blue. The gradient correction required for proper moment rephasing is colored in light blue.

The sinusoidal phase encoding gradients of the wave-CAIPI TSE sequence induce eddy currents which lead to an additional gradient momentum between consecutive refocusing pulses. The effect of this additional gradient momentum on the CPMG condition is illustrated in the extended phase graph in Figure 3.12. An increasing number of spin echoes is generated with every refocusing pulse. These unwanted echoes result in artifacts and signal dropouts in the reconstructed images.

The improper momentum rephasing between the refocusing pulses was solved empirically using the field probe system. During a phantom scan, the central k-space line was monitored and additional rephasing gradients were determined such that the k-space trajectory ends as expected in the k-space center after the gradient rephasing. By application of correction gradients, the CPMG condition is restored and one single spin echo is generated after each refocusing pulse.

3.5.2.3 Data Acquisition

All experiments were performed on a MAGNETOM 7T scanner (Siemens Healthineers, Erlangen, Germany) utilizing a 32-channel head coil (Nova Medical, Wilmington, USA). The data were acquired in a healthy volunteer using the following sequence parameters: FOV$= 256 \times 240 \times 176\,\mathrm{mm}^3$ (whole brain coverage with readout in head-foot direction), $1\,\mathrm{mm}^3$ resolution, $TR = 5\,\mathrm{s}$, number of refocusing pulses $N = 150$ and BW$= 300\,\mathrm{Hz/pixel}$. CAIPIRINHA-type accelerated measurements ($R = 4 \times 4$ with shift 2 and $R = 5 \times 4$ with shift 2) were performed for Cartesian k-space sampling and for wave sampling. For wave sampling, 16 oscillations per readout and wave amplitudes of $A_{p1} = 3 \cdot \Delta k_{p1}$ and $A_{p2} = 2 \cdot \Delta k_{p2}$ in the phase encoding directions were chosen within the slew rate limits of the scanner. An oversampling factor of 4 was chosen in readout direction for all acquisitions to avoid remaining wave artifacts in the reconstructed images (Wang et al., 2020). Additionally, a reference scan with 32×32 fully sampled central Cartesian or wave-sampled calibration lines was acquired. The total acquisition time was 1:32 minutes for the 16-fold accelerated and 1:17 minutes for the 20-fold accelerated measurement.

Trajectory measurements were performed simultaneously to the imaging experiment using the field camera. Due to the newer software version, delays between the MR scanner and the field probe system were considered by short synchronization scans at the beginning of the actual imaging experiment (cf. Section 2.10) for all wave-CAIPI TSE measurements.

The additional rephasing gradients required for a correct gradient rephasing were determined empirically as described above during a phantom measurement using the same sequence parameters as for the planned in-vivo measurement. The adjusted rephasing gradients were then used for the actual measurement.

3.5.2.4 Image Reconstruction and Data Analysis

For image reconstruction, a 3D GRAPPA reconstruction kernel of size $3 \times 3 \times 3$ was chosen and Tikhonov regularization was used for the calculation of the GRAPPA weights to achieve a good compromise between signal-to-noise ration (SNR) and image artifacts.

G-factor maps were calculated from 100 ‘pseudo multiple replicas’ (Robson et al., 2010) and the maximum and mean g-factor were evaluated over the whole brain extracted using BET (FSL (Smith, 2002)). All shown magnitude images were corrected for the receiver profile using the N4 bias field correction (Tustison et al., 2010).

3.5.3 Results

The empirical determination of the additional rephasing gradients is depicted in Figure 3.13. Figure 3.13a) shows the monitored sinusoidal gradient waveforms and the corresponding k-space trajectory of the central k-space line for the acquisition without any correction. It is obvious, that the k-space trajectory does not end in the k-space center as expected after the gradient rephasing. However, the application of adjusted rephasing gradients led to the expected trajectory of the central k-space line (cf. Figure 3.13c)).

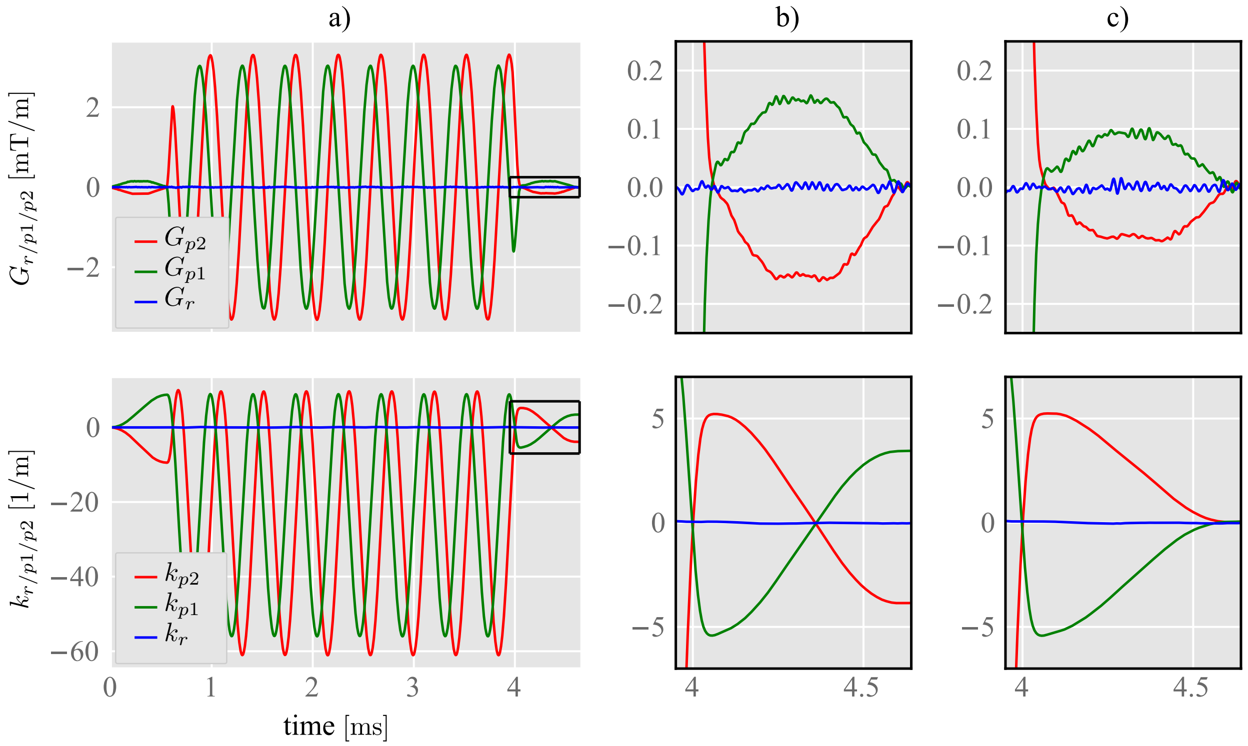

Figure 3.13: Wave-encoded gradient waveforms and k-space trajectories for the central k-space line. a) The wave gradients induce an additional gradient moment resulting in a k-space trajectory which is not rephased in the k-space center. b) Enlarged view of the improper gradient rephasing of a) indicated by the black box. c) Corrected rephasing moment after application of additional rephasing gradients.

Improper gradient momentum dephasing: The wave-CAIPI TSE images show residual inhomogeneities and signal dropouts as indicated by the red arrows in Figure 3.14a). These artifacts vanish in Figure 3.14b), where the empirically determined additional rephasing gradients were applied.

a) improper gradient momentum dephasing

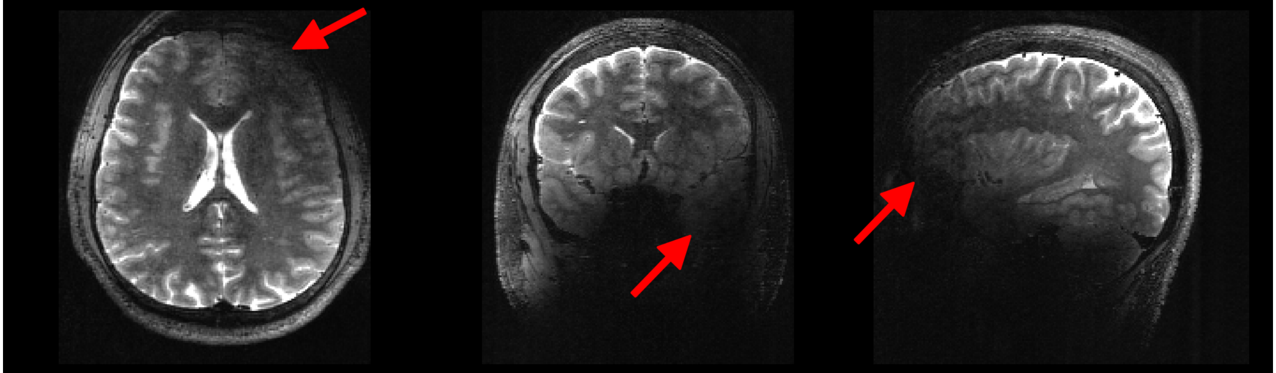

b) corrected gradient momentum dephasing

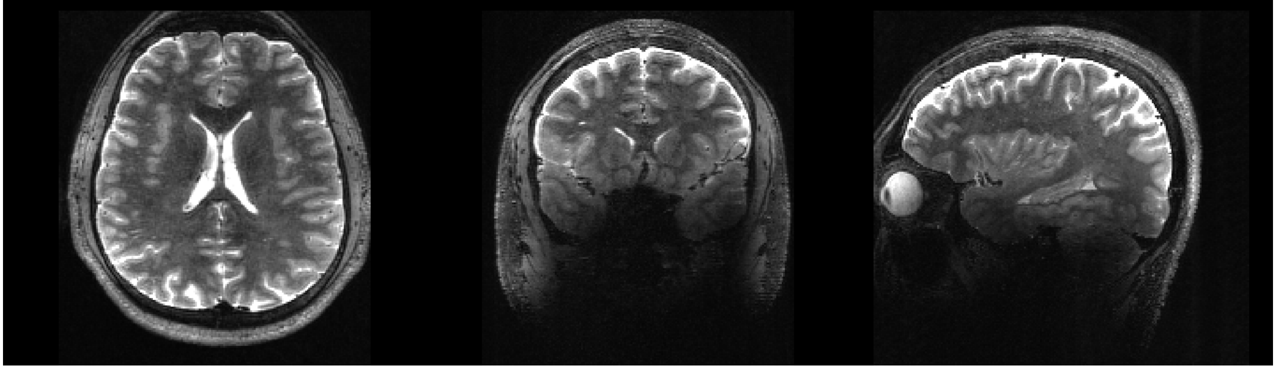

Figure 3.14: Reconstructed images of wave-CAIPI acquisitions with a) improper gradient momentum rephasing and b) corrected momentum rephasing by application of an additional empirically found rephasing gradient. The red arrows indicate residual inhomogeneities in the reconstructed images which vanish with proper momentum rephasing.

The reconstructed images and g-factor maps of 16-fold accelerated CAIPIRINHA and wave-CAIPI TSE acquisitions are shown in Figure 3.15. The gradient momentum of the wave-CAIPI acquisition was empirically corrected as described above. The wave-CAIPI TSE images show a clear improvement in image quality with less reconstruction artifacts and reduced noise enhancement. The mean g-factor is reduced by $31\,\%$ and the maximum g-factor by $42\,\%$.

Figure 3.16 shows example slices of the 20-fold accelerated 3D TSE acquisitions. Due to the high acceleration, the Cartesian images show strong parallel imaging artifacts indicated by the red arrows. These artifacts are clearly reduced in the wave-CAIPI images.

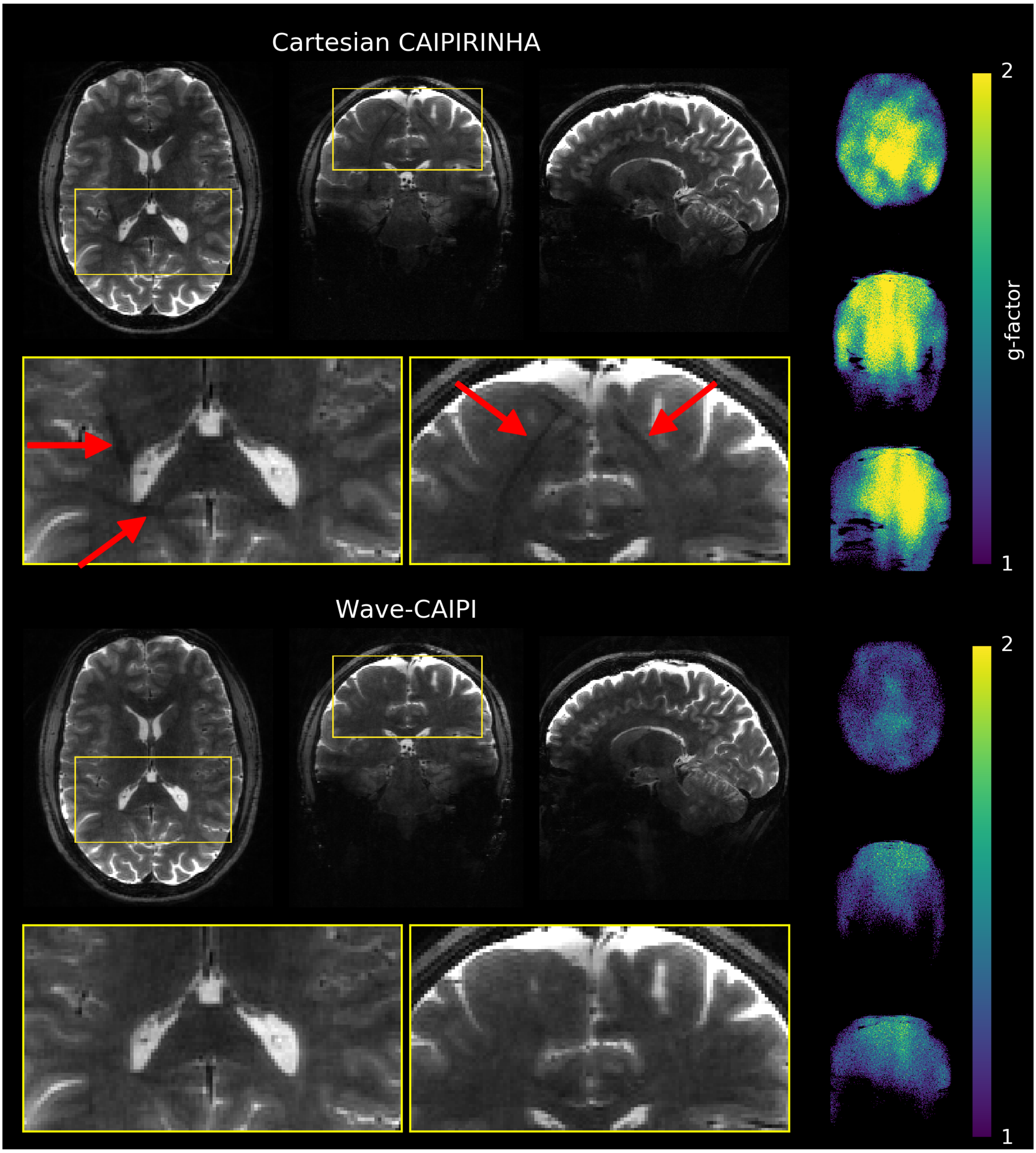

Figure 3.15: Reconstructed images and g-factor maps of 16-fold accelerated full brain CAIPIRINHA and wave-CAIPI TSE acquisitions. Image quality is improved in the wave-CAIPI acquisition with diminished artifacts and strongly reduced g-factor penalties. The red arrows indicate aliasing artifacts in the 2D CAIPIRINHA images. They are not visible in the wave-CAIPI images.

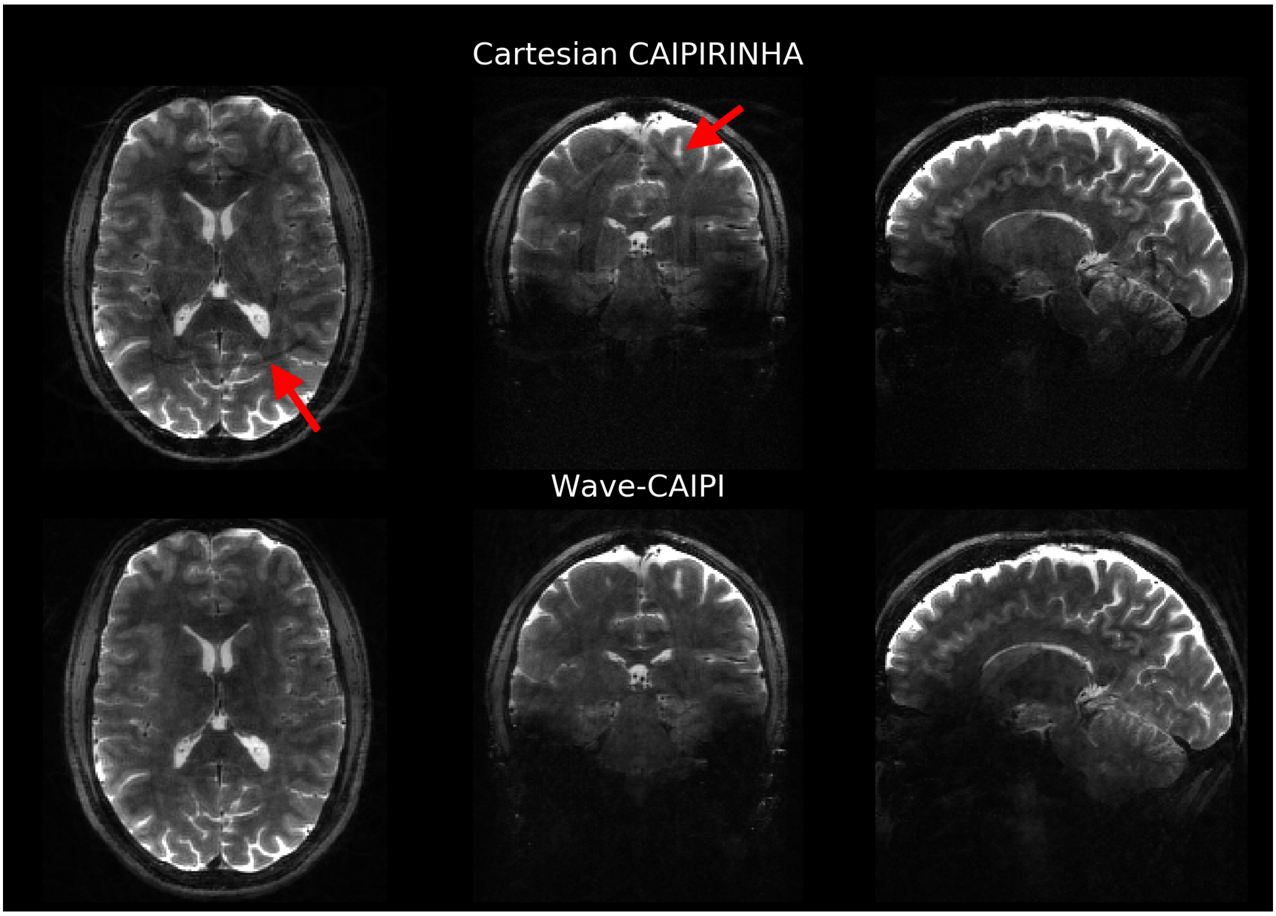

Figure 3.16: Axial, coronal and sagittal example slices of 20-fold accelerated full brain CAIPIRINHA and wave-CAIPI TSE acquisitions. Image artifacts are clearly reduced in the wave-CAIPI images as indicated by the red arrows.

3.5.4 Discussion

The application of sinusoidal phase encoding gradients in addition to CAIPIRINHA-type acceleration enabled highly accelerated TSE imaging at a high spatial resolution of $(1\,\mathrm{mm})^3$. Compared to the Cartesian CAIPIRINHA accelerated images, the wave-CAIPI images showed less image artifacts and significantly reduced noise enhancement (cf. Figure 3.15 and 3.16).

The GRAPPA-based wave-CAIPI reconstruction performs best for a large number of wave cycles and thus many kernel repetitions in readout direction (cf. Figure 3.1b)). This allows a robust determination of the GRAPPA weights. However, the required number of wave cycles and the slew rate limit of the scanner constraints the choice of possible wave parameters for the wave-CAIPI TSE acquisition. The maximum benefit of wave-CAIPI acquisitions can generally be achieved for sequences with low readout bandwidth (Wang et al., 2020), such as the MP-RAGE sequence. This allows relatively high wave amplitudes at a sufficient large number of wave cycles within the slew

rate limit of the scanner and increases the wave spreading.
An increase of the readout bandwidth by a factor of 2 leads to a reduction of the maximum achievable wave amplitude by a factor of 4 or to a reduction of the maximum number of wave cycles by a factor of 2 and thus significantly reduces the wave spreading along the readout direction. Compared to the proposed GRAPPA-based reconstruction, a SENSE-type reconstruction (Bilgic et al., 2015; Pruessmann et al., 1999) does not require a maximum number of wave cycles. However, Wang et al. (Wang et al., 2020) observed, that large wave amplitudes lead to obvious reconstruction artifacts in SENSE-based reconstructions, even if the noise enhancement is reduced.

It has been shown, that wave-CAIPI sampling increases the SNR for the TSE sequence parameters chosen in this section and thus allows for higher acceleration factors than 2D CAIPIRINHA acquisitions. However, wave-encoding is only suitable for TSE applications with relatively low readout bandwidth that allow large wave spreading.
The SNR of fast TSE acquisitions is influenced by various sequence parameters, and the choice of those is not straightforward. On the one hand, higher readout bandwidth result in a shorter echo train with reduced signal decay. Due to the generally higher SNR, these acquisitions allow higher parallel imaging acceleration, or alternatively more refocusing pulses can be applied after each excitation to reduce the total scan time. These acquisitions do not further benefit from wave-CAIPI sampling. On the other hand, SNR is proportional to the square root of the readout bandwidth (cf. Section 2.1.6) and the SNR can benefit from lower readout bandwidth. These TSE acquisitions take advantage of the improved SNR or higher acceleration factors achieved with wave-CAIPI sampling.

Eddy currents induced by the sinusoidal phase encoding gradients in the TSE sequence cause an additional gradient moment between consecutive refocusing pulses and lead to image artifacts. The proposed method using NMR field probes for k-space trajectory measurements allows to measure this additional momentum and to determine the correction gradients in order to avoid these artifacts. However, the method is empirical and the additional magnetic gradient must be determined for every protocol, as the induced eddy currents depend on the imaging gradients and the timing of the sequence. Zhou at al. (Zhou et al., 2020) used a first-order eddy current model to determine additional prephasing and rephasing gradients to maintain the CPMG condition for the wave-encoded TSE pulse train. The response of the gradient system to a predefined input is characterized by the so-called gradient impulse function (GIRF) (Signe J. Vannesjo, Maximilan Haeberlin, et al., 2013). This methods allows to calculate correction gradients for different protocols and must be investigated in further studies.

3.6 Conclusion

In this chapter, a GRAPPA alternative for wave-CAIPI reconstructions is presented. GRAPPA is a robust reconstruction method which is well-established for Cartesian acquisitions. By the use of multiple 3D reconstruction kernels and a PSF deconvolution, the wave-CAIPI reconstruction can be formulated as a Cartesian problem and allows an efficient GRAPPA-based image reconstruction. The corkscrew k-space trajectory required for the PSF deconvolution is measured using 16 magnetic field probes.

Wave sampling was incorporated in two 3D sequences optimized for 7T applications: a magnetization-prepared rapid gradient-echo (MP-RAGE) sequence and turbo spin echo (TSE) sequence.
The combination of the wave-CAIPI MP-RAGE implementation with flexible reordering and elliptical scanning and the GRAPPA-based wave-CAIPI reconstruction enables ultra-fast high-resolution MP-RAGE imaging at 7T. 16-fold accelerated full brain MP-RAGE scans with $1\,\mathrm{mm}$ and $0.8\,\mathrm{mm}$ isotropic resolution are acquired in only 40 seconds and 52 seconds, respectively. Compared to Cartesian CAIPIRINHA, the GRAPPA-based image reconstruction of wave-CAIPI MP-RAGE data achieves strongly improved image quality with fewer artifacts, reduced g-factor penalties, and better subcortical segmentation. The reconstruction results are validated across five subjects.
Similarly, the GRAPPA reconstructed wave-CAIPI TSE achieves an improved image quality with reduced noise enhancement for 16- and 20-fold accelerated imaging experiments. Due to the sinusoidal phase encoding gradients, an additional magnetic gradient momentum is induced between consecutive refocusing pulses of the spin echo sequence. The correcting rephasing gradients are determined empirically with k-space trajectory measurements using the field probe system. Image artifacts caused by improper momentum rephasing can thus be successfully prevented.

4

Correction of Physiological Noise in 3D-EPI Acquisitions

This chapter was partly adapted from:

Schwarz JM, Stirnberg R, Ehses P and Stöcker T, 2019. Correction of physiological field fluctuations in high- and low-resolution 3D-EPI acquisitions at 7 Tesla. Proceedings of the 27th Scientific Meeting of the International Society for Magnetic Resonance in Medicine, p. 0446.

Brunheim S, Mirkes C, Dietrich B, Schwarz JM, Stirnberg R, Ismar S, Alexander C, Barmet C and Stöcker T, 2020. Replaceable field probe holder for the Nova coil on a 7 Tesla Siemens scanner. Proceedings of the 28th Scientific Meeting of the International Society for Magnetic Resonance in Medicine.

4.1 Introduction

3D echo planar imaging (3D-EPI) (Poser et al., 2010) is utilized for an increasing number of applications such as functional MRI (fMRI), T_2^* weighted imaging, quantitative susceptibility mapping (QSM) or T_2^* mapping (Langkammer et al., 2015; Poser et al., 2010; Stirnberg et al., 2018, 2017; Stirnberg and Stöcker, 2014; Van Der Zwaag et al., 2012; Zwanenburg et al., 2011). 3D-EPI enables fast whole-brain coverage with high spatial resolution and increased signal-to-noise ratio (SNR) compared to conventional 2D-EPI. Especially at ultra-high fields, 2D-EPI acquisitions rapidly reach the specific absorption rate (SAR) safety limits. Due to shorter repetition times, 3D-EPI allows the use of much smaller flip angles and hence reduce the local energy deposition. However, the main drawback of 3D-EPI acquisitions is that they are more affected by physiological noise as caused by breathing, cardiac pulsation or movement of the subject during the measurement (Van Der Zwaag et al., 2012).

Gradient-echo sequences at long echo times (TE) in general suffer from physiologically induced field perturbations (Hu and Kim, 1994; Raj et al., 2000; Van de Moortele et al., 2002; Versluis et al., 2010). It has been shown that the influence of physiological field fluctuations on image quality is higher for sequences, where the volume is acquired in several shots, such as segmented 3D-EPI (Van Der Zwaag et al., 2012). Van der Zwaag et al. showed that the temporal signal-to-noise ratio (tSNR) decreases with increasing number of segments and that the maximum available tSNR is reduced compared to acquisitions in a single shot. Subject motion changes the magnetic susceptibility distribution and gives rise to dynamic field fluctuations in the magnetic bore. The resulting field fluctuations affect spatial encoding even at some distance from the moving object and give rise to image artifacts. The effect of physiological field changes scales with signal amplitude and is therefore more prominent at higher field strengths, such as 7 Tesla.

An application, which benefits from the short acquisition time with 3D-EPI, is T_2^* weighted imaging (Zwanenburg et al., 2011). T_2^* weighted imaging is sensitive to susceptibility changes and forms the basic of many MR applications such as the depiction of iron deposition, hemorrhage or calcification in tissues and lesions (Chavhan et al., 2009; Versluis et al., 2010). However, to generate a sufficient T_2^* contrast, T_2^* weighted imaging requires relatively long TE which make the acquisition sensitive to physiological field perturbations.

Various methods have been proposed to correct for physiologically induced field fluctuations. A common method to determine B_0 fluctuations are navigator based MRI techniques (Hu and Kim, 1994; Pfeuffer et al., 2002; Versluis et al., 2010) where phase variations are extracted from navigator scans. If they are spatially resolved, navigator scans are time-consuming and they usually extend the total acquisition time. Generally, navigator techniques do not allow to measure the field dynamics during the imaging readouts and assume that B_0 changes do not change between excitation and k-space acquisition. An other method determines breathing induced field fluctuations through the motion of the chest using a respiratory belt (Van Gelderen et al., 2007). The chest motion is translated into field changes in the imaging volume based on a calibration scan. This methods gets less reproducible if the subject changes its breathing behavior during the measurement.

Alternatively, ^{19}F NMR field probes (Barmet et al., 2008; De Zanche et al., 2008) enable monitoring of field dynamics up to 3rd-order spherical harmonics. Using this method, Vannesjo et al. (Vannesjo et al., 2015) investigated higher-order correction of motion-induced field perturbation for T_2^* weighted 2D-GRE acquisitions at 7 Tesla. Two high-order magnetic field monitoring approaches with different temporal resolutions have been proposed: 'concurrent' field monitoring (Vannesjo et al., 2012, 2015), where the complete field dynamics were monitored during the imaging readouts, and 'snapshot' field monitoring (Signe J. Vannesjo, B J Wilm, et al., 2013; Vannesjo et al., 2015), where field variations were determined in a small gradient-free time window. The field dynamics were incorporated in an extended signal model and an iterative conjugate-gradient algorithm was used for image reconstruction as described in (Wilm et al., 2011).

A zero-order field correction (constant $B_0(t)$ term) based on the snapshot field monitoring approach was recently investigated for segmented 3D-EPI acquisitions with different resolutions and subject motions (Schwarz et al., 2019).

In this project, a field probe system is used to monitor physiological field fluctuations during high-resolution T_2^* weighted 3D-EPI acquisitions (Stirnberg and Pflugfelder, 2013; Stirnberg and Stöcker, 2014; Zwanenburg et al., 2011) at 7 Tesla. Snapshot and concurrent field data are collected for the same experiments and field correction of up to first-order is investigated for both approaches based on temporal signal-to-noise ratio (tSNR) analysis. The measured zero- and first-order field perturbations (constant and linear $B_0(t)$ terms) are accounted for in image reconstruction. First-order field fluctuations lead to small k-space trajectory errors which are corrected for using GRAPPA operator gridding (GROG, ((Seiberlich et al., 2007)). The Eddy current compensation (ECC) performed by the scanner during signal reception is considered in the measured zero-order field term.

4.2 Methods

4.2.1 Sequence Implementation

In this project, a 2D-segmented gradient-echo 3D-EPI sequence (Poser et al., 2010; Stirnberg et al., 2017) was used for data acquisition. In contrast to conventional 2D-EPI or simultaneous multi-slice EPI (Larkman et al., 2001; Setsompop et al., 2012), an entire slab or the entire volume inside the RF transmitter is excited in 3D-EPI acquisitions.

As schematically depicted in Figure 4.1a, the 3D encoding is achieved using short blipped phase encoding gradients (G_{p1}) between two readout gradients (G_r) and employing step-wise updated gradients in the partition encoding direction (G_{p2}). Following one excitation, multiple phase encoding lines are acquired with changing polarity of the readout gradients, resulting in a k-space filling according to Figure 4.1b. Due to the alternating G_r, successive readout lines of an EPI echo train have different k-space sampling directions ('even' and 'odd' lines). The total number of readout lines per excitation is called EPI factor.

The sequence is furthermore extended by segmentation in $p1$-direction (Stirnberg and Pflugfelder, 2013; Stirnberg and Stöcker, 2014), following the original idea of interleaved multi-shot 2D-EPI (Butts et al., 1994; McKinnon, 1993). Instead of acquiring the complete k-space data of one partition encoding step in a single EPI echo train, it is acquired in N_{seg} successive runs with a N_{seg}-fold larger gap between the phase encoding steps and $1/N_{seg}$ reduced EPI factor. The number N_{seg} is referred as segmentation factor. An exemplary k-space trajectory with a segmentation factor of 3 and EPI factor of 4 is illustrated in Figure 4.1b. The filling of k-space with successive EPI echo trains is indicated by a colour gradient. Using this loop structure, neighboring segments are acquired as close as possible in time.

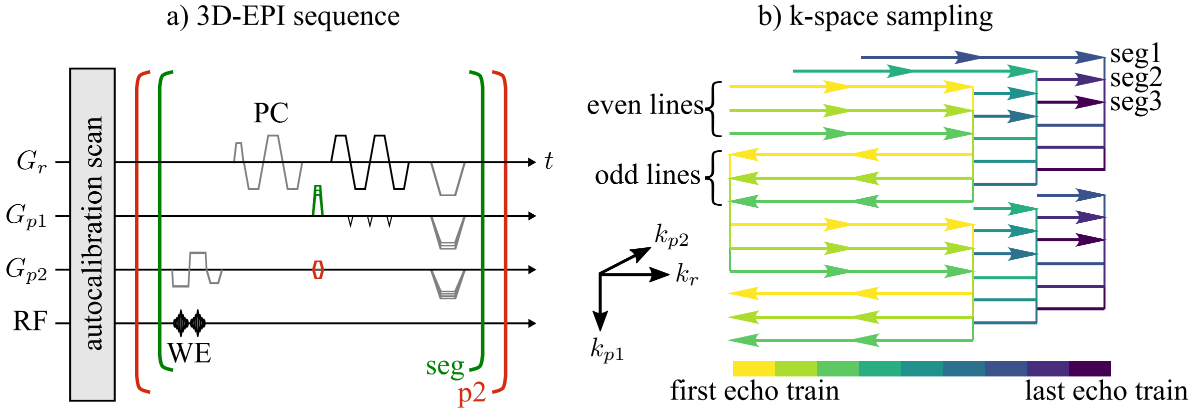

Figure 4.1: a) Schematic sequence diagram and loop structure of a segmented 3D-EPI sequence with a segmentation factor of 3 and EPI factor of 4. Before the actual experiment, a separate fast low angle shot (FLASH) autocalibration scan is acquired and EPI phase correction scans (PC), consisting of 3 EPI readouts, are measured at the beginning of each EPI echo train. The fat signal is suppressed using a slab-selective binomial water excitation pulse (Hore, 1983) (WE). Data is acquired during the flat top time of the readout gradients. b) Corresponding k-space filling for the 3-fold segmented 3D-EPI acquisition. The color gradient indicates the temporal filling of k-space for successive EPI echo trains. Due to the loop structure of the sequence, all segments of one partition are acquired before proceeding to the next partition. Depending on the sign of the readout gradient and the resulting k-space sampling direction, readout lines are referred as even or odd lines.

4.2.2 Field Monitoring

Magnetic field changes during the measurements were monitored using a Clip-On Camera (Skope Magnetic Resonance Technologies, Zurich, Switzerland) which consists of 16 ^{19}F NMR field probes placed around the head receive coil ((De Zanche et al., 2008), cf. section 2.10). The excitation of the field probes is controlled by an external trigger applied before the acquisition of the phase correction scans as shown in Figure 4.2. Starting field monitoring in the k-space center (in contrast to a trigger placement after the phase correction scans) minimizes the dephasing of the field probe signal and thereby reduces signal loss during the EPI echo train. Two magnetic field monitoring approaches with different temporal resolutions have been proposed: 'concurrent' field monitoring (Vannesjo et al., 2012, 2015), where the complete field dynamics are monitored during the imaging readouts, and 'snapshot' field monitoring (Signe J. Vannesjo, B J Wilm, et al., 2013; Vannesjo et al., 2015), where field variations are determined in a small gradient-free time window. In this work, both methods were investigated and will be introduced in the following.

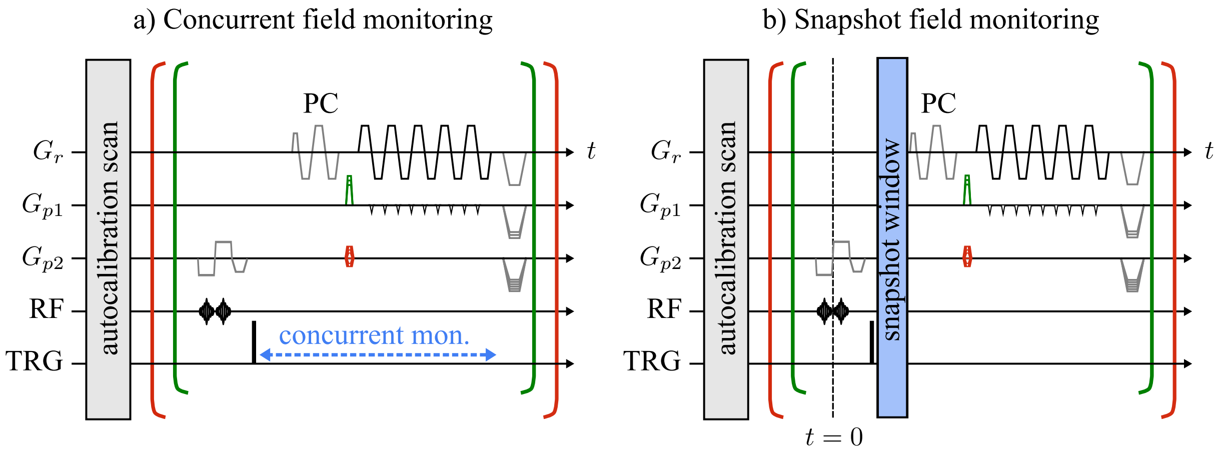

Figure 4.2: Sequence diagram with a) concurrent and b) snapshot field monitoring. The field probes are excited using an external trigger (TRG) that is applied before acquisition of the phase correction scans (PC). a) Full field monitoring during the whole readout. b) The field changes are fitted from the probe signals acquired during a gradient-free snapshot window.

4.2.2.1 Concurrent Field Monitoring

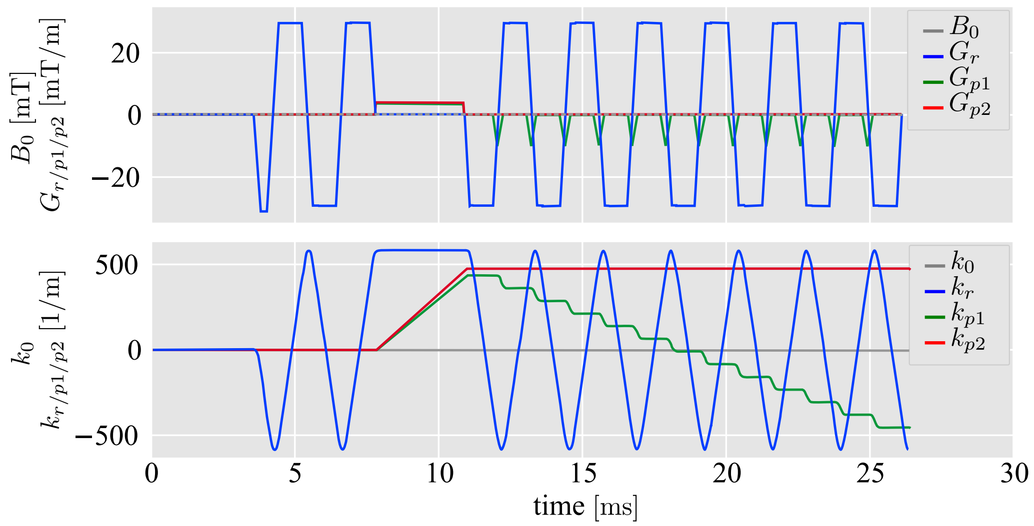

Figure 4.3: Example of concurrent field monitoring of a one 3D-EPI echo train. The gradient shapes and magnetic field changes (B_0) during one EPI echo train are shown on top. The corresponding trajectories through k-space and the phase term k_0 are depicted on the bottom.

The concurrent approach monitors the field dynamics for the whole EPI echo train (cf. Figure 4.2b). The vendor software determines the gradients shapes and the corresponding k-space data by fitting spherical harmonic spatial basic functions to the phase evaluation of the NMR field probes (cf. Section 2.10). The 0^{th}-order term k_0 represents a phase term on the MR signal, the 1^{st}-order terms k_r, k_{p1} and k_{p2} describe the k-space encoding. An example for an EPI echo train monitored with the field probes system is shown in Figure 4.3. A limitation of concurrent field monitoring is the signal loss due to gradient dephasing and T_2^* decay. This can be particularly problematic for long echo trains or very high-resolution acquisitions.

4.2.2.2 Snapshot Field Monitoring

Snapshot field monitoring is based on the assumption that relatively slow field perturbations, such as those resulting from deep breathing, are constant during an imaging readout and that such field changes can be described by a single field measurement per EPI echo train. The signal of the field probes is measured during a gradient-free snapshot window of a few ms as shown in Figure 4.2a. Based on this measurement, field variations are fitted by the vendor software.

In contrast to concurrent field monitoring, the snapshot method is not limited by signal decay of the field probes, but does not allow a correction of fast field fluctuations, such as eddy currents, during the readout. An example of a snapshot measurement with fitted constant field terms $B_{0,fit}$ and linear field terms (constant gradients) $G_{r/p1/p2,fit}$ is shown in Figure 4.4.

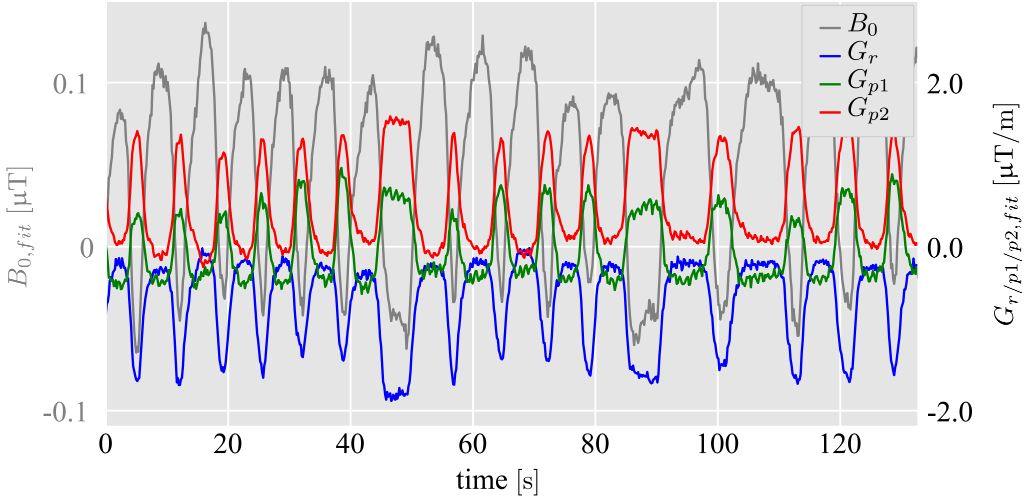

Figure 4.4: Example of snapshot field monitoring during a whole 3D-EPI experiment where the subject was instructed to repeat a movement of the hand from waist to chin. Field fluctuations were fitted for each echo train from the data acquired during the gradient-free snapshot window. Compared to concurrent field monitoring, the snapshot method only determines one variation value per echo train from the total magnetic field or the magnetic gradient shapes.

4.2.2.3 Field Fluctuations

The aim of this project is the correction of field fluctuations of up to first-order. Due to hardware imperfections or physiology, the signal equation (Equation 2.16) changes into

$$S(\mathbf{k}) = \int_{volume} M_{x,y}(\mathbf{r}, t = 0) e^{-i2\pi k_0(t)} e^{-i2\pi(\mathbf{k}+\delta\mathbf{k}(t))\mathbf{r}} \mathrm{d}^3 r. \tag{4.1}$$

0^{th}-order field perturbations $k_0(t)$ correspond to a phase shift of the acquired signal and 1^{st}-order field changes lead to small k-space shifts $\delta\mathbf{k}(t)$ away from the nominal trajectory. These deviations from the Cartesian trajectory are schematically shown in Figure 4.5.

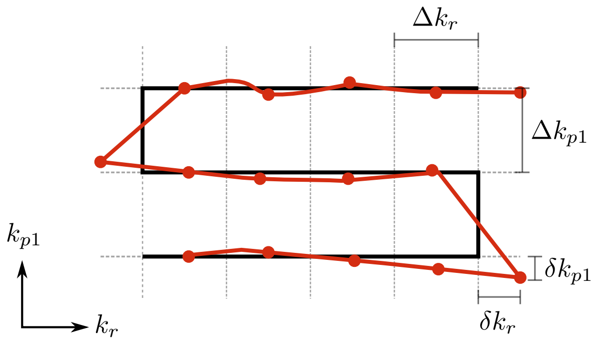

Figure 4.5: The nominal Cartesian trajectory of an EPI sequence is shown in black. Due to physiology- or eddy-current-induced 1^{st}-order field variations during data acquisition, the effective trajectory deviates from the nominal k-space sampling as schematically represented in red.

The field deviations for snapshot field monitoring are calculated using the fitted field values. The snapshot approach is based on the assumption, that they increase linearly with time t after the excitation pulse. The 0^{th}-order frequency modulation is thus given by

$$k_0(t) = \frac{\gamma}{2\pi} \cdot B_{0,fit} \cdot t \tag{4.2}$$

and the 1^{st}-order k-space deviations are determined according to Equation 2.14 by

$$\delta k_{r/p1/p2}(t) = \frac{\gamma}{2\pi} \cdot G_{r/p1/p2,fit} \cdot t. \tag{4.3}$$

For the concurrent field monitoring approach, the k-space values $k_0(t)$ and $k_{r/p1/p2}(t)$ are measured. To reduce noise, they are filtered with a $50\,\mathrm{kHz}$ Butterworth lowpass filter. Knowing the delay between the MR scanner and the field probe measurement (see synchronization scans in Section 2.10) and the exact timing of the EPI echo train, the data are merged for every acquired k-space line. First-order k-space shifts correspond to the difference between the measured and the nominal Cartesian k-space trajectory.

Figure 4.4 depicts k_0 and the relative k-space shifts $\delta k_{r/p1/p2}/\Delta k_{r/p1/p2}$ of three EPI echo trains acquired with snapshot and concurrent field monitoring, respectively. In the experiment, the subject was instructed to generated magnetic field fluctuations by moving his hand from waist to chin. Since the k-space shifts for snapshot field monitoring were calculated based on the fitted field values per echo train (see Equations 4.2 and 4.3), they increase linearly with increasing echo number. In addition, the shifts from $-k_{max}$ to k_{max} differ for even and odd line numbers due to the EPI-typical k-space sampling shown in Figure 4.1b. The k-space shifts for concurrent field monitoring along the echo trains are both physiology- and hardware-induced. Differences between shifts of even and odd lines are most prominent in the readout direction. If the exact k-space trajectory is not known, such as for snapshot field monitoring or normal acquisitions without any field monitoring, these eddy-current-induced inconsistencies between even and odd echoes in readout direction are usually corrected by integrated phase correction. Therefore, phase correction scans are acquired at the beginning of each readout train (cf. Figure 4.2). If not corrected, the reconstructed images show the specific EPI Nyquist ghost artifacts. Concurrent field monitoring eliminates the need of phase correction acquisitions.

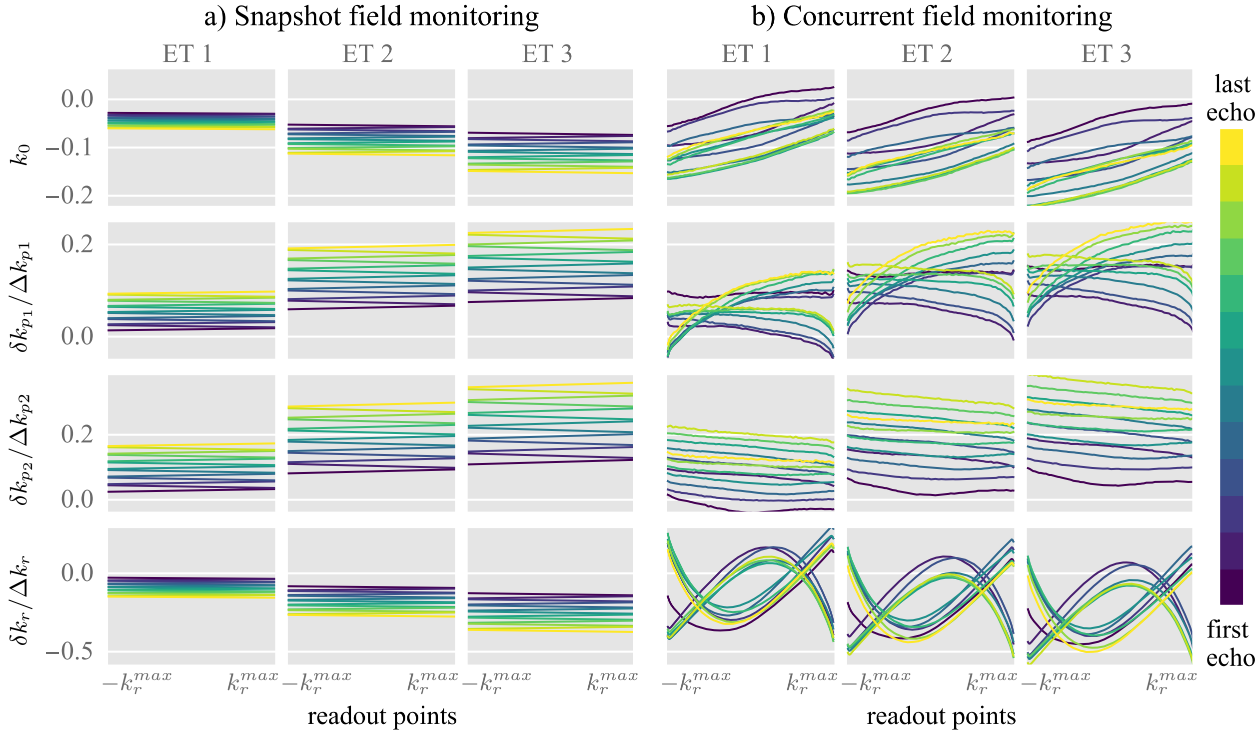

Figure 4.6: Field deviations during all readouts of an echo train for a) snapshot and b) concurrent field monitoring. Field fluctuations were generated by a hand-to-chin movement of the subject. The relative k-space shifts and the k_0 fluctuations are shown for all 13 echoes of three echo trains.

4.2.3 Eddy Current Compensation of the MR Scanner

Fast gradient switching such as in EPI sequences induces eddy currents in the MR system, which lead to time-varying gradients and magnetic field shifts. To reduce image artifacts, the MR scanner employs gradient and RF eddy current pre-emphasis during transmission and signal eddy current compensation (ECC) during reception. The ECC comprises a frequency modulation during signal reception. The NMR field probes system measures the actually applied gradients, but does not know the B_0 modulation employed by the scanner during signal reception. Correcting the data for the B_0 fluctuations detected with snapshot or concurrent field monitoring, without accounting for the B_0 variations that have already been compensated by the scanner (ECC), leads to artifacts.

Snapshot field monitoring only allows the correction of slow field variations, e.g. resulting from physiology. To separate physiological frequency modulations from scanner-induced receive frequency modulations, the fitted field values of a reference phantom measurement are subtracted from the in-vivo measurement as illustrated in Figure 4.7.

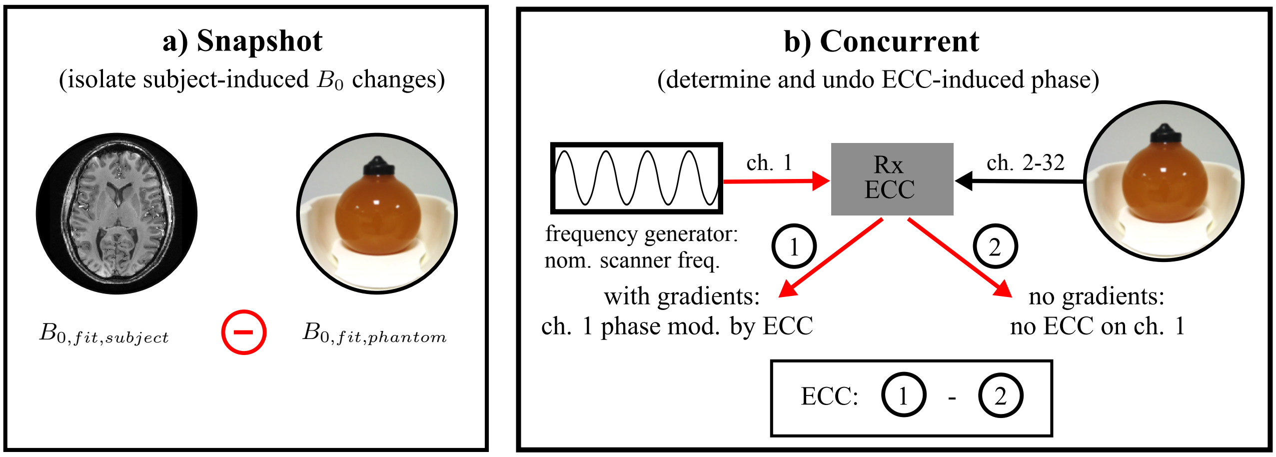

Figure 4.7: Consideration of scanner induced B_0 eddy current compensation for a) snapshot and b) concurrent field monitoring. For the snapshot approach, physiological frequency modulations are separated from scanner-induced receive frequency modulations using the fitted field values of a reference phantom measurement. For concurrent field monitoring, the frequency modulation performed by the scanner is determined using an RF generator. The sinusoidal output signal is fed into one of the receiver channels (ch. 1) and two measurements, one with imaging gradients and one without any gradients, are performed. The scanner-induced phase modulation corresponds to the phase difference of the raw data of channel 1.

For concurrent field monitoring, the scanner-induced receive frequency modulation is determined using an external RF signal generator as proposed by Ma et al. (Ma et al., 2019) and reverted prior to field correction and image reconstruction. Using the RF generator, a sinusoidal output signal with the nominal scanner frequency (Larmor frequency, cf. Equation 2.5) is fed directly into one of the 32 receiver channels as illustrated in Figure 4.7. The generator is furthermore synchronized to the 10 MHz clock of the scanner.

To measure the frequency modulations applied by the scanner for a given protocol, two phantom measurements are carried out. A coupling of imaging signal from channel 2-32 into channel 1 is avoided by setting the scanner transmit voltage to zero during both measurements. The first measurement is performed using the same sequence and protocol as the in-vivo scan. In the second measurements, the timing of RF pulses and readout ADCs is kept, but no gradients are played out. While in the first measurement the phase of the signal is modulated, in the second measurement no ECC is applied by the scanner due to the missing gradients. The scanner-induced phase modulation corresponds to the phase difference of the raw data of channel 1. The receive ECC can be removed from the measured in-vivo data by demodulation with this phase term or from the measured k_0 before field correction as shown in Figure 4.8.

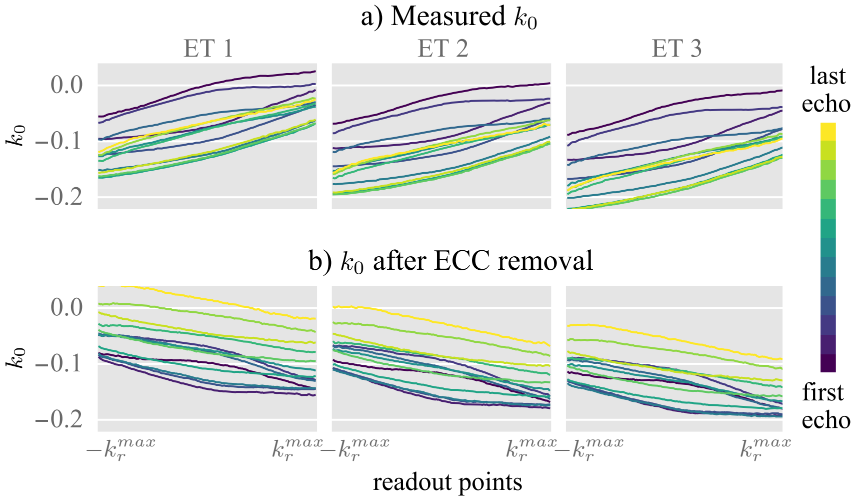

Figure 4.8: 0^{th}-order field fluctuations using concurrent field monitoring shown for all readouts of three echo trains. Top: k_0 term measured with concurrent field monitoring. Bottom: 0^{th}-order field fluctuations remaining after removal of the ECC performed by the MR scanner during signal reception.

Figure 4.9 shows examples of the mean value of the measured ECC frequency per readout applied by the scanner for two typical EPI acquisitions of $1\,\mathrm{mm}$ isotropic resolution with different orientations of the readout axis. In the saggital measurement (Figure 4.9a), the readout axis was oriented along the z-axis of the scanner, which is the direction of the main magnetic field. For this orientation, the imaging gradients induce strong eddy currents and therefore the scanner applied larger ECC frequencies. The changes of the mean frequency of the even readouts during one echo train are $\approx 30-40\,\mathrm{Hz}$, compared to $\approx 10\,\mathrm{Hz}$ for the transversal measurement (Figure 4.9b). The sign of readout gradients changes in the EPI sequence between even and odd readout lines (cf. Figure 4.1). This change of sign is reflected in the signs of the the mean ECC frequency.

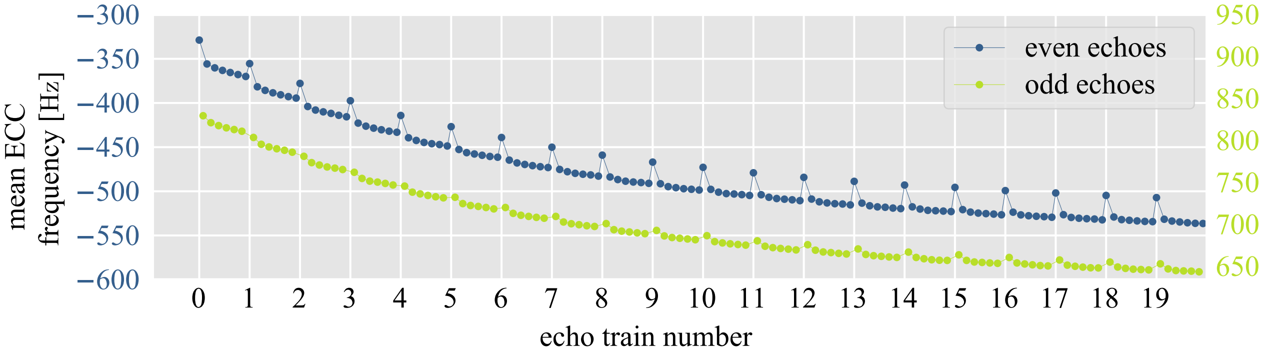
a) Mean ECC frequency of a saggital EPI measurement

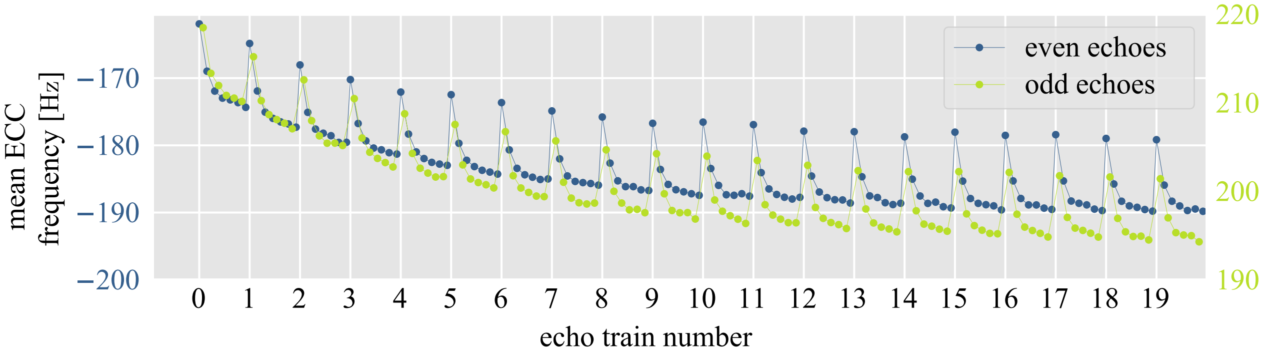
b) Mean ECC frequency of a transversal EPI measurement

Figure 4.9: Mean scanner-induced ECC frequency per readout for a typical EPI protocol with $1\,\mathrm{mm}$ isotropic resolution acquired with a) saggital orientation (readout in z-direction) and b) transversal orientation (readout in x-direction) . The plots show that the sagittal measurement induces more eddy currents and therefore the ECC frequency is much higher and has higher deviations between even and odd lines and between the different readouts during an echo train.

4.2.4 Data Acquisition

All experiments were carried out on a 7T Magnetom scanner (Siemens Healthineers, Erlangen, Germany) utilizing a 32-channel head coil (Nova Medical, Wilmington, USA). For field monitoring, the NMR field probes were placed between the transmit and the receive part of the coil using the upper frame of a prototype field probe holder (Brunheim et al., 2020) and fixing the probes of the bottom frame with tape at approximately the designed positions. The probe positioning, as schematically shown in Figure 4.10, was conditioned for the best approximation to the field dynamics, taking into account the limitations of the coil architecture. The field probe number 3 marked in red was defective and could not be used during the experiments. All field measurements were performed with the remaining 15 field probes. However, the probe positioning on the field probe holder was conditioned for 16 and not 15 field probes. The influence of a missing field probe on the field dynamics was investigated in the Appendix in Section 6.2.1.

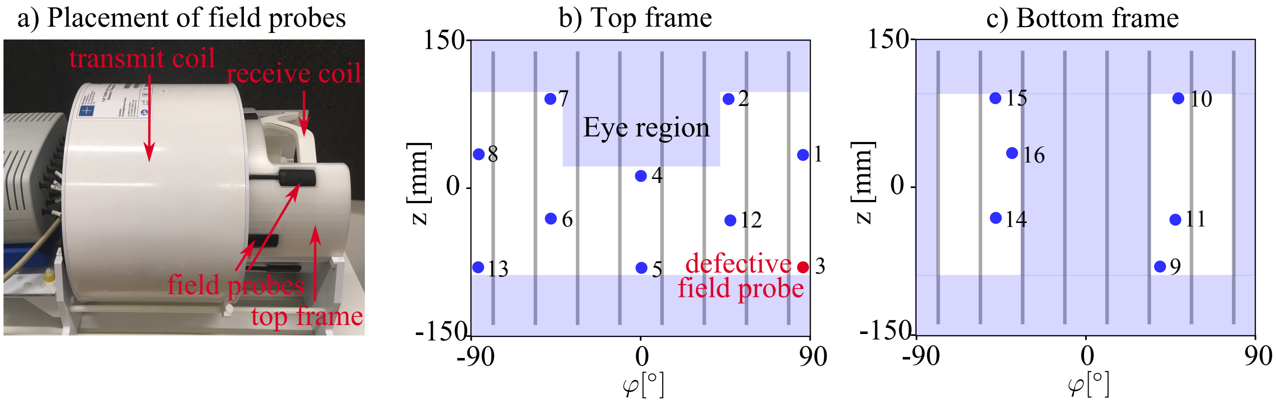
a) Placement of field probes b) Top frame c) Bottom frame

Figure 4.10: Field probe holder and probe positioning. a) The 3D-printed top frame is placed between the transmit and the receive part of the head coil (photo courtesy of Sascha Brunheim). The probe positioning for the Nova coil architecture is schematically shown for b) the top and c) the bottom frame. The tuning capacitors' end-ring zones of the birdcage transmit coil and the cutout zone in the receive part of the coil are marked in light blue. The 16 gray lines indicate the strip lines of the birdcage transmit coil where no probes should be placed. The defective field probe that could not be used during the experiment is marked in red.

For a field correction of up to fist order, substantially better image results were observed when using a 1^{st}-order fit compared to a 2^{nd}-order spherical harmonics fit for the processing of the monitored field probes signal (cf. Appendix, Section 6.4). Therefore, a 1^{st}-order spherical harmonic field model was used for all field monitoring experiments.

Image data were acquired using two different T_2^* weighted segmented 3D-EPI protocols:

A) $1\,\text{mm}$ isotropic resolution, FOV $= 194\times194\times160\,\text{mm}^3$ (transversal), $TE/TR_{shot} = 19/83.3\,\text{ms}$, $TR_{vol} = 200\,\text{s}$, $1.1\,\text{ms}$ echo spacing, flip angle 9°, 6 volume repetitions and a readout bandwidth of $1289\,\text{Hz/pixel}$. The protocol applied slab-selective binomial water excitation of $0.3\,\text{ms}$ duration with a bandwidth-time product of 25 yielding a slab thickness of approximately $144\,\text{mm}$ and 15-fold segmentation was applied along the first phase-encoding direction (cf. Figure 4.1b) with an EPI factor of 13. Additionally, a fast low angle shot (FLASH) reference scan (Ivanov et al., 2015) with 36×36 fully sampled calibration lines was acquired.

B) $1\,\text{mm}$ isotropic resolution, FOV $= 196\times196\times160\,\text{mm}^3$ (transversal), $TE/TR_{shot} = 19/31.2\,\text{ms}$, $TR_{vol} = 25\,\text{s}$, $1.1\,\text{ms}$ echo spacing, flip angle 6°, 15 volume repetitions and a readout bandwidth of $1276\,\text{Hz/pixel}$. The protocol was 5-fold segmented with an EPI factor of 13. Furthermore, the scan was accelerated with an acceleration factor of $\text{R} = 3\times1$ and 36×36 FLASH calibration lines were acquired.

Physiological field changes were induced by instructing the subject to perform different tasks. For protocol A, these tasks were breathing deeply and repeating a hand movement from waist to chin. For the accelerated protocol B, a scan with normal breathing was acquired in addition to the two tasks.

Field changes during the measurement were monitored during a gradient-free snapshot window of $3\,\mathrm{ms}$ after excitation of the field probes and during the whole echo train including the initial phase correction scans. Using this monitoring scheme, it is possible to obtain concurrent and snapshot field data from the same experiment and to compare the resulting field corrections. Note that only the snapshot approach requires the default phase corrections scans. For the accelerated protocol B with minimal $TR_{shot} = 31.2\,\mathrm{ms}$, only every 5^{th} echo train was monitored, resulting in an interleave TR (iTR) of $156\,\mathrm{ms}$ for the field probes. Too short iTR can lead to spin echoes and stimulated echoes of previous excitations. Therefore, Skope recommends a minimal iTR of the field probes of $150\,\mathrm{ms}$.

In addition, phantom measurements as described in Section 4.2.3 were performed for both protocols to account for the ECC performed by the scanner during signal reception.

4.2.5 Image Reconstruction with Correction of Field Fluctuations

The raw data were corrected for field fluctuations prior to image reconstruction. For the 0^{th}-order field correction, the raw data signal is demodulated by the phase

$$\varphi_0(t) = 2\pi k_0(t), \tag{4.4}$$

where t denotes the time after the imaging RF pulse excitation. Prior to phase demodulation, the ECC performed by the scanner was removed from k_0 as described in Section 4.2.3 for snapshot and concurrent field monitoring. For the 1^{st}-order correction, the relative k-space shifts according to 2.14 are given by

$$\frac{\delta k_{r/p1/p2}(t)}{\Delta k_{r/p1/p2}} = \delta k_{r/p1/p2}(t) \cdot FOV_{r/p1/p2}. \tag{4.5}$$

The relative k-space shifts are the basis for the reconstruction using GRAPPA operator gridding (GROG) ((Seiberlich et al., 2007), Section 2.2.2.3). GROG uses the concepts of parallel imaging and allows to shift data sampled along a non-Cartesian trajectory to a Cartesian grid. The GROG weights were determined using the low resolution FLASH dataset and based on them, the GRAPPA operator for the different k-space shifts was calculated. The data points were shifted to the Cartesian k-space location by applying these operators to the data. Since k-space shifts due to physiological field fluctuations are generally small ($< 1\Delta k$), GROG is well-suited for this application.

For reconstructions with snapshot field correction or without field correction, the inconsistencies between even and odd echoes were corrected based on the phase correction scans acquired at the beginning of each readout train. The 1^{st}-order concurrent field data already contain this information in the measured k-space trajectory and no additional phase correction is needed for concurrent field correction.

The undersampled data measured with protocol B were reconstructed utilizing the developed Python toolbox for image reconstruction and using a 3D reconstruction kernel of size $3 \times 3 \times 3$. For this protocol, field fluctuations were monitored only for every 5^{th} echo train. As physiological field fluctuations induced by breathing or hand movement can be assumed slow, the missing field data were estimated using spline interpolation. In order to interpolate only physiological field changes, the 0^{th}-order ECC performed by the scanner was first removed for the snapshot and the concurrent field data. For snapshot field monitoring, the data were directly interpolated from the fitted field values. For concurrent field monitoring, the field deviations from the nominal trajectory were interpolated separately for each timepoint of the EPI echo train. However, the concurrent field data contains eddy-current-induced field fluctuations. Such an interpolation implies that successively sampled echo trains experience the same eddy currents. But for larger jumps in k-space, the phase and partition encoding gradient shapes change significantly and induce stronger eddy currents. This effect is not considered by the interpolation.

4.2.6 Data Processing and Analysis

The influence of snapshot and concurrent field correction on the image quality is shown using difference images. However, the images corrected for field fluctuations show a small pixel offset compared to the images reconstructed without field correction (‘uncorrected’ images). Although the mean k_0 value is set to zero, the phase modulation due to 0^{th}-order field correction leads to a small shift in image space that dominates the difference images if not accounted for. Therefore, the field corrected datasets were registered to the uncorrected data using FLIRT (FSL (Greve and Fischl, 2009; Jenkinson et al., 2002, 2012; Jenkinson and Smith, 2001)) with three degrees of freedom (translation only). Furthermore, the same maps for the correction of intensity inhomogeneities (N4 bias field correction, (Tustison et al., 2010)) were used for the compared datasets. The different processing steps were illustrated in the flowchart in Figure 4.11.

Temporal signal-to-noise ratio (tSNR, ratio of voxel-wise mean and standard deviation of time series) has been shown to be a good measure for temporal signal fluctuations due to system instabilities and physiological processes (Krüger and Glover, 2001; Triantafyllou et al., 2005). This metric is used in this work to analyze the effect of snapshot and concurrent field correction. For the tSNR calculation, the datasets were motion corrected using MCFLIRT (FSL, (Jenkinson et al., 2002)). For the measurements performed with protocol B, the first repetition was not considered for the tSNR determination due to transient signal effects. The tSNR maps were analyzed in the brain region extracted using BET (FSL, (Smith, 2002)).

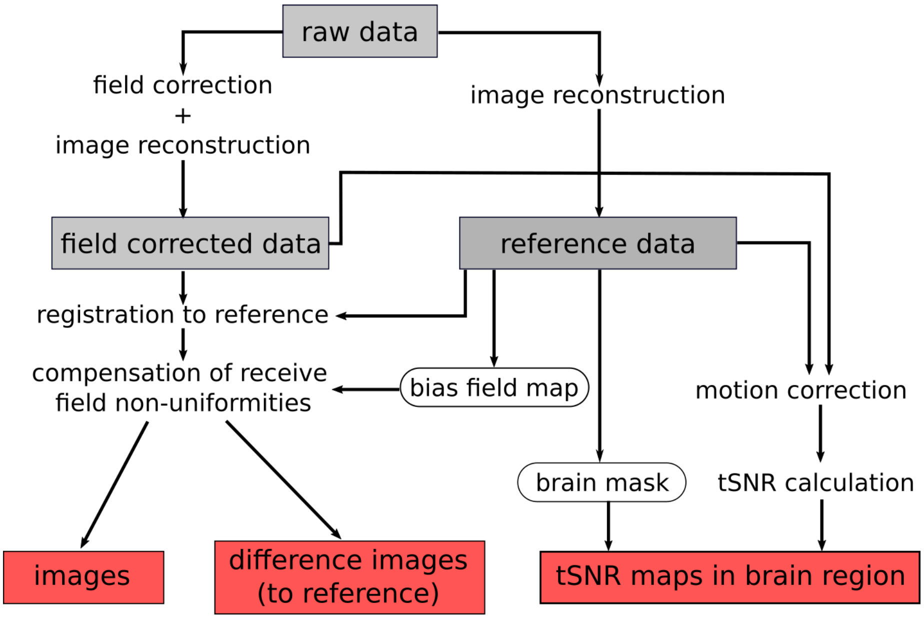

Figure 4.11: Flowchart illustrating the different processing steps from raw data to the images, difference images and tSNR maps shown in the results. The dataset reconstructed without field correction is referred as reference data. The registration to the reference data was performed using FSL's FLIRT, the bias field map was determined using the N4 bias field correction, the brain mask using FSL's BET and motion correction was performed using FSL's MCFLIRT.

Due to the different task during the measurement (normal/deep breathing, hand-to-chin movement), image quality and tSNR were influenced by motion of the subject in addition to the field fluctuations. To describe the mean apparent head motion between the different volumes in the time series, the mean framewise displacement (FD) (Power et al., 2012) was calculated based on the reference data transformation matrix determined by MCFLIRT. The transformation consists of a combination of 3 displacement and 3 rotation components and the rotations were converted into a translational displacement by projection on the surface of a sphere of radius $50\,\mathrm{mm}$. Furthermore, the mean 0^{th}-order fluctuations μ_k^0 and the mean relative k-space shifts $\mu_k^{r/p1/p2}$ during an experiment were calculated based on the snapshot field monitoring data. The given terms correspond to the mean differences between minima and maxima of the field fluctuations in the middle of the echo train at time $t = TE$.

4.3 Results

The mean field fluctuations induced during the different measurements and the mean framewise displacement (FD) as a metric for the apparent head motion are summarized in Table 4.1. As expected, the largest field fluctuations were measured while the subject repeated a movement of his hand from waist to chin. For protocol A, this hand movement induced strong field fluctuations with mean phase changes of $\mu_k^0 = 0.132$ (corresponding to mean frequency variations of $7.34\,\mathrm{Hz}$) and mean k-space shifts of $\mu_k^{r/p1/p2} > 0.2$ in all three directions. For protocol B, a different subject was measured and the fields changes induced by the hand-to-chin movement were generally smaller.

For the deep breathing tasks, field fluctuations were dominated by the 0^{th}-order term and by the 1^{st}-order shifts in phase encoding direction. This corresponds to the main direction of chest movement during deep breathing. However, field fluctuations were smaller than for the hand movement. Besides, breathing very deeply into the chest led to a stronger apparent head motion with FD$= 0.28\,\text{mm}$ compared to the motion during normal breathing (FD$= 0.10\,\text{mm}$) or during the hand-to-chin task (FD$= 0.26\,\text{mm}$).

Generally, mean 1^{st}-order field fluctuations of $\mu_k^{r/p1/p2} < 0.03$ were dominated by noise and thus, only the 0^{th}-order field term was relevantly influenced by normal breathing.

		μ_k^0	$\mu_k^{r/x}$	$\mu_k^{p1/y}$	$\mu_k^{p2/z}$	FD [mm]
A	deep breathing	0.051	0.020	0.086	0.038	0.55
	hand-to-chin	0.132	0.218	0.203	0.210	0.19
B	normal breathing	0.021	0.009	0.017	0.016	0.08
	deep breathing	0.015	0.022	0.112	0.060	0.33
	hand-to-chin	0.073	0.102	0.131	0.109	0.24

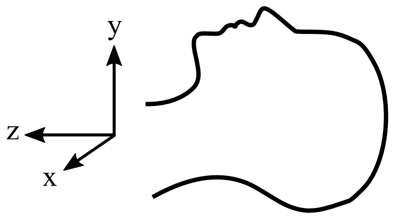

Table 4.1: Mean 0^{th}- and 1^{st}-order field fluctuations and mean framewise displacement (FD) for all 5 experiments performed with protocol A and B, respectively. The mean peak-to-peak field fluctuations were determined based on the snapshot field data at time $t = TE$. The mean 1^{st}-order fluctuations $\mu_k^{r/p1/p2}$ are given in mean relative k-space shifts. The directions of the imaging gradients relative to the subject are schematically illustrated on the right image.

Figure 4.12 shows a subset of the field fluctuations (k_0 and relative k-space shifts) induced during the hand-to-chin experiment with protocol A. In contrast to Figure 4.4, only the mean values per readout for snapshot and concurrent field monitoring are shown. The general behavior of the field fluctuations was similar for the two monitoring methods.

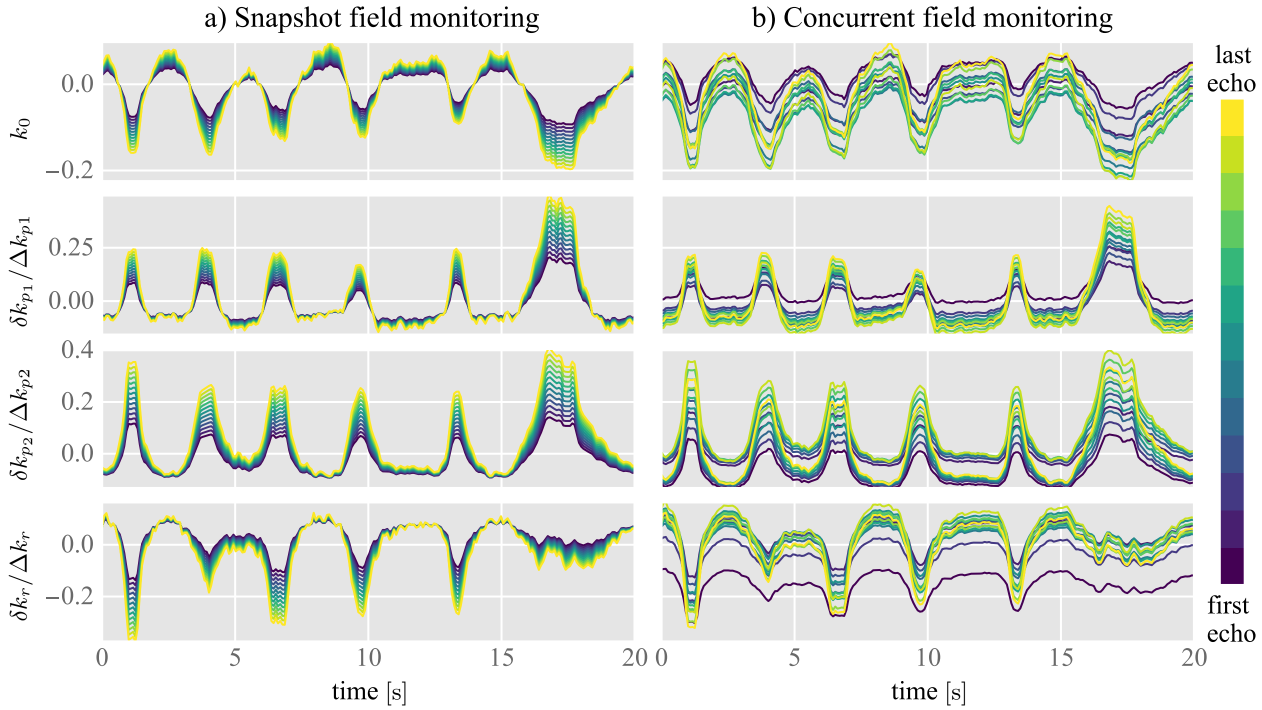

Figure 4.12: k_0 fluctuations and relative k-space shifts $\frac{\delta k}{\Delta k}$ averaged over each readout line. The temporal development of the mean field fluctuations are shown for all 13 readouts of the EPI echo train for a) snapshot and b) concurrent field monitoring. The field fluctuations were induced by a repeated hand-to-chin movement of the subject throughout the scan.

Images acquired during hand-to-chin movement (Figure 4.13 and 4.15) or deep breathing (Figure 4.14) show artifacts in the reconstructed images. Image artifacts are more severe in the hand-to-chin experiments, especially in the anterior part of the head. For deep breathing, they are more evenly distributed over the head. The correction of field fluctuations achieved a considerable improvement in image quality for both field monitoring approaches. Images acquired during normal breathing (Figure 4.16) do not show this kind of artifacts, and therefore the correction of field fluctuations did not achieve a visible improvement in image quality. Using the interpolated field dynamics, concurrent field correction even led to a slight deterioration of image quality.
The effect of field correction was additionally visualized by means of a difference image of the uncorrected reference image to the field corrected image. They were scaled relative to the maximum displayed value. In the hand-to-chin experiments, field correction of up to 1st-order achieved a clear improvement compared to only 0th-order correction. The improvement is visible in the images and particularly in the difference images.

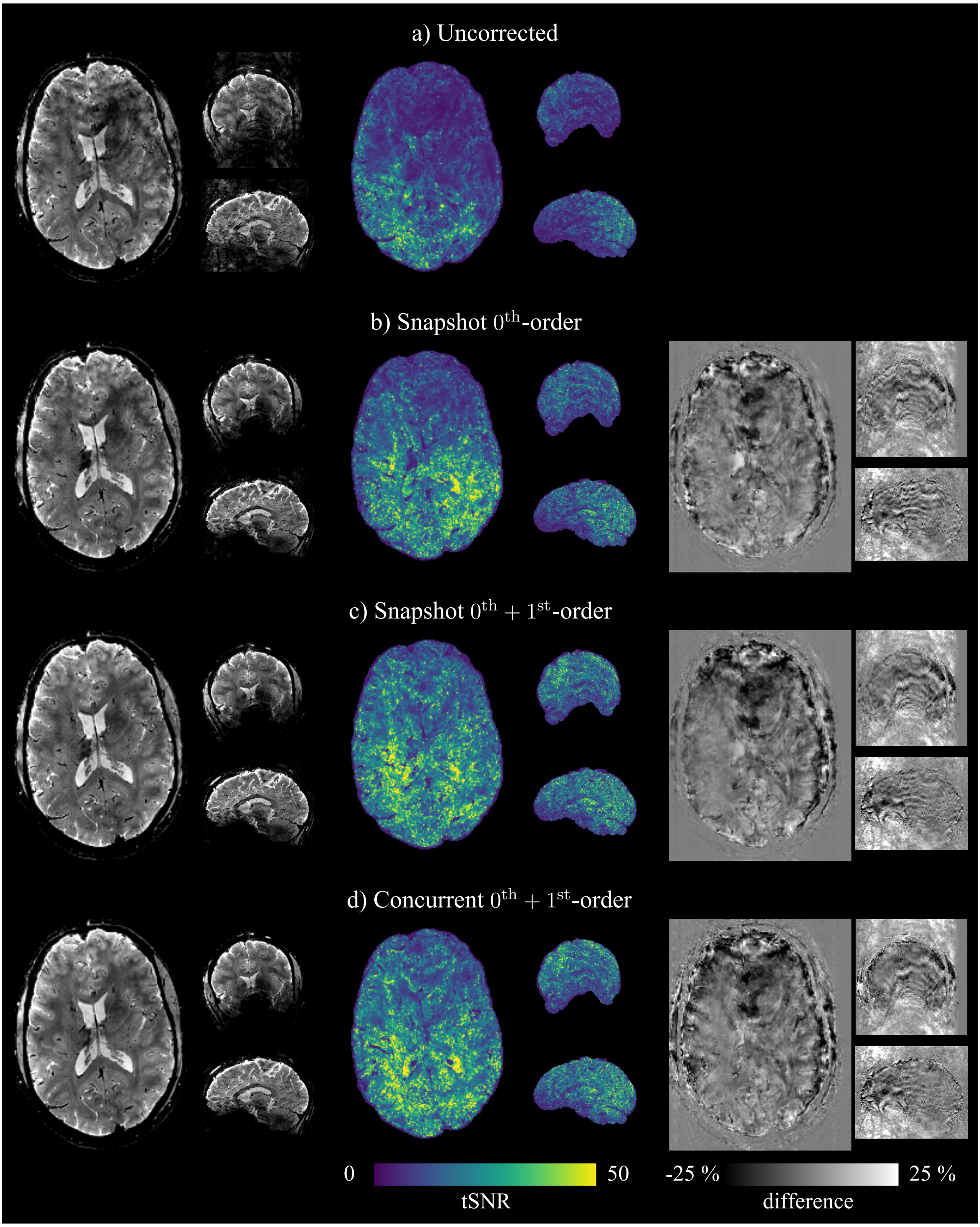

Figure 4.13: Example slices for one volume in the time series for the 1 mm segmented 3D-EPI measurement acquired with protocol A. The subject induced field fluctuations by repeating a hand-to-chin movement. The effect up to 1st-order field correction using snapshot and concurrent field monitoring is visible in the reconstructed images (left), in the tSNR maps determined from the time series (middle) and in the difference to the uncorrected reference image (right).

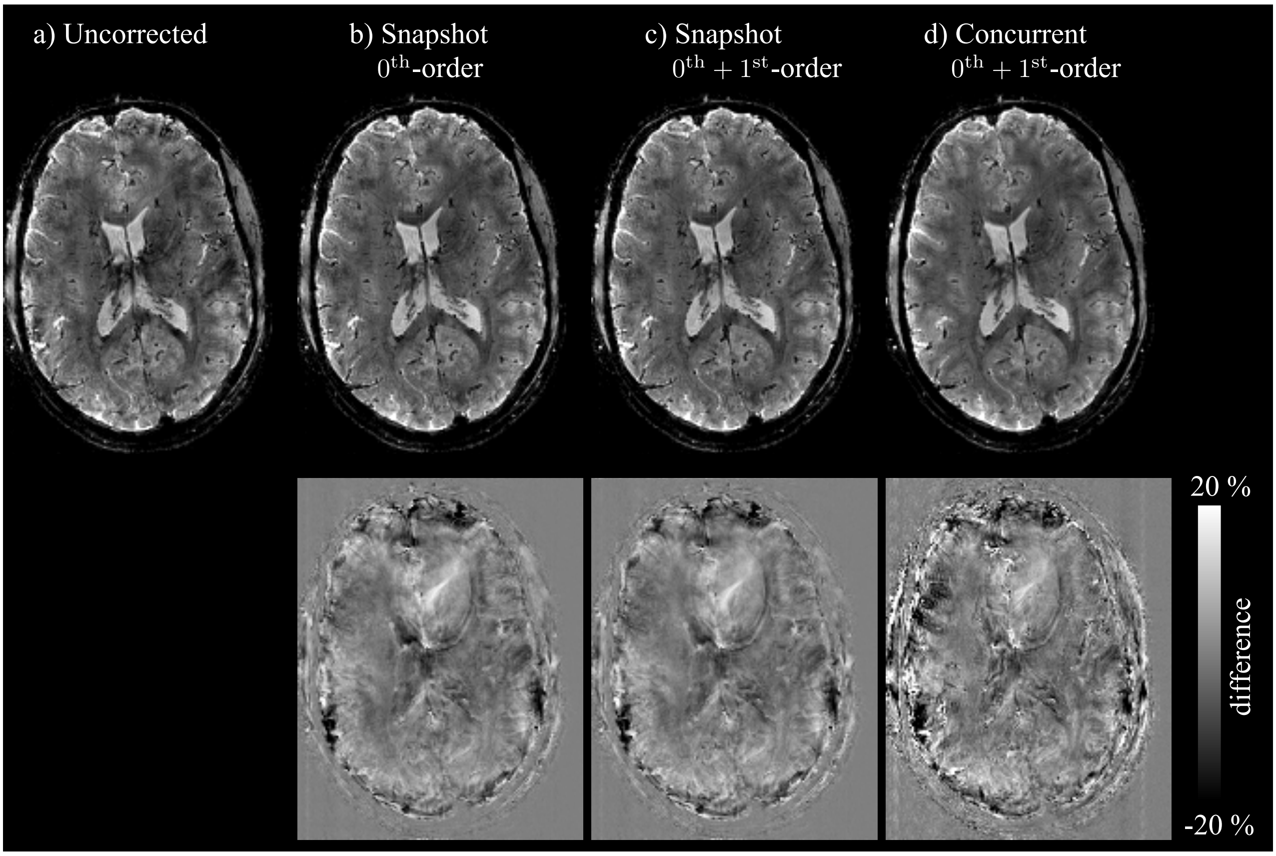

Figure 4.14: The effect of the different field correction methods for the deep breathing experiment performed with protocol A. Axial example slices are shown of the a) uncorrected reference image, b) 0^{th}-order field correction with the snapshot method, c) 0^{th}- and 1^{st}-order snapshot correction and d) 0^{th}- and 1^{st}-order field correction with the concurrent approach. Difference images between the uncorrected image and the field corrected images (scaled relative to the maximum displayed value) are depicted on the bottom.

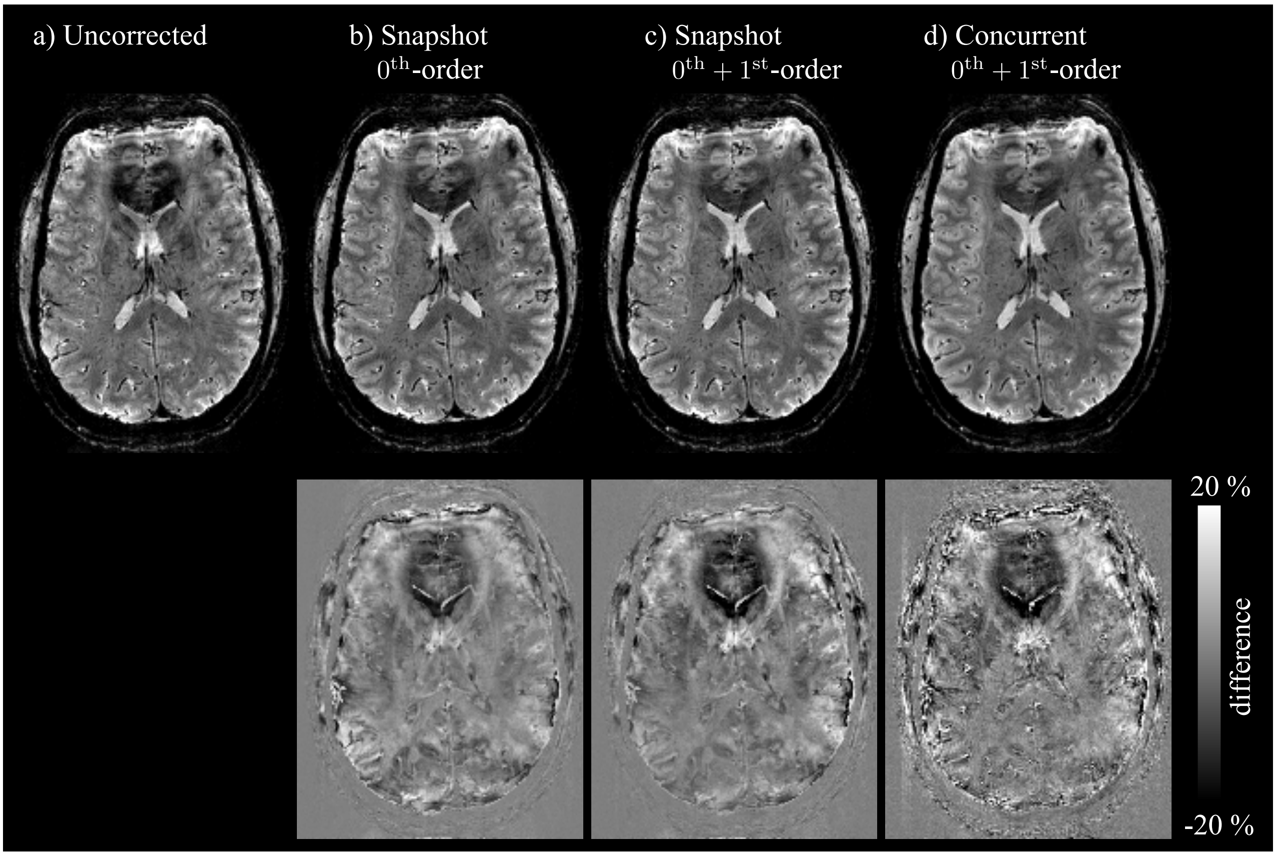

Figure 4.15: The effect of the different field correction methods for the hand-to-chin movement experiment performed with protocol B. Axial example slices of the a) uncorrected reference image and b)-d) the field corrected images. Difference images between the uncorrected image and the field corrected images are shown on the bottom.

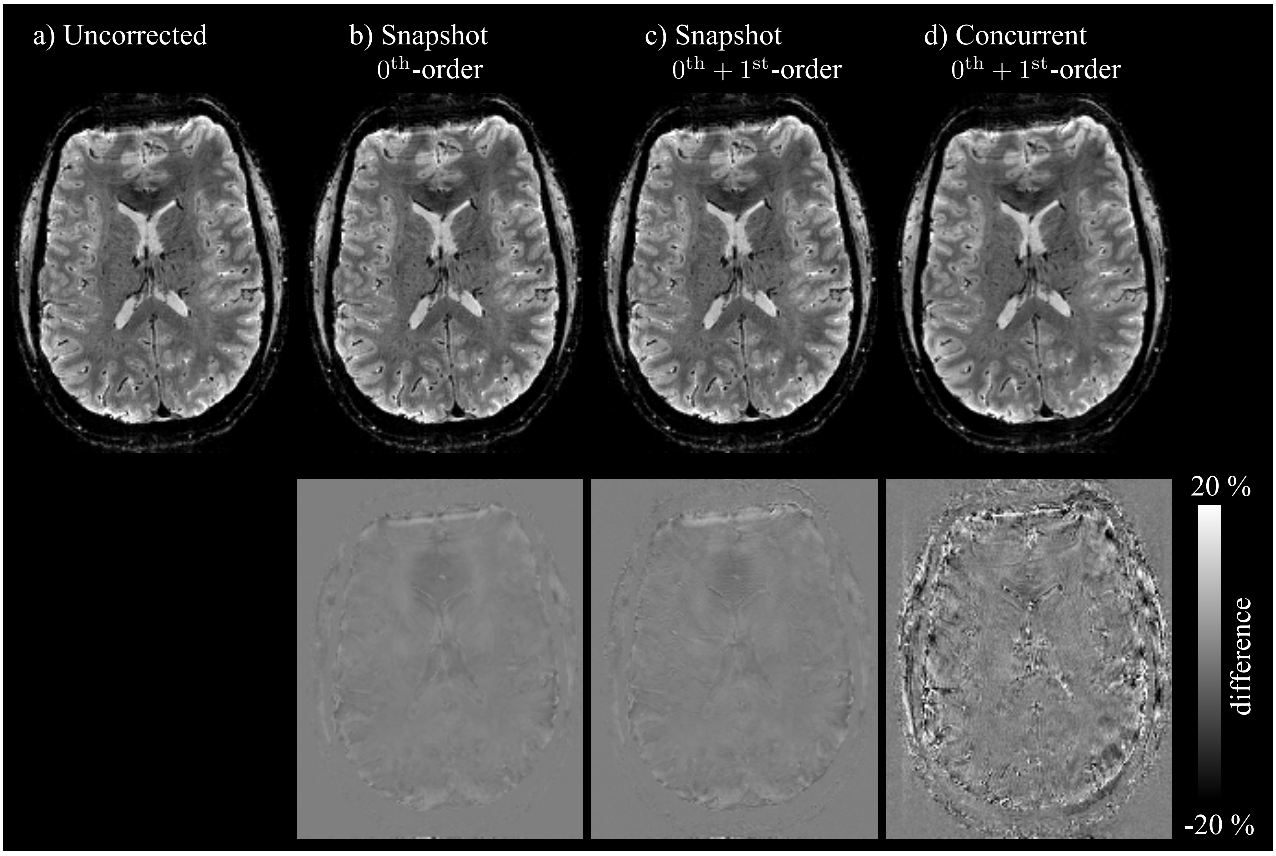

Figure 4.16: The effect of the different field correction methods for the normal breathing experiment performed with protocol B. Axial example slices of the a) uncorrected reference image and b)-d) the field corrected images. Difference images between the uncorrected image and the field corrected images are shown on the bottom.

To examine the effect of the order of field correction and compare snapshot and concurrent field monitoring, tSRN maps were determined and evaluated for all 5 experiments. Exemplary, tSNR maps for the hand-to-chin experiment acquired with protocol A are shown in Figure 4.13. In addition to the gain in image quality, field correction clearly improved the temporal SNR, especially in the anterior part of the brain which was strongly affected by field perturbations. Whole brain cumulated tSNR histograms are displayed in Figure 4.17 for the experiments performed with protocol A and in Figure 4.18 for protocol B. The tSNR distribution is shown for reconstructions without field correction, and reconstructions employing 0^{th}-order snapshot, 0^{th}- and 1^{st}-order snapshot, 0^{th}-order concurrent and 0^{th}- and 1^{st}-order concurrent field correction.

For protocol A, the whole-brain tSNR maps were determined based on the 6 volume repetitions. For both tasks, field correction led to a significant improvement in tSNR. Furthermore, 0^{th}- and 1^{st}-order field correction increased the tSNR compared to only 0^{th}-order correction. For the hand-to-chin experiment, the tSNR median improved compared to the uncorrected data by $50\,\%$ for 0^{th}-order field correction using the concurrent field monitoring approach and by $74\,\%$ for 0^{th}- and 1^{st}-order correction. For the snapshot method, the median increased by 46 % and 70 %, respectively. For the deep breathing experiment, the tSNR increased by 32 % and 37 % for the concurrent and by 36 % and 39 % for the snapshot approach.

For the accelerated protocol B, whole-brain tSNR maps were calculated based on 14 volume repetitions. For the hand-to-chin experiment, a significant tSNR improvement due to field correction was observed, as for protocol A. Field correction with snapshot field monitoring achieved slightly better results than with concurrent field monitoring. In the normal breathing experiment, field correction based on concurrent field monitoring even resulted in a decrease in tSNR, while the snapshot method increased the tSNR. However, the 1^{st}-order snapshot field correction could not improve the 0^{th}-order corrected reconstruction. As a matter of fact, the 0^{th}- and 1^{st}-order snapshot correction was slightly worse than 0^{th}-order snapshot correction. In the deep breathing experiment measured with protocol B, the head motion was strong compared to the relatively small field fluctuations (see table 4.1) and thus, the datasets were subject to strong motion correction prior to tSNR calculation. However, a small improvement of the median tSNR can be observed using 0^{th}-order and 0^{th}- and 1^{st}-order field correction. Again, the 0^{th}- and 1^{st}-order correction was less effective. Notably, the 90 % tSNR percentile only improved with the 0^{th}-order snapshot or concurrent correction, although the differences are small.

a) Hand-to-chin experiment

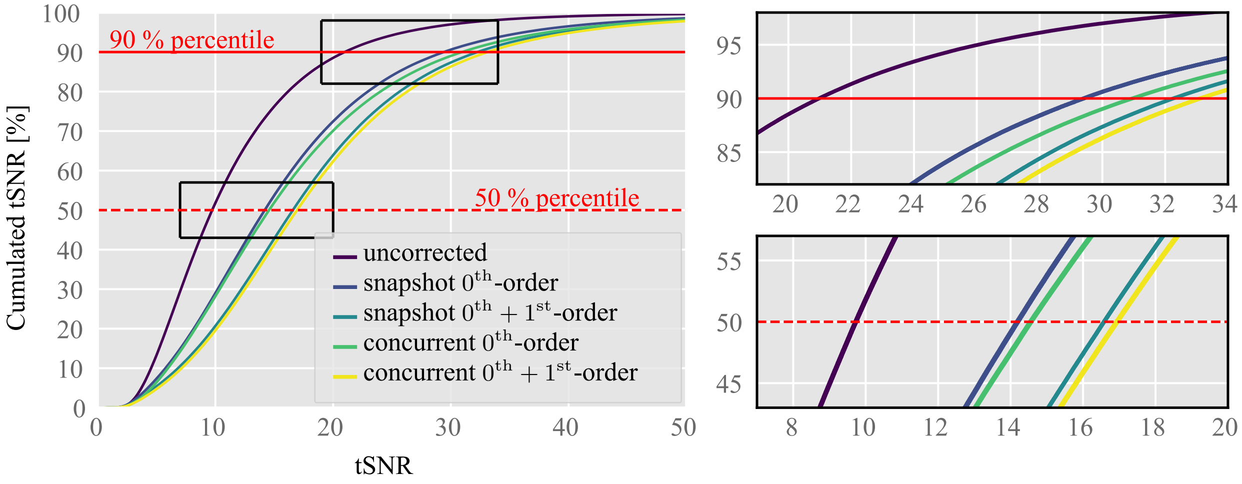

b) Deep breathing experiment

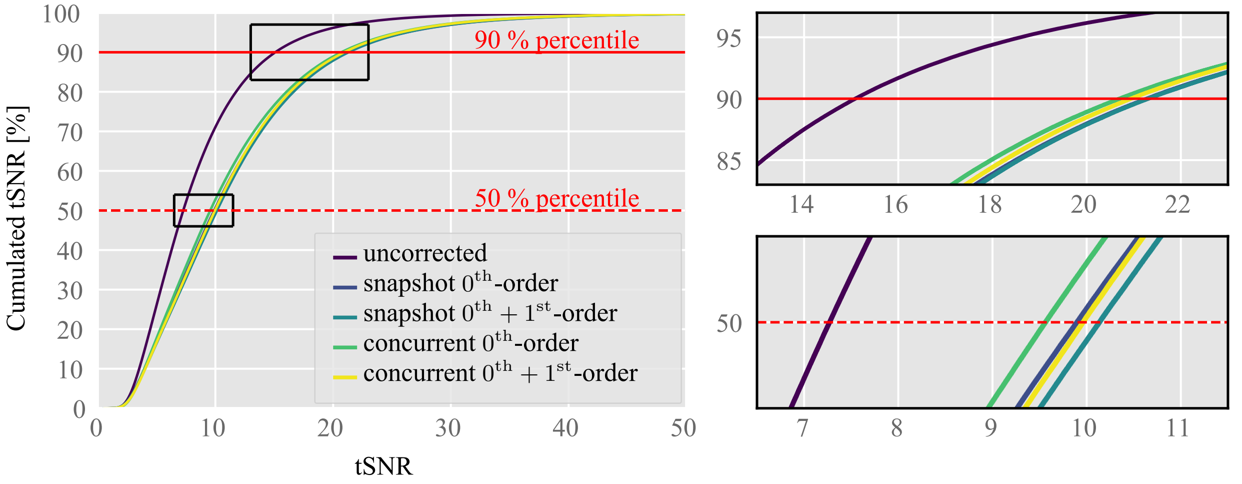

Figure 4.17: Effect of field correction on the cumulated tSRN of measurements performed with protocol A. Results are shown for a) the hand-to-chin movement and b) the deep breathing experiment. The tSRN was determined over the 6 repetitions of the time series.

a) Hand-to-chin experiment

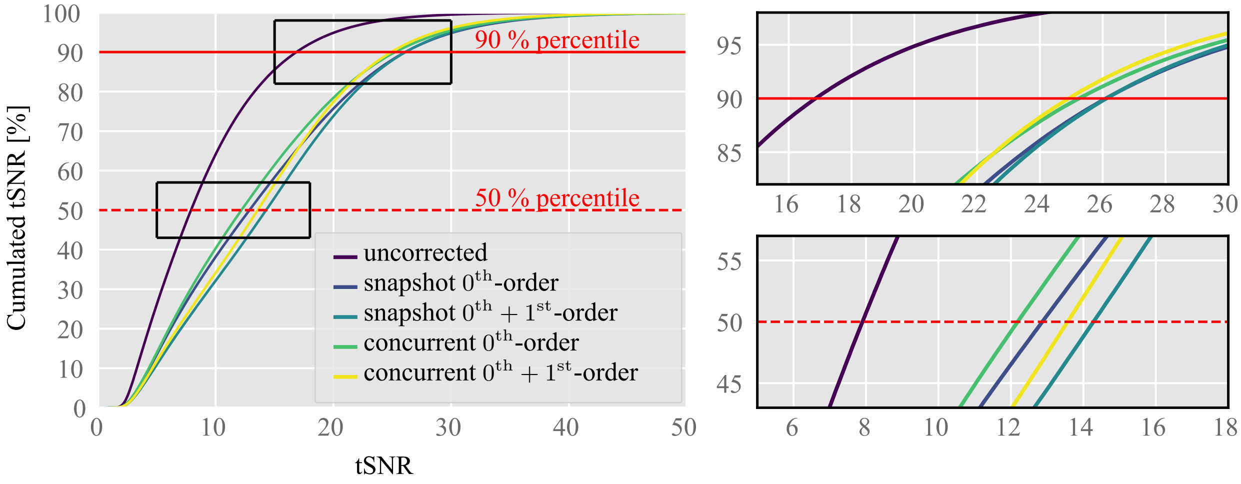

b) Deep breathing experiment

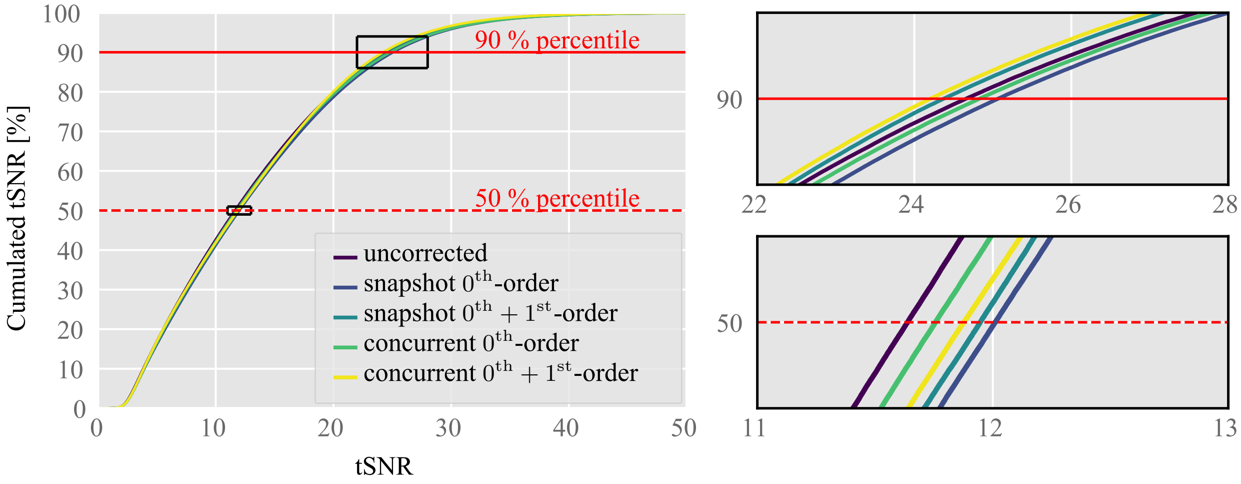

c) Normal breathing experiment

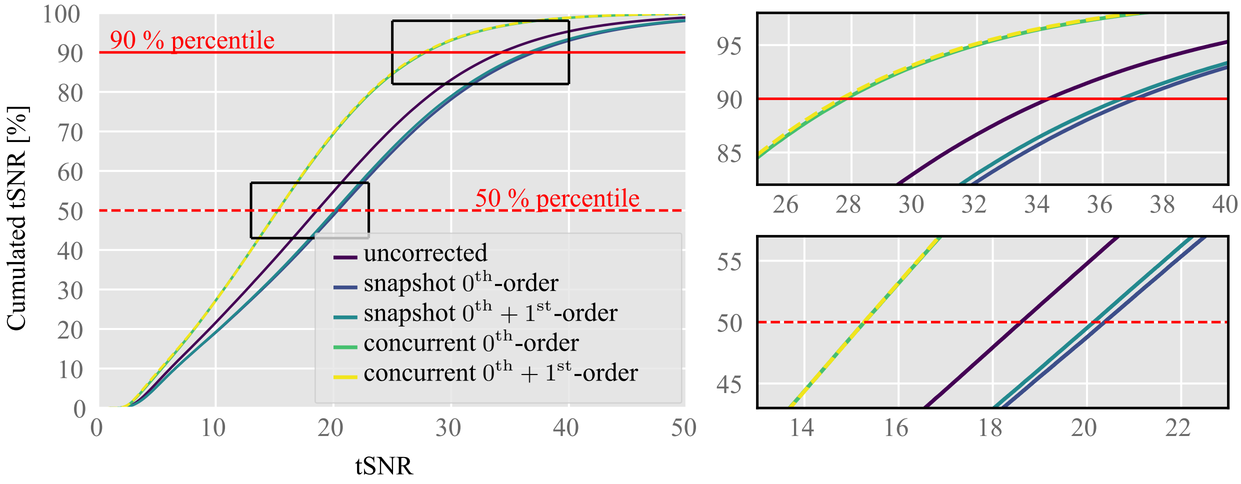

Figure 4.18: Effect of field correction on the cumulated tSRN of measurements performed with protocol B. Results are shown for a) the hand-to-chin movement, b) the deep breathing and c) the normal breathing experiment. The tSRN was determined over 14 (of the 15) volume repetitions. The first repetition was not considered due to transient signal effects

4.4 Discussion

In this project, physiological field fluctuations of up to 1^{st}- order were monitored during high-resolution T_2^* weighted 2D-segmented 3D-EPI acquisitions using NMR field probes. Physiological field changes were induced by instructing the subject to perform different tasks: repeating a movement of the hand from waist to chin or (deep) breathing. The induced field fluctuations had a mean frequency fluctuation of approximately $1 - 7\,\mathrm{Hz}$ and the first-order field changes led to mean k-space deviations of up to $0.2 \cdot \Delta k$ from the nominal EPI trajectory. Although bulk susceptibility changes through lung volume variations are large, the observed field fluctuations induced by respiration were generally smaller than by hand-to-chin movement, presumably because the chest moved less close to the imaging volume than the hand. Furthermore, the two subjects performed the tasks differently which led to field fluctuations of different intensity. While the hand-to-chin movement induced strong field fluctuations in all three directions, the dominating first-order field fluctuations for the deep breathing task were in the phase encoding direction, which corresponds to the main direction of the chest movement during deep breathing.

Two different magnetic field monitoring approaches, snapshot and concurrent field monitoring, were investigated. While concurrent field monitoring provides the complete field dynamics during the whole EPI echo train, including physiological field changes and imperfections of the gradient waveforms due to eddy currents, snapshot field monitoring is limited to relatively slow field changes, such as those due to physiology. The general behavior of the mean (mainly) motion-induced field fluctuations per readout has shown to be similar for both field monitoring approaches (cf. Figure 4.12). But the first-order k-space deviations in readout and phase encoding direction for concurrent field monitoring indicate, that especially the first (or the first two) readouts per EPI echo train experience stronger eddy currents compared to the other readouts. Snapshot field monitoring is limited to slow field changes and assumes a constant increase of the field fluctuations during the EPI echo train. However, the eddy-current-induced inconsistencies between even and odd echoes in readout direction are corrected by integrated phase correction using phase correction. Concurrent field monitoring eliminates the need for phase correction acquisitions since the complete k-space trajectory is monitored (cf. b)).

The MR scanner performs a zero-order eddy current compensation (ECC) during signal reception, which depends strongly on the sequence parameters and on the readout orientation (cf. Figure 4.9). To avoid correcting these B_0 variations twice, the ECC performed by the scanner had to be considered in the measured zero-order term for both field monitoring approaches. Since the ECC is independent of the subject, the measurements were performed once per protocol on a phantom.

Data were acquired using two different protocols, A and B, with similar sequence parameters. The main difference of the protocols was the time between consecutive excitation pulses which was relatively long for protocol A $TR_{shot} = 83.3\,\mathrm{ms}$) and minimal for protocol B ($TR_{shot} = 31.2\,\mathrm{ms}$).

It was shown, that images acquired during hand-to-chin movement (Figure 4.13 and 4.15) or deep breathing (Figure 4.14) were strongly affected by image artifacts appearing as intensity modulations, signal dropouts and blurring. The correction of field fluctuations achieved a considerable improvement in image quality for both field monitoring approaches. Due to the large field fluctuations induced during the movement of the hand from waist to chin, image artifacts were most severe in these experiments. Images acquired during normal breathing (Figure 4.16) did not show this kind of artifacts, and therefore the correction of field fluctuations did not achieved a visible improvement in image quality.

For protocol A, the long TR_{shot} allowed to monitor snapshot and concurrent field changes for every readout and the field correction yielded a large increase in image quality and tSNR. The tSNR gain of field correction were comparable for both field monitoring methods. However, imperfections in gradient waveforms due to eddy currents can be assumed similar in each volume repetition and accordingly, related artifacts can be expected to be static. Therefore, no significant tSNR change can be expected from the correction of eddy-current-induced field changes. To analyze the influence of eddy-current-induced gradient imperfections, another metric such as for example gradient entropy (McGee et al., 2000) is needed. But this analysis is beyond the scope of this project with focus on physiological field changes and need to be investigated in future studies.

Since fast successive excitation of the field probes can lead to spin echoes and stimulated echoes of previous excitations in the probe signal, snapshot and concurrent field data were monitored for only every 5^{th} echo train for acquisitions with protocol B.
For concurrent field monitoring, field deviations were interpolated for each time point of the EPI echo train. However, this interpolation implies the assumption that successively sampled echo trains experience the same eddy currents. The tSNR results (Figure 4.18c) for normal breathing clearly show, that experiments do not benefit from interpolated concurrent field monitoring if eddy currents between different lines and partitions are the dominating field changes. In this case, the interpolated concurrent field data were erroneous and the tSNR even decreased compared to the uncorrected data. In contrast, snapshot field monitoring only considered physiological field changes and the fitted field values determined from the long snapshot window of $3\,\mathrm{ms}$ were only little effected by eddy currents from the previous echo train. The field correction with the interpolated snapshot field data achieved a tSNR gain for all measurements, including the normal breathing experiment.

The results show, that strong field perturbations, such as those induced by deep breathing or a movement of the hand from waist to chin, lead to severe artifacts in the T_2^* weighted 3D-EPI images and image quality and tSNR strongly benefit from field correction. In this case, the 1^{st}-order field correction achieved further improvement. Due to the varying polarity of the readout gradients and the short blipped phase encoding gradients (cf. Figure 4.1), EPI sequences are prone to hardware-related gradient imperfections (Bollmann et al., 2017) which lead to deviations from the nominal trajectory (cf. Figure 4.4b)). The correction of up to the 1^{st}-order allowed to remove most artifacts in the high-resolution 3D-EPI acquisitions at 7 Tesla. These results are consistent with the work of Vannesjo et al. (Vannesjo et al., 2015) who investigated higher-order field correction of motion-induced field perturbation for T_2^* weighted 2D-GRE acquisitions at 7 Tesla. However, the TE and TR_{shot} of the 2D-GRE protocols were larger and therefore no interpolation of field monitoring data was required.

In general, the influence of physiological field fluctuations on the 1^{st}-order term is smaller than on the 0^{th}-order term and noise and eddy currents are therefore more prominent in the 1^{st}-order term. For high-resolution 3D-EPI acquisitions with small physiological field fluctuations, a snapshot field correction of only 0^{th}-order is sufficient or even beneficial if an interpolation of field probe data is necessary. For protocol A, which allows monitoring of every EPI train due to prolonged but less realistic timing, the benefit of 1^{st}-order concurrent and snapshot field correction for small field fluctuations was not investigated.

However, the $(1\,\mathrm{mm})^3$ T_2^* weighted 3D-EPI experiment generally achieved a good image quality with high tSNR for the normal breathing task. In this case, a field correction is not necessarily required. Triantafyllou et al. (Triantafyllou et al., 2005) showed that at higher field strength, the physiological to thermal noise ratio for 2D gradient echo EPI acquisitions has a steeper decline with voxel volume than at lower field strength. It can thus be expected, that 3D-EPI acquisition with lower spatial resolution are more effected by physiological noise. Furthermore, to achieve a good T_2^* contrast, Peters et al. (Peters et al., 2007) suggested to chose the TE of the sequence equal to the average T_2^* of white matter, which is approximately $27\,\mathrm{ms}$ at $7\,\mathrm{T}$. Increasing TE of the 3D-EPI sequence from $19\,\mathrm{ms}$ to $27\,\mathrm{ms}$ would certainly increase the effect of physiological field fluctuations, and thus the effect of field correction. In general, field monitoring is expected to be particularly useful in patients who breathe deeply and irregularly and who have difficulties lying still, that has been observed in patients with neurodegenerative diseases (Versluis et al., 2010).

Various methods, such as navigator-based MRI techniques (Hu and Kim, 1994; Pfeuffer et al., 2002; Versluis et al., 2010) or the use of a respiration belt (Van Gelderen et al., 2007) have been proposed to determine (physiologically) induced field fluctuations. Alternatively, field monitoring systems based on ^{19}F NMR field probes (De Zanche et al., 2008) have been applied to measure hardware- and physiology-related field changes for spiral (Engel et al., 2018; Kasper et al., 2018), 2D-GRE (Vannesjo et al., 2015) and 2D-EPI acquisitions (Bollmann et al., 2017; Hennel et al., 2020; Wilm et al., 2011, 2015). Wezel et al. (Wezel et al., 2017) compared navigator-based and snapshot field monitoring B_0 correction of T_2^* weighted multislice GRE acquisitions at 7T and achieved comparable results.

In this work, NMR field probes were used to monitor physiological field fluctuations in 3D-EPI acquisitions. The determination of higher-order field dynamics from the field probe signals have shown to be extremely sensitive to the positioning of the field probes. Positions that achieve optimal conditioning for expansion into a 3^{rd}-order spherical harmonic field model were proposed for different head coil architectures (Engel et al., 2018; Wilm et al., 2015). Zones of enhanced electrical

interaction (strip lines of the birdcage transmit coil and the end-ring-zones of the tuning capacitor) can lead to eddy currents in the signal of individual probes limit the probe positioning. For the 1Tx/32Rx Nova head coil of the 7T Siemens scanner, the narrow space between the transmit and the receive part further limits the probe positioning (cf. Figure 4.10). Taking into account all these limitations, the positioning was conditioned for the best approximation to the field dynamics and a field probe holder was developed (Brunheim et al., 2020). The prototype of the upper frame of the probe holder was used for all experiments. However, manual fixation of the bottom probes led to small deviations from the optimal position and certainly had an influence on the measured magnetic fields. Furthermore, the probe positioning was conditioned for 16 field probes, but due to a defective probe, only 15 field probes were used for the field measurements. Leaving out one more field probe showed a clear effect on the concurrent estimation of field dynamics and the reconstructed images (cf. Figure 6.3). It has to be further investigated whether the results change when using all 16 field probes with a probe positioning on the final field probe holder.
For the field correction of up to 1^{st}-order, the field monitoring data was determined from the field probe signal using 1^{st}-order spherical harmonics fit. Substantially better results were achieved for concurrent field correction compared to using a 2^{nd}-order fit (cf. Figure 6.4). These results differ from the findings of (Vannesjo et al., 2015) for T_2^* weighted 2D-GRE acquisitions at 7 Tesla.

Since snapshot field monitoring only captures slow field dynamics during a gradient-free time window, it is less sensitive to the probe positioning or the order of fitting. However, eddy currents from previous echo trains influence the snapshot field values and are then misinterpreted as slow field dynamics and assumed constant throughout the whole EPI echo train. To minimize the effect of eddy currents by averaging them out, a snapshot window of $3\,\mathrm{ms}$ was used for all experiments.
A strong influence of eddy currents in the snapshot window has been observed when employing a method called echo time shifting (ETS) [Feinberg1994]. Thereby, ghosting artifacts in the EPI images are reduced by varying EPI readout start time of successive EPI segments such that the phase evolution in k-space is more continuous. This led to varying eddy currents across shots in the snapshot window, which worsened the correction of physiological field fluctuations. Furthermore, ETS does not allow an accurate interpolation of concurrent field data. Due to these limitations, all measurements were acquired without ETS.

4.5 Conclusion

Using NMR field probes, physiological field fluctuations were monitored during high-resolution T_2^* weighted 2D-segmented 3D-EPI acquisitions. A non-iterative field correction up to 1^{st}-order was implemented for snapshot and concurrent field monitoring and included into the in-house developed reconstruction toolbox. The ECC performed by the scanner during signal reception was considered in the measured 0^{th}- order field term.

Image quality and tSNR of the 3D-EPI acquisitions that were subject to severe physiological noise strongly benefit from field correction based on both, snapshot and concurrent field monitoring. The results of this work indicate, that snapshot field monitoring is the preferable method for acquisitions with short TR_{shot}, where an interpolation of the field monitored data is required. However, the method does not allow for correction of eddy-current-induced field changes and require the standard phase correction scans and a gradient-free snapshot window. If the acquisition is not limited by signal decay and the repetition time is long enough to monitor every EPI echo train, concurrent field monitoring is the preferred method to capture and correct physiologically-induced and eddy-current-induced field fluctuations. Full concurrent field monitoring is more flexible with respect to the echo time of the sequence, as it allows ETS and does not require phase correction scans and a gradient-free time window.

With ‘normal’ physiological field fluctuations, the segmented 3D-EPI acquisitions with the chosen sequence parameters generally achieved good image quality with high tSNR. Routinely field correction is probably only necessary with older patients or small children that have difficulties lying still. However, a larger effect of physiological noise on 3D-EPI acquisitions at 7T is expected for applications with lower spatial resolution or longer TE.

5

Conclusion and Outlook

The usage of magnetic resonance imaging for a wide range of applications requires the acquisition of high-quality images in short scan times. This is a challenging problem and still one of the main research topics in MRI. One recent step in this direction is the introduction of the first clinical 7 Tesla scanners. The high SNR obtained by higher field strength allows for higher parallel imaging accelerations. In this context, achieving high acceleration factors at good image quality relies, among others, on the parallel imaging sampling pattern and on a robust image reconstruction. In the scope of this work, a Python toolbox for a parallel imaging reconstruction based on the GRAPPA algorithm was developed. Using a three-dimensional reconstruction kernel and Tikhonov regularization, Cartesian data is reconstructed robustly.

The aim of the first part of this thesis was to extend the reconstruction to non-Cartesian wave-CAIPI data. The developed GRAPPA-based wave-CAIPI reconstruction is fast and robust and, compared to the recently proposed SENSE-type reconstruction, it is a non-iterative method that does not depend on the accuracy of specific coil sensitivity estimations and mask regions. A system of NMR field probes was used to determine the exact trajectories required for successful and artifact-free reconstructions of the non-Cartesian data.
To validate the GRAPPA-based wave-CAIPI reconstruction, wave-CAIPI sampling was incorporated into two widely-used fast 3D sequences: a T_1 weighted gradient echo sequence (MP-RAGE) and a T_2 weighted spin echo sequence (TSE). It has been shown, that both sequences allow ultra-fast high-resolution wave-CAIPI imaging with reduced g-factor penalties and improved image quality compared to conventional 2D CAIPIRINHA. 16-fold accelerated whole brain MP-RAGE and TSE data with $1\,\mathrm{mm}$ isotropic resolution were acquired in only 40 seconds and 1:32 minutes, respectively. This is about 5-8 times faster than usual.

However, it has been observed that the sinusoidal phase encoding gradients of wave-sampling induce eddy currents, which lead to additional gradient moments. This is problematic for the TSE sequence, where the magnetization is refocused using RF pulses during the echo trains. However, image artifacts caused by improper momentum rephasing could be successfully prevented by the application of correcting rephasing gradients. These gradients were empirically determined with k-space trajectory measurements using the field probe system.

The NRM field probes were furthermore used during in-vivo measurements to account for subject-induced field and trajectory deviations in the image reconstruction. Physiological field fluctuations of up to first order spatial expansion were monitored during high-resolution T_2^* weighted segmented 3D-EPI acquisitions at 7 Tesla. It was shown that field changes induced by (deep) breathing or limb movements lead to artifacts in the reconstructed images. Especially for strong field distortions, the image quality and the tSNR strongly benefit from a field correction. Two different field monitoring approaches, snapshot and concurrent field monitoring, were investigated. Both methods are, among others, limited by the time between successive NMR field probe excitations. As a consequence, not every echo train can be monitored for fast 3D-EPI acquisitions and missing field probe data must be interpolated. Concurrent field monitoring allows to capture physiologically-induced and eddy-current-induced field fluctuations and has proven to be the preferable method if the acquisition is not limited by signal decay and if the repetition time is long enough to monitor every EPI echo train. However, most fast 3D acquisitions require an interpolation of the field monitored data. In this case, the correction of physiological field fluctuations is more reliable using snapshot field monitoring.
A zero- and first-order field correction was incorporated into the reconstruction toolbox. Field fluctuations of first-order lead to shifts of sampling points away from the nominal trajectory. Shifting of sampling points back to the Cartesian grid is achieved by GRAPPA operator gridding (GROG). This GRAPPA-based parallel imaging concept has shown to be well-suited for the small k-space shifts induced by physiological field changes. Furthermore, the eddy current compensation (ECC) performed by the scanner during signal reception was considered in the measured zero-order field term. For its determination, a separate method based on phantom scans was developed for each of the two field monitoring approaches.
It has been shown that with field correction of up to first-order, a high image quality can be regained for acquisitions that were subject to strong physiological field fluctuations. For some patient groups, such as small children or elderly people who have difficulties lying still, a routinely performed field correction could therefore be advantageous. However, to ensure correct and reproducible field measurements, this also requires the completion of the 3D-printed NMR field probe holder that was developed in close collaboration throughout this work.

To conclude, the GRAPPA-based reconstruction presented in this thesis provides a fast, robust and non-iterative reconstruction of Cartesian and wave-CAIPI parallel imaging acquisitions for highly accelerated acquisitions. Furthermore, the correction of physiological field changes measured with NMR field probes is incorporated into the reconstruction process and allows for a significant improvement of images acquired in the presence of strong field fluctuations. In further steps, integration of the reconstruction into the scanner's workflow by means of the Gadgetron software (Hansen and Sørensen, 2013) is envisaged, thus, making GRAPPA-based wave-CAIPI imaging and physiological field correction available for routine neuroimaging applications. Furthermore, to gain more flexibility for wave-CAIPI acquisitions, the gradient impulse function (GIRF) (Signe J. Vannesjo, Maximilan Haeberlin, et al., 2013) can be measured using the NRM field probe system. Its knowledge allows to predict gradient shapes and facilitates the determination of the correcting rephasing gradients required for multiecho spin echo protocols. Besides, it might eliminate the need of corkscrew trajectory measurements for each wave-CAIPI protocol. In addition, the effect of physiological noise and thus the benefit of the field correction on other 3D-EPI acquisitions at 7 Tesla must be investigated in future studies. The benefit is expected to be more prominent for applications with lower spatial resolution or longer TE, such as for example T_2^* mapping and functional MRI. However, the interpolation of data monitored during fast 3D-EPI acquisitions with echo time shifting (ETS) still remains a challenging problem.

6

Appendix

6.1 Supplementary Material of Chapter 3

6.1.1 Automatic Subcortical Segmentation

Figure 6.1 depicts examples of the subcortical segmentation achieved within FreeSurfer's longitudinal processing stream (Reuter et al., 2012) for retrospectively accelerated Cartesian and wave-CAIPI data. Visual inspection shows that the segmentation worked well in all cases and no clear difference is visible between the different sampling schemes and accelerations. However, the quantitative comparison based on the DICE coefficient indicates a clear improvement of the segmentation of the different brain regions using wave-CAIPI instead of Cartesian CAIPIRINHA. The results are discussed in Section 3.4.3.2.

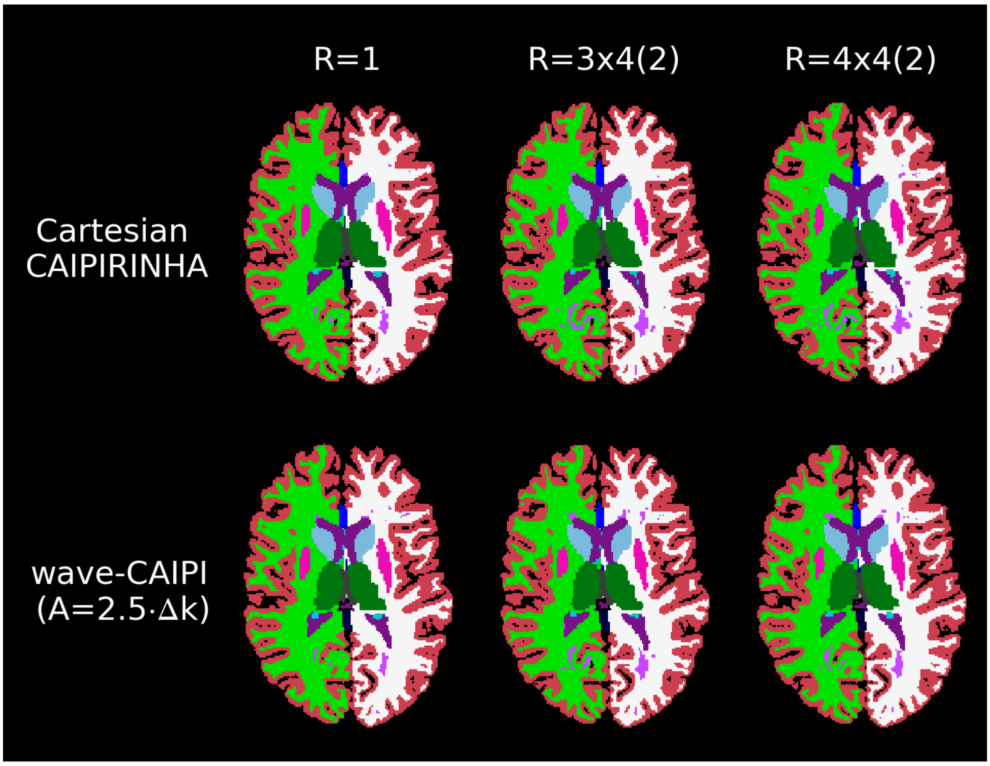

Figure 6.1: Axial view of the automatic subcortical segmentation achieved within FreeSurfer's longitudinal processing stream. The results are shown for one of the subjects using Cartesian CAIPIRINHA and wave-CAIPI sampling with different acceleration factors.

6.1.2 Mask Region for SENSE Reconstruction

SENSE reconstructions require high-quality sensitivity maps and mask regions, estimated from the calibration data. Utilizing the BART toolbox (Uecker et al.) for their estimations allows to produce high-quality SENSE reconstructed wave-CAIPI images. However, the default mask computed by the toolbox is too small. The effect of different mask sizes on the reconstructed images and on the RMSE with regard to the fully sampled data is show in Figure 6.2.

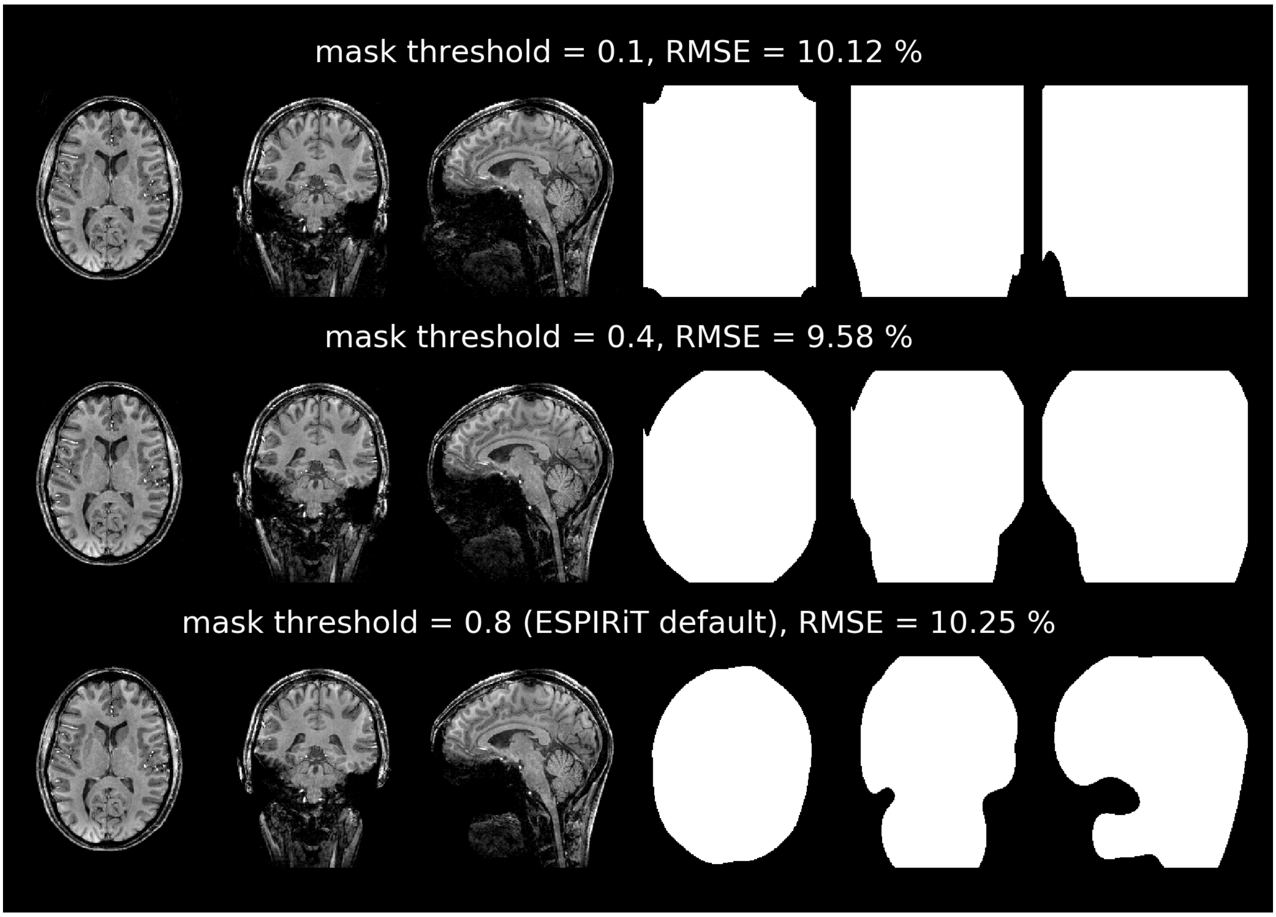

Figure 6.2: SENSE-type wave-CAIPI reconstruction of retrospectively 16-fold accelerated wave-CAIPI acquisition. Different ESPIRiT thresholds were used for the computation of different sizes of sensitivity masks (right). The RMSE with regard to the fully sampled data was calculated in the brain region for all three reconstructions. The default mask (threshold $= 0.8$) computed with the ESPIRiT algorithm crops out the mouth and nasal cavity region and thereby, the reconstruction slightly falls of in quality. The smallest RMSE was found for the threshold 0.4, however, the results are very similar.

6.2 Supplementary Material of Chapter 4

6.2.1 Effect of Missing Field Probes

All magnetic field measurements of Chapter 4 were performed using NMR field probes placed on the upper frame of a prototype field probe holder (Brunheim et al., 2020) and fixing the probes of the bottom frame with tape at approximately the designed positions. The probe positioning of the 16 NMR field probes schematically shown in Figure 4.10 was conditioned for the best approximation to the field dynamics, taking into account the limitations of the coil architecture. Due to the defective field probe number 3, only 15 probes were used for the determination of the field dynamics of up to 1^{st}-order. Since the probe positioning was conditioned for 16 and not 15 field probes, the missing field probe certainly had an impact on the field monitoring data fitted from the probe signals and thus on the field correction.

To investigate the influence of a missing field probe on the measured field dynamics and on the resulting field corrected image, a $(1\,\mathrm{mm})^3$ in vivo EPI measurement was carried out without any intentionally induced field perturbations. Hardware-related concurrent field dynamics were measured on a phantom using the same sequence parameters as for the in-vivo measurement. Field deviations and the field corrected images are shown for field data processed for all 15 working field probes (Figure 6.3a) and for only 14 field probes (Figure 6.3b). In Figure 6.3b, the signal of probe number 13 (cf. Figure 4.10) was omitted for the fitting of the magnetic fields. A clear influence can be observed on the relative k-space deviation $\frac{\delta k_{p2}}{\Delta k_{p2}}$ in partition direction (z-direction) and the impact on the reconstructed image is visible in the difference image.

a) all 15 available field probes

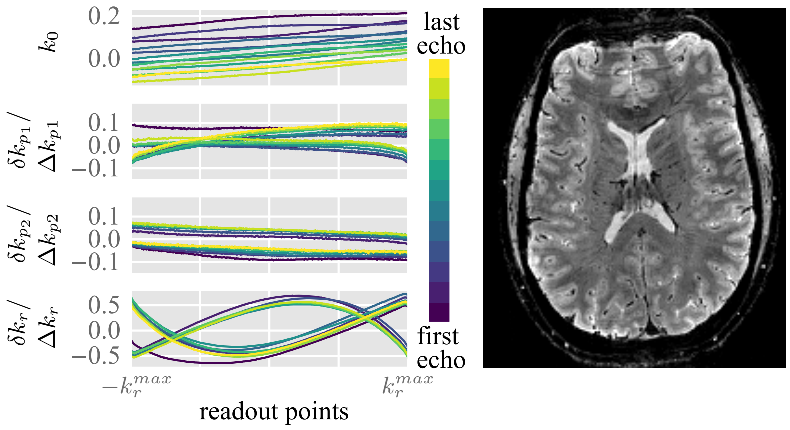

b) only 14 field probes

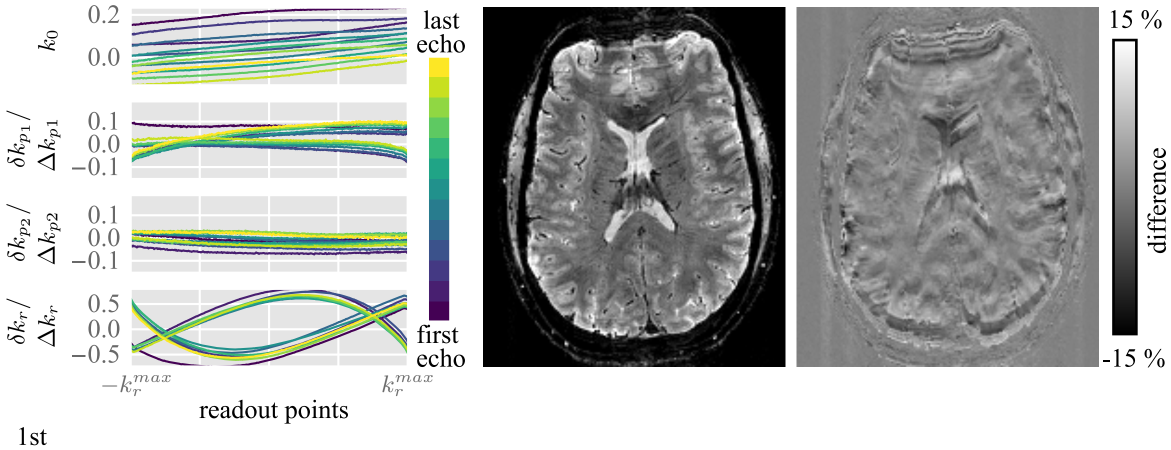

1st

Figure 6.3: Left: 0^{th}- and 1^{st}-order field deviations of one EPI echo train acquired with concurrent field monitoring during a phantom measurement. Field probe data were processed for a) all 15 working field probes of Figure 4.10 by fitting spherical harmonic spatial basic functions of 1^{st}-order and b) using only 14 field probes. The signal of probe number 13 in Figure 4.10 was omitted for the fitting of the magnetic fields. Middle: Reconstructed images for a normal breathing experiment reconstructed with the 0^{th}- and 1^{st}-order phantom concurrent field data. The image quality in b) is slightly reduced compared to a). Right: Difference images between a) and b) scaled relative to the maximum displayed value.

6.2.2 Order of the Spherical Harmonics Fit

Using 16 NMR field probes allow a monitoring of up to 3^{rd}-order field dynamics. In Chapter 4, only up to 1^{st}-order fields fluctuations were corrected. The temporal evolution of the spatial distribution of magnetic field perturbations was determined by fitting spherical harmonics of up to 1^{st}-order to each time point. Vannesjo et al. (Vannesjo et al., 2015) investigated higher-order field correction and achieved better results for up to 1^{st}-order field correction using a higher-order model (2^{nd}-order fit) than using a 1^{st}-order fit.

However, we observed substantially better results using a 1st-order fit for field corrections of 0th- and for a 1st-order. Field deviations and the corresponding reconstructions are shown for a 1st-order field model in Figure 6.4a and a 2nd-order field model in Figure 6.4b. The in vivo dataset and phantom field measurements were the same as in Section 6.2.1. A clear difference in the relative k-space shifts can be observed in phase and partition encoding direction ($p1$ and $p2$) and using the 2nd-order model results in visible image artifacts.

a) 1st-order fit, up to 1st-order field correction

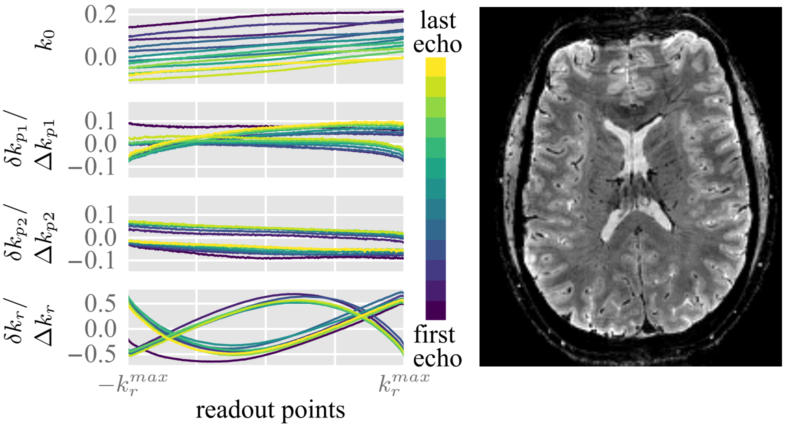

b) 2nd-order fit, up to 1st-order field correction

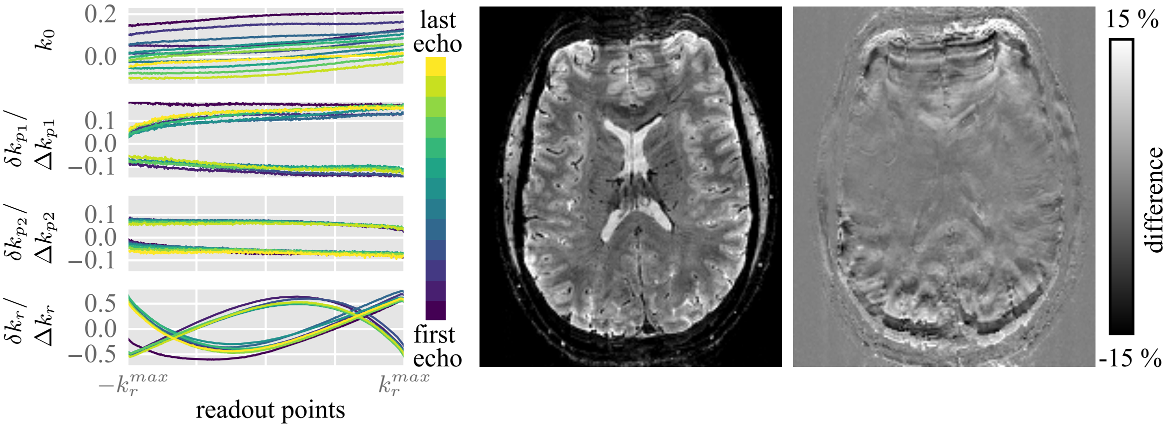

Figure 6.4: Left: 0th- and 1st-order field deviations of one EPI echo train acquired with concurrent field monitoring during a phantom measurement. Field probe data were processed for a) all 15 working field probes of Figure 4.10 by fitting spherical harmonic spatial basic functions of 1st-order and b) using a spherical harmonic fit of 2nd-order. Middle: Reconstructed images for a normal breathing experiment reconstructed with the 0th- and 1st-order phantom concurrent field data. The image quality in b) is reduced compared to a). Right: Difference images between a) and b) scaled relative to the maximum displayed value.

This can be understood, if the field probe fitting coefficients are taken as the results of a Taylor expansion. The order of the expansion should match the order of the consequential correction applied. A simple 2nd-order polynomial example in Figure 6.5 clarifies this. The 1st-order polynomial fit provides the best linear approximation of the function, whereas the linear function using only 0^{th}- and 1^{st}-order terms of the 2^{nd}-order polynomial fit shows a large deviation from the original function across the observed range.

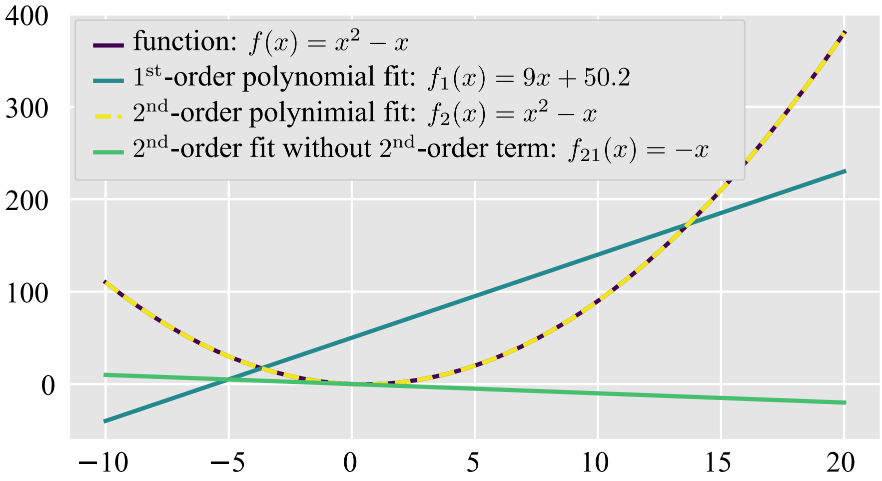

Figure 6.5: Representation of a simple 2^{nd}-order polynomial function $f(x) = x^2 - x; x \in \{-10, 20\}$. The 1^{st}-order polynomial fit provides the best linear approximation of the function, whereas using only the 0^{th}- and 1^{st}-order terms of the 2^{nd}-order polynomial fit does not represent a good linear approximation.

References

Ahn CB, Kim JH, Cho ZH, 1986. High-Speed Spiral-Scan Echo Planar NMR Imaging-I. IEEE Transactions on Medical Imaging 5, 2–7.

Barmet C, De Zanche N, Pruessmann KP, 2008. Spatiotemporal magnetic field monitoring for MR. Magnetic Resonance in Medicine 60, 187–197.

Barmet C, De Zanche N, Wilm BJ, Pruessmann KP, 2009. A transmit/receive system for magnetic field monitoring of in vivo MRI. Magnetic Resonance in Medicine 62, 269–276.

Bauer S, Markl M, Honal M, Jung BA, 2011. The effect of reconstruction and acquisition parameters for GRAPPA-based parallel imaging on the image quality. Magnetic Resonance in Medicine 66, 402–409.

Bernstein MA, Fain SB, Riederer SJ, 2001. Effect of windowing and zero-filled reconstruction of MRI data on spatial resolution and acquisition strategy. Journal of Magnetic Resonance Imaging 14, 270–280.

Bilgic B, Gagoski BA, Cauley SF, Fan AP, Polimeni JR, Grant PE, Wald LL, Setsompop K, 2015. Wave-CAIPI for Highly Accelerated 3D Imaging. Magnetic Resonance in Medicine 73, 2152–2162.

Blaimer M, Breuer FA, Mueller M, Seiberlich N, Ebel D, Heidemann RM, Griswold MA, Jakob PM, 2006. 2D-GRAPPA-operator for faster 3D parallel MRI. Magnetic Resonance in Medicine 56, 1359–1364.

Blaimer M, Breuer F, Mueller M, Heidemann RM, Griswold MA, Jakob PM, 2004. SMASH, SENSE, PILS, GRAPPA. Topics in Magnetic Resonance Imaging 15, 223–236.

Blaimer M, Gutberlet M, Kellman P, Breuer FA, Köstler H, Griswold MA, 2009. Virtual coil concept for improved parallel MRI employing conjugate symmetric signals. Magnetic Resonance in Medicine 61, 93–102.

Bloch F, 1946. Nuclear induction. Physical Review 70, 460–474.

Boesch C, Gruetter R, Martin E, 1991. Temporal and spatial analysis of fields generated by eddy currents in superconducting magnets: Optimization of corrections and quantitative characterization of magnet/gradient systems. Magnetic Resonance in Medicine 20, 268–284.

Bollmann S, Kasper L, Vannesjo SJ, Diaconescu AO, Dietrich BE, Gross S, Stephan KE, Pruessmann KP, 2017. Analysis and correction of field fluctuations in fMRI data using field monitoring. NeuroImage 154, 92–105.

Brenner D, Stirnberg R, Pracht ED, Stöcker T, 2014. Two-dimensional accelerated MP-RAGE imaging with flexible linear reordering. Magnetic Resonance Materials in Physics, Biology and Medicine 27, 455–462.

Breuer FA, Blaimer M, Heidemann RM, Mueller MF, Griswold MA, Jakob PM, 2005. Controlled aliasing in parallel imaging results in higher acceleration (CAIPIRINHA) for multi-slice imaging. Magnetic Resonance in Medicine 53, 684–691.

Breuer FA, Blaimer M, Mueller MF, Seiberlich N, Heidemann RM, Griswold MA, Jakob PM, 2006. Controlled aliasing in volumetric parallel imaging (2D CAIPIRINHA). Magnetic Resonance in Medicine 55, 549–56.

Breuer FA, Kannengiesser SAR, Blaimer M, Seiberlich N, Jakob PM, Griswold M a, 2009. General formulation for quantitative G-factor calculation in GRAPPA reconstructions. Magnetic Resonance in Medicine 62, 739–46.

Breuer FA, Moriguchi H, Seiberlich N, Blaimer M, Jakob PM, Duerk JL, Griswold MA, 2008. Zigzag sampling for improved parallel imaging. Magnetic Resonance in Medicine 60, 474–478.

Brunheim S, Mirkes C, Dietrich B, Schwarz JM, Stirnberg R, Ismar S, Alexander C, Barmet C, Stöcker T, 2020. Replaceable field probe holder for the Nova coil on a 7 Tesla Siemens scanner, in: Proceedings of the 28th Scientific Meeting of the International Society for Magnetic Resonance in Medicine.

Buehrer M, Pruessmann KP, Boesiger P, Kozerke S, 2007. Array compression for MRI with large coil arrays. Magnetic Resonance in Medicine 57, 1131–1139.

Buonocore MH, Gao L, 1997. Ghost artifact reduction for echo planar imaging using image phase correction. Magnetic Resonance in Medicine 38, 89–100.

Busse RF, Brau ACS, Vu A, Michelich CR, Bayram E, Kijowski R, Reeder SB, Rowley HA, 2008. Effects of refocusing flip angle modulation and view ordering in 3D fast spin echo. Magnetic Resonance in Medicine 60, 640–649.

Butts K, Riederer SJ, Ehman RL, Thompson RM, Jack CR, 1994. Interleaved echo planar imaging on a standard MRI system. Magnetic Resonance in Medicine 31, 67–72.

Cauley SF, Setsompop K, Bilgic B, Bhat H, Gagoski B, Wald LL, 2016. Autocalibrated wave-CAIPI reconstruction; Joint optimization of k-space trajectory and parallel imaging reconstruction. Magnetic Resonance in Medicine 78, 1093–1099.

Chavhan GB, Babyn PS, Thomas B, Shroff MM, Mark Haacke E, 2009. Principles, techniques, and applications of T2*-based MR imaging and its special applications. Radiographics 29, 1433–1449.

Crozier S, Eccles CD, Beckey FA, Field J, Doddrell DM, 1992. Correction of eddy-current-induced B0 shifts by receiver reference-phase modulation. Journal of Magnetic Resonance 97, 661–665.

De Zanche N, Barmet C, Nordmeyer-Massner Ja, Pruessmann KP, 2008. NMR Probes for measuring magnetic fields and field dynamics in MR systems. Magnetic Resonance in Medicine 60, 176–186.

Duyn JH, Yang Y, Frank JA, Veen J van der, 1998. Simple Correction Method for k-Space Trajectory Deviations in MRI. Journal of Magnetic Resonance 153, 150–153.

Engel M, Kasper L, Barmet C, Schmid T, Vionnet L, Wilm B, Pruessmann KP, 2018. Single-shot spiral imaging at 7 T. Magnetic Resonance in Medicine 80, 1836–1846.

Feiweier T, 2010. Magnetic Resonance Imaging Data Acquisition Sequence and Apparatus.

Fischl B, Salat DH, Busa E, Albert M, Dieterich M, Haselgrove C, Kouwe A van der, Killiany R, Kennedy D, Klaveness S, Montillo A, Makris N, Rosen B, Dale AM, 2002. Whole Brain Segmentation: Neurotechnique Automated Labeling of NeuroanatomicalStructures in the Human Brain. Neurotechnique 33, 341–355.

Foester BU, Dardo T, Elisabeth, 2014. Magnetic Field Shift due to Mechanical Vibration in Functional Magnetic Resonance Imaging. Magnetic Resonance in Medicine 54, 1261–1267.

Gagoski BA, Bilgic B, Eichner C, Bhat H, Grant PE, Wald LL, Setsompop K, 2015. RARE/Turbo Spin Echo imaging with Simultaneous MultiSlice Wave-CAIPI. Magnetic Resonance in Medicine 73, 929–938.

Greve DN, Fischl B, 2009. Accurate and robust brain image alignment using boundary-based registration. NeuroImage 48, 63–72.

Griswold MA, Blaimer M, Breuer F, Heidemann RM, Mueller M, Jakob PM, 2005. Parallel magnetic resonance imaging using the GRAPPA operator formalism. Magnetic Resonance in Medicine 54, 1553–1556.

Griswold MA, Heidemann RM, Jakob PM, 2003. Direct Parallel Imaging Reconstruction of Radially Sampled Data Using GRAPPA with Relative Shifts M., in: Proceedings of the 11th Scientific Meeting of the International Society for Magnetic Resonance in Medicine. p. 2349.

Griswold Ma, Jakob PM, Heidemann RM, Nittka M, Jellus V, Wang J, Kiefer B, Haase A, 2002. Generalized autocalibrating partially parallel acquisitions (GRAPPA). Magnetic Resonance in Medicine 47, 1202–1210.

Griswold MA, Jakob PM, Nittka M, Goldfarb JW, Haase A, 2000. Partially Parallel Imaging With Localized Sensitivities (PILS). Magnetic Resonance in Medicine 44, 602–609.

Haase A, Frahm J, Matthaei D, Hanicke W, Merboldt KD, 1986. FLASH imaging. Rapid NMR imaging using low flip-angle pulses. Journal of Magnetic Resonance 67, 258–266.

Han X, Fischl B, 2007. Atlas Renormalization for Improved Brain MR Image Segmentation Across Scanner Platforms. IEEE Transactions on Medical Imaging 26, 479–486.

Hansen MS, Sørensen TS, 2013. Gadgetron: An open source framework for medical image reconstruction. Magnetic Resonance in Medicine 69, 1768–1776.

Heidemann RM, Griswold MA, Haase A, Jakob PM, 2001. VD-AUTO-SMASH Imaging. Magnetic Resonance in Medicine 45, 1066–1074.

Heidemann RM, Griswold MA, Seiberlich N, Krüger G, Kannengiesser SA, Kiefer B, Wiggins G, Wald LL, Jakob PM, 2006. Direct parallel image reconstructions for spiral trajectories using GRAPPA. Magnetic Resonance in Medicine 56, 317–326.

Hennel F, Wilm B, Roesler MB, Weiger M, Dietrich B, Pruessmann KP, 2020. Echo-planar imaging of the human head with 100 mT/m gradients and high-order modeling of eddy current fields. Magnetic Resonance in Medicine 1–11.

Hennig J, 1988. Multiecho imaging sequences with low refocusing flip angles. Journal of Magnetic Resonance 78, 397–407.

Hennig J, Nauerth A, Friedburg H, 1986. RARE imaging: A fast imaging method for clinical MR. Magnetic Resonance in Medicine 3, 823–833.

Hennig J, Weigel M, Scheffler K, 2004. Calculation of Flip Angles for Echo Trains with Predefined Amplitudes with the Extended Phase Graph (EPG)-Algorithm: Principles and Applications to

Hyperecho and TRAPS Sequences. Magnetic Resonance in Medicine 51, 68–80.

Hore PJ, 1983. Solvent suppression in fourier transform nuclear magnetic resonance. Journal of Magnetic Resonance 55, 283–300.

Hu X, Kim S, 1994. Reduction of signal fluctuation in functional MRI using navigator echoes. Magnetic Resonance in Medicine 31, 495–503.

Huang F, Vijayakumar S, Li Y, Hertel S, Duensing GR, 2008. A software channel compression technique for faster reconstruction with many channels. Magnetic Resonance Imaging 26, 133–141.

Inati SJ, Naegele JD, Zwart NR, Roopchansingh V, Lizak MJ, Hansen DC, Liu CY, Atkinson D, Kellman P, Kozerke S, Xue H, Campbell-Washburn AE, Sørensen TS, Hansen MS, 2017. ISMRM Raw data format: A proposed standard for MRI raw datasets. Magnetic Resonance in Medicine 77, 411–421.

Ivanov D, Barth M, Uludag K, Poser BA, 2015. Robust ACS acquisition for 3D echo planar imaging, in: Proceedings of the 23th Scientific Meeting of the International Society for Magnetic Resonance in Medicine. p. 2059.

Jackson JI, Meyer CH, Nishimura DG, Macovski A, 1991. Selection of a convolution function for Fourier inversion using gridding. IEEE Transactions on Medical Imaging 10, 473–478.

Jakob PM, Grisowld MA, Edelman RR, Sodickson DK, 1998. AUTO-SMASH: A self-calibrating technique for SMASH imaging. Magnetic Resonance Materials in Physics, Biology, and Medicine 7, 42–54.

Jenkinson M, Bannister P, Brady M, Smith S, 2002. Improved optimization for the robust and accurate linear registration and motion correction of brain images. NeuroImage 17, 825–841.

Jenkinson M, Beckmann CF, Behrens TEJ, Woolrich MW, Smith SM, 2012. Review FSL. NeuroImage 62, 782–790.

Jenkinson M, Smith S, 2001. A global optimisation method for robust affine registration of brain images. Medical Image Analysis 5, 143–156.

Jezzard P, 2006. Shim Coil Design, Limitations and Implications. Abstracts from the International Society of Magnetic Resonance in Medicine.

Kasper L, Engel M, Barmet C, Haeberlin M, Wilm BJ, Dietrich BE, Schmid T, Gross S, Brunner DO, Stephan KE, Pruessmann KP, 2018. Rapid anatomical brain imaging using spiral acquisition and an expanded signal model. NeuroImage 168, 88–100.

Krüger G, Glover GH, 2001. Physiological Noise in Oxygenation-Sensitive Magnetic Resonance

Imaging. Magnetic Resonance in Medicine 46, 631–637.

Kyriakos WE, Panych LP, Kacher DF, Westin C-f, Bao SM, Mulkern RV, Jolesz FA, 2000. Sensitivity Profiles From an Array of Coils for Encoding and Reconstruction in Parallel (SPACE RIP). Magnetic Resonance in Medicine 44, 301–308.

Langkammer C, Bredies K, Poser BA, Barth M, Reishofer G, Fan AP, Bilgic B, Fazekas F, Mainero C, Ropele S, 2015. Fast quantitative susceptibility mapping using 3D EPI and total generalized variation. NeuroImage 111, 622–630.

Larkman DJ, Hajnal JV, Herlihy AH, Coutts GA, Young IR, Ehnholm G, 2001. Use of multicoil arrays for separation of signal from multiple slices simultaneously excited. Journal of Magnetic Resonance Imaging 13, 313–317.

Lauterbur P, 1973. Image formation by induced local interactions: examples employing nuclear magnetic resonance. Nature 242, 190–191.

Liu Q, Hughes DG, Allen PS, 1994. Quantitative Characterization of the Eddy Current Fields in a 40-cm Bore Superconducting Magnet. Magnetic Resonance Imaging 31, 73–76.

Lustig M, Pauly JM, 2010. SPIRiT: Iterative self-consistent parallel imaging reconstruction from arbitrary k-space. Magnetic Resonance in Medicine 64, 457–71.

Ma RE, Akçakaya M, Moeller S, Auerbach EJ, Ugurbil K, Van de Moortele PF, 2019. Correcting Eddy Current Induced Geometric Distortion for High Resolution Multi-Band Diffusion Weighted SE-EPI with Magnetic Field Monitoring at 7T, in: Proceedings of the 27th Scientific Meeting of the International Society for Magnetic Resonance in Medicine. p. 0922.

Mansfield P, 1977. Multi-planar image formation using. Journal of Physics C: Solid State Physics 10, 55–58.

Mansfield P, Maudsley AA, 1976. Line scan proton spin imaging in biological structures by NMR. Physics in Medicine and Biology 21, 847–852.

Mason GF, Harshbarger T, Hetherington HP, Zhang Y, Pohost GM, Twieg DB, 1997. A method to measure arbitrary k-space trajectories for rapid MR imaging. Magnetic Resonance in Medicine 38, 492–496.

McGee KP, Manduca A, Felmlee JP, Riederer SJ, Ehman RL, 2000. Image metric□based correction (Autocorrection) of motion effects: Analysis of image metrics. Journal of Magnetic Resonance Imaging 11, 174–181.

McKenzie CA, Yeh EN, Ohliger MA, Price MD, Sodickson DK, 2002. Self-calibrating parallel imaging with automatic coil sensitivity extraction. Magnetic Resonance in Medicine 47, 529–538.

McKinnon GC, 1993. Ultrafast interleaved gradient-echo-planar imaging on a standard scanner. Magnetic Resonance in Medicine 30, 609–616.

Meiboom S, Gill D, 1958. Modified spin-echo method for measuring nuclear relaxation times. Review of Scientific Instruments 29, 688–691.

Moriguchi H, Duerk JL, 2006. Bunched phase encoding (BPE): a new fast data acquisition method in MRI. Magnetic Resonance in Medicine 55, 633–48.

Mugler JP, 2014. Optimized three-dimensional fast-spin-echo MRI. Journal of Magnetic Resonance Imaging 39, 745–767.

Mugler JP, Brookeman JR, 1990. Three-dimensional magnetization-prepared rapid gradient-echo imaging (3D MP RAGE). Magnetic Resonance in Medicine 15, 152–157.

Noll DC, Nishimura DG, Macovski A, 1991. Homodyne Detection in Magnetic Resonance Imaging. IEEE Transactions on Medical Imaging 10, 154–163.

Ordidge RJ, Cresshull ID, 1986. The correction of transient B0 field shifts following the application of pulsed gradients by phase correction in the time domain. Journal of Magnetic Resonance 69, 151–155.

Peters AM, Brookers MJ, Hoogenraad FG, Gowland PA, Francis ST, Morris PG, Richard B, 2007. T2* measurements in human brain at 1.5, 3 and 7 T. Magnetic Resonance Imaging 25, 748–753.

Peters DC, Derbyshire JA, McVeigh ER, 2003. Centering the projection reconstruction trajectory: reducing gradient delay errors. Magnetic Resonance in Medicine 50, 1–6.

Pfeuffer J, Van Moortele PFD, Ugurbil K, Hu X, Glover GH, 2002. Correction of physiologically induced global off-resonance effects in dynamic echo-planar and spiral functional imaging. Magnetic Resonance in Medicine 47, 344–353.

Polak D, Cauley S, Huang SY, Longo MG, Conklin J, Bilgic B, Ohringer N, Raithel E, Bachert P, Wald LL, Setsompop K, 2019. Highly-accelerated volumetric brain examination using optimized wave-CAIPI encoding. Journal of Magnetic Resonance Imaging 50, 961–974.

Polak D, Setsompop K, Cauley SF, Gagoski BA, Bhat H, Maier F, Bachert P, Wald LL, Bilgic B, 2018. Wave-CAIPI for highly accelerated MP-RAGE imaging. Magnetic Resonance in Medicine 79, 401–406.

Poser BA, Bilgic B, Gagoski BA, Uludağ K, Stenger VA, Wald LL, Setsompop K, 2017. Echo-planar imaging with wave-CAIPI acquisition and reconstruction, in: Proceedings of the 25th Scientific Meeting of the International Society for Magnetic Resonance in Medicine. p. 1198.

Poser BA, Koopmans PJ, Witzel T, Wald LL, Barth M, 2010. Three dimensional echo-planar imaging at 7 Tesla. NeuroImage 51, 261–266.

Power JD, Barnes KA, Snyder AZ, Schlaggar BL, Petersen SE, 2012. Spurious but systematic correlations in functional connectivity MRI networks arise from subject motion. NeuroImage 59, 2142–2154.

Pracht ED, Feiweier T, Ehses P, Brenner D, Roebroeck A, Weber B, Stöcker T, 2018. SAR and scan-time optimized 3D whole-brain double inversion recovery imaging at 7T. Magnetic Resonance in Medicine 79, 2620–2628.

Preibisch C, Wallenhorst T, Heidemann R, Zanella FE, Lanfermann H, 2008. Comparison of parallel acquisition techniques generalized autocalibrating partially parallel acquisitions (GRAPPA) and modified sensitivity encoding (mSENSE) in functional MRI (fMRI) at 3T. Journal of Magnetic Resonance Imaging 27, 590–598.

Pruessmann KP, 2001. Advances in Sensitivity Encoding With Arbitrary k-Space Trajectories. Magnetic Resonance in Medicine 651, 638–651.

Pruessmann KP, Weiger M, Scheidegger MB, Boesiger P, 1999. SENSE: sensitivity encoding for fast MRI. Magnetic Resonance in Medicine 42, 952–962.

Purcell E, Torrey H, 1946. Resonance absorption by nuclear magnetic moments in a solid. Physical Review 69, 37–38.

Raj D, Paley D, Anderson AW, Kennan RP, Gore JC, 2000. A model for susceptibility artefacts from respiration infunctional echo-planar magnetic resonance imaging. Physics in medicine and biology 45, 3809–3820.

Reuter M, Schmansky NJ, Rosas HD, Fischl B, 2012. Within-subject template estimation for unbiased longitudinal image analysis. NeuroImage 61, 1402–1418.

Robison RK, Devaraj A, Pipe JG, 2010. Fast, simple gradient delay estimation for spiral MRI. Magnetic Resonance in Medicine 63, 1683–1690.

Robson PM, Grant AK, Madhuranthakam AJ, Lattanzi R, Sodickson DK, Mckenzie C a, 2010. Comprehensive Quantification of SNR Ratio and g-Factor for Image-Based and k-space Based Parallel Imaging Reconstructions. Magnetic Resonance in Medicine 60, 895–907.

Roemer PB, Edelstein WA, Hayes CE, 1990. The NMR Phased Array. Magn Res Med 225, 192–225.

Schenck JF, 1996. The role of magnetic susceptibility in magnetic resonance imaging: MRI magnetic compatibility of the first and second kinds. Medical Physics 23, 815–850.

Schwarz JM, Pracht ED, Brenner D, Reuter M, Stöcker T, 2018. GRAPPA reconstructed wave-

CAIPI MP-RAGE at 7 Tesla. Magnetic Resonance in Medicine 80, 2427–2438.

Schwarz JM, Pracht ED, Stöcker T, 2018. GRAPPA reconstructed 3D wave-CAIPI TSE at 7 Tesla, in: Proceedings of the 26th Scientific Meeting of the International Society for Magnetic Resonance in Medicine. p. 0938.

Schwarz JM, Stirnberg R, Ehses P, Stöcker T, 2019. Correction of physiological field fluctuations in high- and low-resolution 3D-EPI acquisitions at 7 Tesla, in: Proceedings of the 27th Scientific Meeting of the International Society for Magnetic Resonance in Medicine. p. 0446.

Seiberlich N, Breuer FA, Blaimer M, Barkauskas K, Jakob PM, Griswold MA, 2007. Non-Cartesian data reconstruction using GRAPPA operator gridding (GROG). Magnetic Resonance in Medicine 58, 1257–1265.

Setsompop K, Gagoski BA, Polimeni JR, Witzel T, Wedeen VJ, Wald LL, 2012. Blipped-controlled aliasing in parallel imaging for simultaneous multislice echo planar imaging with reduced g-factor penalty. Magnetic Resonance in Medicine 67, 1210–1224.

Smith SM, 2002. Fast robust automated brain extraction. Human Brain Mapping 17, 143–155.

Sodickson DK, Manning WJ, 1997. Simultaneous acquisition of spatial harmonics (SMASH): Fast imaging with radiofrequency coil arrays. Magnetic Resonance in Medicine 38, 591–603.

Spees WM, Buhl N, Sun P, Ackerman JJH, Neil JJ, Garbow JR, 2011. Quantification and Compensation of Eddy-Current-Induced Magnetic Field Gradients. Journal of Magnetic Resonance 212, 116–123.

Stirnberg R, Deistung A, Reichenbach J, Stöcker T, 2018. Accelerated quantitative susceptibility and R2* mapping with flexible k-t-segmented 3D-EPI, in: Proceedings of the 26th Scientific Meeting of the International Society for Magnetic Resonance in Medicine. p. 0320.

Stirnberg R, Huijbers W, Brenner D, Poser BA, Breteler M, Stöcker T, 2017. Rapid whole-brain resting-state fMRI at 3 Tesla: Efficiency-optimized three-dimensional EPI versus repetition time-matched simultaneous-multi-slice EPI. NeuroImage 163, 81–92.

Stirnberg R, Pflugfelder D, 2013. High-Resolution 3D-fMRI at 9.4 Tesla with Intrinsically Minimised Geometric Distortions, in: Proceedings of the 21th Scientific Meeting of the International Society for Magnetic Resonance in Medicine. p. 2372.

Stirnberg R, Stöcker T, 2014. Conventional 2D-EPI or Segmented 3D-EPI? A Temporal SNR Study at 3 and 7 Tesla, in: Proceedings of the 22th Scientific Meeting of the International Society for Magnetic Resonance in Medicine. p. 0868.

Tan H, Meyer CH, 2009. Estimation of k-space trajectories in spiral MRI. Magnetic Resonance in Medicine 61, 1396–1404.

Thunberg P, Zetterberg P, 2007. Noise distribution in SENSE- and GRAPPA-reconstructed images: a computer simulation study. Magnetic Resonance Imaging 25, 1089–1094.

Triantafyllou C, Hoge RD, Krueger G, Wiggins CJ, Potthast A, Wiggins GC, Wald LL, 2005. Comparison of physiological noise at 1.5 T, 3 T and 7 T and optimization of fMRI acquisition parameters. NeuroImage 26, 243–250.

Tustison NJ, Avants BB, Cook PA, Zheng Y, Egan A, Yushkevich PA, Gee JC, 2010. N4ITK: Improved N3 bias correction. IEEE Transactions on Medical Imaging 29, 1310–1320.

Uecker M, Lai P, Murphy MJ, Virtue P, Elad M, Pauly JM, Vasanawala SS, Lustig M, 2014. ESPIRiT - An eigenvalue approach to autocalibrating parallel MRI: Where SENSE meets GRAPPA. Magnetic Resonance in Medicine 71, 990–1001.

Van de Moortele PF, Pfeuffer J, Glover GH, Ugurbil K, Hu X, 2002. Respiration-induced Bo fluctuations and their spatial distribution in the human brain at 7 Tesla. Magnetic Resonance in Medicine 47, 888–895.

Van Der Zwaag W, Marques JP, Kober T, Glover G, Gruetter R, Krueger G, 2012. Temporal SNR characteristics in segmented 3D-EPI at 7T. Magnetic Resonance in Medicine 67, 344–352.

Van Gelderen P, De Zwart JA, Starewicz P, Hinks RS, Duyn JH, 2007. Real-time shimming to compensate for respiration-induced B0 fluctuations. Magnetic Resonance in Medicine 57, 362–368.

Vannesjo SJ, Barmet C, Duerst Y, Gross S, Brunner DO, Pruessmann KP, 2012. Higher-order monitoring of physiological field fluctuations in brain MRI at 7T, in: Proceedings of the 20th Scientific Meeting of the International Society for Magnetic Resonance in Medicine. p. 216.

Vannesjo SJ, Haeberlin M, Kasper L, Pavan M, Wilm BJ, Barmet C, Pruessmann KP, 2013. Gradient system characterization by impulse response measurements with a dynamic field camera. Magnetic Resonance in Medicine 69, 583–593.

Vannesjo SJ, Wilm BJ, Duerst Y, Dietrich BE, Brunner DO, Barmet C, Schmid T, Pruessmann KP, 2013. Snapshot field monitoring enables correction of slow field perturbations in high-resolution brain MRI, in: Proceedings of the 21th Scientific Meeting of the International Society for Magnetic Resonance in Medicine. p. 2569.

Vannesjo SJ, Wilm BJ, Duerst Y, Gross S, Brunner DO, Dietrich BE, Schmid T, Barmet C, Pruessmann KP, 2015. Retrospective correction of physiological field fluctuations in high-field brain MRI using concurrent field monitoring. Magnetic Resonance in Medicine 73, 1833–1843.

Versluis MJ, Peeters JM, Rooden S van, Grond J van der, Buchem MA van, Webb AG, Osch MJ van, 2010. Origin and reduction of motion and f0 artifacts in high resolution T2*-weighted magnetic resonance imaging: Application in Alzheimer's disease patients. NeuroImage 51, 1082–1088.

Wang H, Qiu Z, Su S, Jia S, Li Y, Liu X, Zheng H, Liang D, 2020. Parameter optimization framework on wave gradients of Wave-CAIPI imaging. Magnetic Resonance in Medicine 83, 1659–1672.

Wang Z, Wang J, Detre Ja, 2005. Improved data reconstruction method for GRAPPA. Magnetic Resonance in Medicine 54, 738–742.

Weigel M, 2015. Extended phase graphs: Dephasing, RF pulses, and echoes - Pure and simple. Journal of Magnetic Resonance Imaging 41, 266–295.

Wezel J, Boer VO, Velden TA van der, Webb AG, Klomp DW, Versluis MJ, Osch MJ van, Garpebring A, 2017. A comparison of navigators, snap-shot field monitoring, and probe-based field model training for correcting B0-induced artifacts in T2*-weighted images at 7 T. Magnetic Resonance in Medicine 78, 1373–1382.

Wilm BJ, Barmet C, Pavan M, Pruessmann KP, 2011. Higher order reconstruction for MRI in the presence of spatiotemporal field perturbations. Magnetic Resonance in Medicine 65, 1690–1701.

Wilm BJ, Nagy Z, Barmet C, Vannesjo SJ, Kasper L, Haeberlin M, Gross S, Dietrich BE, Brunner DO, Schmid T, Pruessmann KP, 2015. Diffusion MRI with concurrent magnetic field monitoring. Magnetic Resonance in Medicine 74, 925–933.

Yuhua W, Chronik BA, Bowe C, Mechefske CK, Rutt BK, 2000. Gradient-induced acoustic and magnetic field fluctuations in a 4T whole-body MR imager. Magnetic Resonance in Medicine 44, 532–536.

Zhang T, Pauly JM, Vasanawala SS, Lustig M, 2013. Coil compression for accelerated imaging with Cartesian sampling. Magnetic Resonance in Medicine 69, 571–582.

Zhang Y, Hoby P, Stokely EM, Mason GF, Twieg DB, 1998. Novel k-Space Trajectory Measurement Technique. Magnetic Resonance in Medicine 39, 999–1004.

Zhou Z, Yuan C, Börnert P, 2020. Self-calibrating wave-encoded 3D turbo spin echo imaging using subspace model based autofocusing. Magnetic Resonance in Medicine 83, 1250–1262.

Zwanenburg JJ, Versluis MJ, Luijten PR, Petridou N, 2011. Fast high resolution whole brain T2* weighted imaging using echo planar imaging at 7T. NeuroImage 56, 1902–1907.

List of Figures

List of Tables

Acknowledgements

This work would not have been possible without the support, encouragement and expertise of many people. I would like take the opportunity to express my sincere gratitude to

- my supervisor Tony Stöcker for giving me the chance to join his group. For your continuous guidance and advice throughout my thesis and for always having an open ear (or rather an open office door). And thank you for your support in making it possible to combine research and family.
- Daniel Brenner, Eberhard Pracht and Rüdiger Stirnberg for pushing my research in the right direction. Thanks for providing the MR sequences and a lot of expertise, for your patience and for the many fruitful discussions.
- my fellow doctoral student and office mates Suzan Akbey, Yannik Völzke, Alexandra Koch, Markus Boland and Martin Schidlowski. Thank you for the great working atmosphere, the many interesting (scientific) conversations, your continuous support and motivation and for your help with computer, programing, scientific, ‘googling’ and all other kinds of questions.
- Sascha Brunheim, Philipp Ehses, Daniel Brenner and Marten Veldmann for your support with the field probes system.
- Christian Mirkes, Benjamin Dietrich and the rest of the Skope team for the great collaboration and continuous support with the field probes system.
- Suzan Akbey, Rüdiger Stirnberg, Eberhard Pracht, Philipp Ehses and Yannik Völzke for spending your valuable time on proof-reading parts of this thesis. Your constructive criticism and helpful suggestions contributed a lot to the success of this work.

- Anke Rühling for introducing me to the operation of the scanner and for your support and open ear.
- the whole MR physics group for the great time in a pleasant and friendly (working) atmosphere, for entertaining lunch and coffee breaks, conferences and retreats. Many thanks for any kind of help during the last years. Furthermore, I would like to thank all of you who volunteered for the MRI measurements required for the preparation and completion of this thesis.
- my parents Agnes and Otto Schwarz and my sisters Jenny, Leila and Samira for your love and continuous support throughout my life and especially during the last weeks of writing this thesis. Without your help, it would never have been possible to keep my personal deadline for the completion of this thesis.
- my friends for your support, motivation and joyful distractions from work.
- and last but not least to my husband Pascal Huber for his continuous support, encouragement and patience, especially during busy times. Thanks to my son Linus and also the baby-in-belly for giving me the motivation to finish my thesis in time and for giving me a wonderful balance to work.